Aston University

Some parts of this thesis may have been removed for copyright restrictions.

If you have discovered material in AURA which is unlawful e.g. breaches copyright, (either yours or that of a third party) or any other law, including but not limited to those relating to patent, trademark, confidentiality, data protection, obscenity, defamation, libel, then please read our Takedown Policy and contact the service immediately

Application of SOA-NOLM in All-Optical Processing

Mohamad Halim Bin Abd Wahid

Doctor of Philosophy

Aston University

February 2009

This copy of the thesis has been supplied on condition that anyone who consults it is understood to recognise that its copyright rests with its author and that no quotation from the thesis and no information derived from it may be published without proper acknowledgement.

Aston University

Application of SOA-NOLM in All-Optical Processing

Mohamad Halim Bin Abd. Wahid

Doctor of Philosophy

February 2009

Summary

This thesis presents experimental investigations of the use of semiconductor optical amplifiers in a nonlinear loop mirror (SOA-NOLM) and its application in all-optical processing. The techniques used are mainly experimental and are divided into three major applications.

Initially the semiconductor optical amplifier, SOA, is experimentally characterised and the optimum operating condition is identified. An interferometric switch based on a Sagnac loop with the SOA as the nonlinear element is employed to realise all-optical switching. All-optical switching is a very attractive alternative to optoelectronic conversion because it avoids the conversion from the optical to the electronic domain and back again.

The first major investigation involves a carrier suppressed return to zero, CSRZ, format conversion and transmission. This study is divided into single channel and four channel WDM respectively. The optical bandwidth which limits the conversion is investigated. The improvement of the nonlinear tolerance in the CSRZ transmission is shown which shows the suitability of this format for enhancing system performance.

Second, a symmetrical switching window is studied in the SOA-NOLM where two similar control pulses are injected into the SOA from opposite directions. The switching window is symmetric when these two control pulses have the same power and arrive at the same time in the SOA.

Finally, I study an all-optical circulating shift register with an inverter. The detailed behaviour of the blocks of zeros and ones has been analysed in terms of their transient measurement. Good agreement with a simple model of the shift register is obtained. The transient can be reduced but it will affect the extinction ratio of the pulses.

Keywords and phrases

SOA-NOLM, CSRZ, symmetrical switching window, all-optical circulating shift register.

Acknowledgements

I would like to express my gratitude to my supervisor, Professor K.J.Blow for giving me the opportunity to be a member of his research group. I would like to thank him for the knowledge and support that he has given me in completing this doctoral thesis.

I am grateful to the members of the Photonics Research Group especially M.M.Nahas, W.M.Wong, R.Ibbotson, S.A.Feiven, H.Lu, J.Harrison, P.Harper, T.Ellingham and N.Johnson who have contributed to a conducive research environment and with technical and administrative supports.

I am indebted to my wife Alroyanti M Ali, for her patience and support especially in the last phase of writing this thesis. This acknowledgement also goes to my family members for their encouragement in completing this PhD work.

Finally, special thanks to Majlis Amanah Rakyat (MARA) Malaysia for their financial support through a scheme named 'Skim Pelajar Cemerlang, SPC'.

To my lovely wife Alroyanti, mum Aishah, bro Salim and sis Halina.

Thanks for all the support and patience in this work.

Contents

Abbreviations

ASE	amplified spontaneous emission
BER	bit error rate
BPF	band pass filter
CH	carrier heating
CW	continuous wave
cw	clockwise
ccw	counter-clockwise
DFB	distributed feedback laser
DFF	dispersion-flattened fibre
DH	double heterostructure
DL	optical delay line
DSF	dispersion-shifted fibre
EDFA	Erbium-doped fibre amplifier
FBG	fibre Bragg grating
FPSOA	Fabry-Perot semiconductor optical amplifier
FWHM	full wave half maximum
FWM	four wave mixing
GVD	group velocity dispersion
MMF	multimode fibre
NA	numerical aperture
NOLM	nonlinear loop mirror
OSA	optical spectrum analyser
OSNR	optical to signal noise ratio
OTDM	optical time-division multiplexing
PBC	polarisation beam combiner
PMD	polarisation mode dispersion
PPG	pulse pattern generator
PRBS	pseudorandom bit sequence
SBS	stimulated Brillouin scattering
SHB	spectral hole burning
SLA	semiconductor laser amplifier
SLALOM	semiconductor laser amplifier nonlinear loop mirror
SMF	single mode fibre
SOA	semiconductor optical amplifier
SOA-NOLM	semiconductor optical amplifier nonlinear loop mirror
SPM	self-phase modulation
SRS	stimulated Raman scattering
SSMF	standard single-mode fibre
TE	transverse electric
THG	third harmonic generation
TIR	total internal reflection
TM	transverse magnetic
TOAD	terahertz optical asymmetric demultiplexer
TWSOA	traveling-wave semiconductor optical amplifier
UNI	ultrafast nonlinear interferometer
WDM	wavelength-division multiplexing
XGM	cross-gain modulation
XPM	cross-phase modulation

List of Figures

List of Tables

Chapter 1

Introduction and Overview

1.1 Historical overview in communication technology

Since the 19th century, the need to communicate has created interest in devising communication systems for conveying information from one location to another. In 1838, the invention of the telegraph by Samuel F.B. Morse opened the era of electrical communication. The telegraph passed information at a data rate of a few bits per second through a wire cable. The telegraph was followed by the advent of the electromagnetic telephone by A.G. Bell in 1876 where electric signals were transmitted in analogue form through a continuously varying electric current [1]. This event drastically transformed the development of communication technology. One of the greatest 19th century scientists, James C. Maxwell described the propagation of the electromagnetic waves mathematically in his famous Maxwell's equations. These equations are the foundation of the modern communication which form what we now characterise as advanced or high technology. Maxwell's equations described exactly the behaviour and interaction of electric and magnetic fields. From his work, he has proved that all electromagnetic waves, in a vacuum, travel at 300000 km per second which is equal to the speed of light. He then deduced that light is an electromagnetic wave, therefore the wave spectrum must contain many invisible waves, each with its own wavelength and characteristic [2]. Based on the predictions of Maxwell, Heinrich Hertz and Gugliemo Marconi discovered these unseen waves and demonstrated what is now called wireless communication. With the invention of electronic devices such as triodes and transistors in the early to mid 20^{th} century, radio communication and later transatlantic connections become possible. The trend in electrical communication systems is to employ progressively shorter wavelengths (higher

frequencies), which offer corresponding increases in bandwidth or information capacity. The bandwidth required is determined by the ever growing desire to transmit information, this led to the birth of optical fibre communications where signals in an optical format are now carried not by frequency modulation of the carrier (although this is still possible), but by varying the intensity of the optical power [3]. Therefore, the modern era of communication could be said to have originated with the invention of the laser in 1960.

1.2 Evolution of fibre optic communications

Fibre optic communication systems use optical fibres as the transmission medium; hence, the bit rate-distance product can be improved by several orders of magnitude due to the large available bandwidth and the very low-loss of the medium. When optical fibers were first introduced in the 1960s, they had extremely high loss, exceeding 1000 dB/km [4]. The combination of low-loss optical fibres and the advance in semiconductor technology made optical fibre communication systems practically possible. The development of fibre optic communication systems can be classified into four generations. The first generation of optical fibre communication systems utilised multimode optical fibres and operated in the 0.8 μm wavelength region. The advantage of the multimode fibres is that their core is large; therefore, coupling of the light from the source into the fibre is not difficult. However, the large core diameter also leads to an unavoidable drawback. The optical waves travel in a multimode fibre with different paths; thus, they arrive at the receiver with different time delays, which causes pulse spreading. This phenomenon is known as inter-modal dispersion. The system in the first generation is therefore limited by this dispersion and fibre loss. In the second generation these two problems were eliminated by using a single-mode fibre instead of a multimode fibre in the 1.3 μm region. For this type of fibre, there is only one path (mode), in which the optical wave is allowed to travel.

When the attenuation of single-mode and multimode optical fibres is considered, the attenuation in the 1.3 μm wavelength region is less than that in 0.8 μm. In addition, another advantage of using the single-mode optical fibre is that this type of fibre has less internal (Rayleigh) scattering [5]; thus, contributing to the lower attenuation of the single-mode optical fibre. Both advantages led to the move of the operating wavelength from 0.8 to 1.3 μm resulting in both higher bit-rates and longer transmission distances.

The third generation had seen that the attenuation of a single-mode optical fibre is lowest in the 1.55 μm wavelength window (0.2 dB/km). However, the dispersion of a standard single-mode fibre in this wavelength window is very large [+17 ps/(km·nm)], which is intolerable for very high bit-rate and long distance systems. Note that the units of dispersion constant are ps of delay spread per km of transmission length, per nm of wavelength spread. In order to take the advantage of lowest attenuation at this wavelength window, narrow-linewidth lasers are required to minimize the effect of dispersion. Another approach is to employ a new type of fibre, known as dispersion shifted optical fibre (DSF) whose core-and-cladding profile is tailored so that the dispersion is minimum at the 1.55 μm wavelength region. With the development of optical amplifiers in the fourth generation, the huge amount of bandwidth offered by the optical fibre could be fully utilised by using the wavelength division multiplexing (WDM) technique. All channels could be simultaneously amplified without optical-electrical-optical conversion with the help of optical amplifiers, thus, the spacing between electrical regenerative repeaters could be extended considerably. As a result, the bit-rate distance product was significantly increased, and can be larger than 100,000 Gb/s-km. There is another approach that can combat the dispersion effect which is to make use of fibre nonlinearity to balance the effect of dispersion, which results in the shape of optical pulses being preserved while

travelling along the transmission link. The systems that utilise this technique are called soliton-based systems [4].

In many applications the signal in the transmission link has to be converted to electronic form before arriving at the receiver. Electro-optical conversion delays the signal propagating in an optical fibre. In such a network, all communication is limited by the capabilities of the electronics in the system. Once the optical signal is converted into an electronic signal, some form of processing unit must examine the data and decide to which output fibre and wavelength the data must be forwarded. The data must then be modulated onto the optical carrier. All of these steps involve significant delays enforced by the limitations of electronic processing speed. However, the conversion is unnecessary with the advancement of all-optical communication systems. The all-optical systems in which the light propagates without ever being converted to electrical signals, have been in existence since the advent of low-loss fibres and EDFAs in the mid-1990s.

1.3 All-optical processing

Generally, all-optical refers to the use of optical devices that do not require switching back into the electrical domain. Using all-optical processing makes opto-electrical or electro-optical conversion in the system unnecessary, which can potentially be more cost-effective. Moreover, the bandwidth of the signal can be significantly larger, compared to electrical processing, because the optical signal processor can work at higher bit rates. This enables optical transmission systems where the bit rates in a single wavelength channel can exceed the bandwidth of electronics. Therefore, future optical signal processing can achieve higher operating speed compared to electronics. In order to

achieve high operating speeds and stable operation, the optical signal processing should be carried out in integrated devices [5].

1.4 Objectives and thesis outline

The objective of this work is to utilise the nonlinear behaviour associated with an SOA-NOLM for application in all-optical signal processing. Three experiments have been done with different control pulses applied into the SOA-NOLM. In detail, the investigations include:

a) *Generation and transmission of carrier suppressed return to zero, CSRZ, modulated data.*

   This is accomplished by converting return to zero, RZ, format to CSRZ using sinusoidal control pulses. Then, the CSRZ is put into the transmission loop for performance measurement in comparison with the RZ.

b) *Observation and measurement of a symmetrical switching window.*

   The switching window that is observed in a typical SOA-NOLM is basically asymmetrical when only a single control pulse is used. However, a symmetrical switching window is achieved if two identical control pulses are employed in opposite directions through the SOA.

c) *Characterisations of the transient behaviour in all-optical shift register.*

   An all-optical shift register is obtained if the output of an SOA-NOLM optical switch is fed back as the control pulse. A real time oscilloscope has been used to observe the transient behaviour of the stored pulses.

The above aims have been performed with the optimum operation parameters for the SOA-NOLM in different configurations as determined by characterising the device.

This thesis is written in seven chapters. Chapter one gives a brief historical perspective about the telecommunications, the principle reasons for optical fibre communication and the goals of this work. The theoretical background on communicating in fibres is presented in chapter two. The optical nonlinearities are also stated in this chapter. In chapter three, the basic nonlinear properties of the SOA and the operation of the SOA-NOLM are described. This includes the details of the experimental procedures used. Chapter four is dedicated to the CSRZ conversion and transmission. The CSRZ conversion is discussed for a single channel and WDM channels. The results and discussion from the symmetrical switching window experiment is provided in chapter five. The transient in the all-optical circulating shift register is presented in chapter six. Finally, the results obtained are concluded in chapter seven and a brief outline of future work is provided.

Chapter 2

Theory of Optical Fibre Communications

2.1 Introduction

The explosive growth of the internet has put a new demand on the provision of bandwidth for the transmission of information. The transmission medium that offers the widest bandwidth of any electromagnetic waveguide is the optical fibre. There are many advantages of using optical fibres for instance: large bandwidth and low loss; immunity to electromagnetic interference; comparatively lighter and cheaper than copper cables of equivalent bandwidth. Their bandwidth-distance product, *BL,* significantly exceeds that obtained in systems based on radio, microwave, satellite, and free–space optical transmission in the distance range of a few tens to thousands of kilometres. Modern optical transmission systems contain a large number of individual optical components such as lasers, modulators, multiplexers, filters, optical fibres, and amplifiers. Fig. 2.1 shows the schematics of a basic optical transmission system.

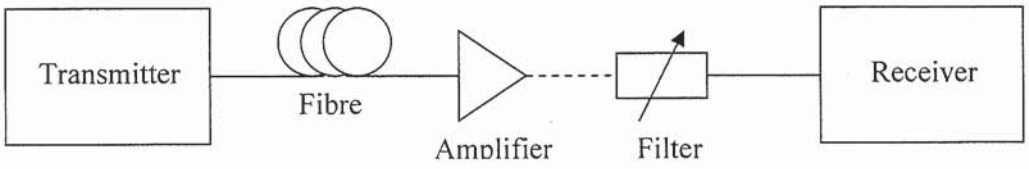

Fig. 2.1. Optical transmission system.

The optical signal is generated by a transmitter and inserted into the fibre. It then passes through a transmission line that primarily consists of fibre spans and optical amplifiers. At the end of the transmission line, the signal is filtered and converted to electrical current by a receiver.

2.2 Characteristics of optical fibres

An optical fibre is a dielectric waveguide that operates at optical frequencies. The optical fibres are generally made from silica (SiO_2) which has a stable, well-controlled refractive index and is highly transparent. The fibre as shown in Fig. 2.2 is composed of the core and cladding regions with refractive indices n1 and n2 (n1 > n2) respectively and an elastic buffer encapsulation for strength and mechanical isolation. Fibres are characterised into single mode and multimode, principally determined by the core diameter. Single-mode fibres (also called monomode fibres) are optical fibres which are designed so that they support only a single propagation mode for a given wavelength. They usually have a relatively small core and a small refractive index difference between core and cladding. Typically, a fibre has single-mode characteristics only over a limited wavelength range with a width of a few hundred nanometres. The limit towards smaller wavelengths is given by the single-mode cut-off wavelength, beyond which the fibre supports multiple modes. For step-index fibres, the condition for single-mode guidance can be calculated using the V number (normalized frequency), which must be below $\approx$2.405. In optical fibre communications systems, single-mode guidance avoids the problem of modal dispersion, which (in multimode fibre) would lead to the occurrence of multiple copies of the input signals at the receiver. Multimode fibres (MMF), with a larger core diameter, are advantageous from the point of view of coupling light and the ease of launching optical power.

In a fibre, attenuation and dispersion are two of the main important design issues. Attenuation in fibres determines the amplifier spacing while dispersion leads to broadening of individual optical pulses with propagation causing the transmitted signal to be severely degraded. This problem is most severe in multimode fibres since pulses spread

rapidly (typically at a rate of 10ns/km) because of different speeds associated with different fibre modes [3].

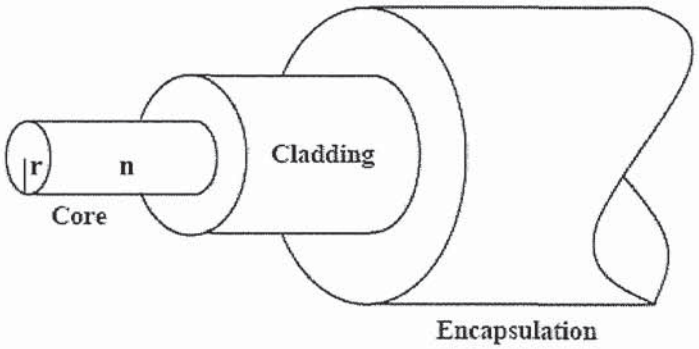

Fig. 2.2. Schematic of a single optical fibre.

Besides dispersion, nonlinearity is another major limiting factor that causes degradation in optical communication. In some circumstances, the nonlinearity could counteract the dispersion. In addition, when multiple channels are considered, the fibre nonlinearity results in interactions among channels.

2.2.1 Geometrical configuration

A fibre waveguide is normally cylindrical in form. The most widely accepted structure is the single solid dielectric cylinder of radius, r and index of refraction, n shown in Fig. 2.2. Variations in the material composition of the core define two fibre types known as a step-index fibre and a graded-index fibre. In step-index fibres, the refractive index changes abruptly at the core-cladding interface, whereas the refractive index decreases gradually in the graded-index fibre. Both fibres can be further divided into single-mode and multimode classes.

Consider the geometry of Fig. 2.3, where a cylindrical glass fibre consisting of an inner core of refractive index, n, an outer cladding of refractive index, n_1, an air of refractive index, n_o and a ray making an incident angle, θ_i, at the core centre. The angles of incidence, θ_i and refraction, θ_r can be related to the refractive indices of the media by using Snell's law, which is [3]

$$n_o \sin\theta_i = n \sin\theta_r . \tag{2.1}$$

From Fig. 2.3, when $\phi' = \pi/2$, the incidence angle, ϕ is called the critical angle, ϕ_c, which is given by

$$\sin\phi_c = \frac{n_1}{n} . \tag{2.2}$$

There is a wave that propagates along the core-cladding surface called the evanescent wave. For incident angles larger than ϕ_c, the ray experiences total internal reflection (TIR) and guided in the fibre with no losses at the boundary. By applying Snell's law to the air-fibre interface and nothing that $\theta_r = \pi/2 - \phi_c$, Eq. (2.2) can be related to the maximum entrance angle, $\theta_{i,\max}$ through the relationship

$$n_o \sin\theta_{i,\max} = n\cos\phi_c = \sqrt{\left(n^2 - n_1^2\right)} . \tag{2.3}$$

This equation represents the light-gathering capacity of an optical fibre and also is defined as the numerical aperture (NA) of a step-index fibre. If the relative index difference $\Delta = (n - n_1)/n$ is small, the NA can be approximated by $NA \cong n(2\Delta)^{1/2}$ [6]. Typical values of the parameter Δ range from 1 to 3 percent for MMF and from 0.2 to 1.0 percent for SMF.

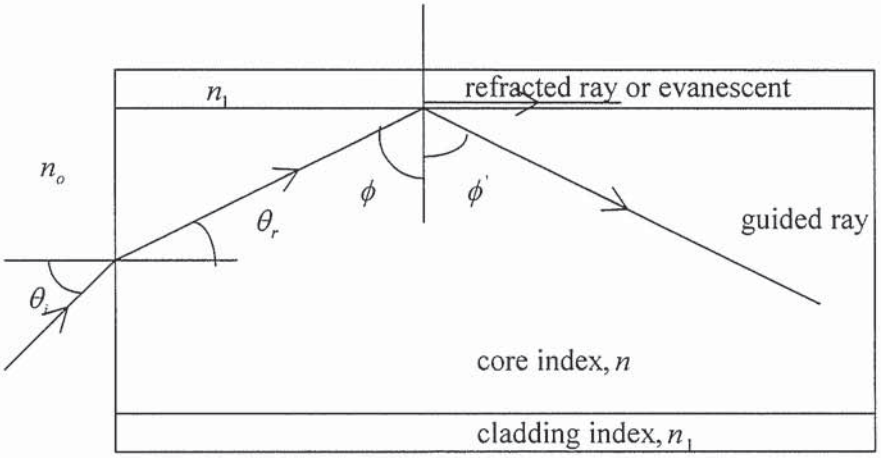

Fig. 2.3. Refraction and total internal reflection in step-index fibres.

2.2.2 Modes

The propagation of light along a fibre or waveguide can be described by a set of electromagnetic waves known as modes of the waveguide. If the electromagnetic wave of the frequency, f is to propagate in the fibre with refractive index, n in the direction, z in time, t as shown in Fig. 2.4, the electric field vector, $\bar{E}$ and the magnetic field vector, $\bar{H}$ can be written in a cylindrical coordinate system $\{r, \phi, z\}$ as [2]

$$\bar{E} = E_o(r, \phi) e^{j(\omega t - \beta z)} \tag{2.4}$$

$$\bar{H} = H_o(r, \phi) e^{j(\omega t - \beta z)} \tag{2.5}$$

where E_o and H_o are fields constant; $\omega = 2\pi f$ is the angular frequency of the wave; and $\beta = 2\pi \bar{n}/\lambda$ is the propagation constant of the wave with an effective refractive index, $\bar{n}$

and wavelength, λ. The modes refer to a specific solution of these wave equations that satisfy the appropriate boundary conditions. The boundary conditions follow from Maxwell's equations, and essentially may be stated as the tangential components of $\bar{E}$ and $\bar{H}$ are continuous across the boundary. From Fig. 2.4, mode solutions can be obtained by taking either $E_z = 0$ or $H_z = 0$. The modes are called transverse electric or TE modes when $E_z = 0$, and they are called transverse magnetic or TM modes when $H_z = 0$. However, in optical fibres the core-cladding boundary conditions lead to a coupling between the electric and magnetic fields components. Thus, fibres modes are denoted by HE_{mn} or EH_{mn}, depending on which component makes a larger contribution to the transverse field . The subscripts are referred to possible modes of propagation of the optical fields and can be obtained by solving the eigenvalue equation which is given in details in other references [1-3]. The number of modes is determined by the normalised frequency, V or the V-number which is given by [3]

$$V = \frac{2\pi r\sqrt{\left(n^2 - n_1^2\right)}}{\lambda} = \frac{2\pi r}{\lambda} NA \tag{2.6}$$

where r is the core radius of the step-index fibre and n_1 is the refractive index of the cladding. A fibre with a large value of V can support multimode, however a single-mode fibre (SMF) supports only the fundamental mode of the fibre i.e. HE_{11} or also known in the linearly polarised mode as LP_{01}. The LP_{01} mode is an approximation of weakly guided fibre with a small refractive index difference, Δ between the core and the cladding. For small Δ both electric and magnetic fields are plane polarised everywhere in the fibre cross section. The HE_{11} can be polarised in any arbitrary direction in the $x - y$ plane.

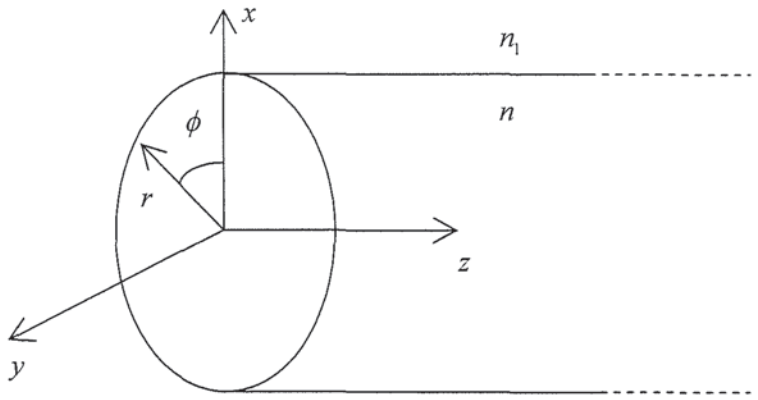

Fig. 2.4. Cylindrical coordinate system for a wave propagating in a fibre.

The wavelength at which the SMF suddenly becomes multimode is called the cut-off wavelength, λ_c and is given by Eq. (2.3) when $V = 2.405$. Each fibre mode propagates with an effective refractive index, $\bar{n} = \beta / 2\pi\lambda$ and remains guided as long as β satisfies the condition $n_1 k \langle \beta \langle nk$ where $k = 2\pi/\lambda$ is the wavenumber. For large values of V the total number of modes can be approximated by $V^2/2$.

2.2.3 Attenuation and losses

An optical signal will experience attenuation as it propagates along a fibre, this leads to a loss of signal. The mechanisms of attenuation can be classified into two major groups;

a) *Absorption* is basically related to the property of the fibre material. It is caused by atomic defects, impurity atoms and the constituent atoms in the glass material. As a result light is absorbed and converted into stored energy within the material.

b) *Scattering* is associated both with the fibre material and structural imperfections in the fibre geometry. Therefore, light is scattered away from its original direction.

Total optical attenuation can be expressed by Beer's Law [7]

$$P_{out} = P_{in} e^{-\alpha z} \tag{2.7}$$

where P_{out} and P_{in} are the output and the input powers of the optical waves, respectively, and α is the attenuation coefficient. When α is independent of z, the power decays exponentially with distance

$$P(z) = P(0) e^{-\alpha z} \tag{2.8}$$

where

$$\alpha = \frac{1}{z} \ln\left[\frac{P(0)}{P(z)}\right]. \tag{2.9}$$

Over the length of a fibre, L, a loss of $-10\log_{10}[\exp(-\alpha L)]$ dB/km is obtained. The typical unit of attenuation is in dB/km.

Scattering losses in fibre arise from microscopic variations around the average material density, and local microscopic variations in composition due to structural inhomogeneities or defects occurring in the fibre manufacture. These two effects give rise to fluctuations of refractive index on a scale that is small compared to wavelength. This causes the light to be scattered in the manner known as Rayleigh scattering. In general, a Rayleigh scattering loss coefficient may be defined such that $\alpha_R = A_R / \lambda^4$ where A_R is a constant for any material. Since Rayleigh scattering follows a characteristic λ^{-4} dependence, it decreases dramatically with increasing wavelength. When the attenuation of single-mode and multimode optical fibres is considered, the attenuation in the 1.3 μm wavelength region is less than that in 0.8 μm as shown in Fig. 2.5. The single-mode optical fibre has less

internal scattering [8]; thus, the attenuation is also less than that of the MMF. Note that the peak near 1.4 μm and a smaller peak near 1.23 μm seen in Fig. 2.5 are due to absorption caused by Hydroxyl (OH) impurities in the fibre [1]. In addition, a standard single-mode fibre (SSMF) exhibits lowest dispersion in this new region. These advantages lead to the higher *BL* product. It is clearly seen from Fig. 2.5 that the attenuation of a single-mode optical fibre is lowest in the 1.55 μm wavelength window (0.2 dB/km).

Fig. 2.5. Fibre attenuation as a function of wavelength for SSMF [3].

Besides absorption and scattering, the optical power can be lost due to bending, and from defects at connections between fibres. Principally the optical power scattered out of a fibre at a major bend depends exponentially on the radius of curvature, R. The bending loss is proportional to $\exp(R/R_c)$ where $R_c \cong r/(NA)^2$, r being the radius of the fibre core [2]. As the radius of curvature decreases, the loss increase exponentially until at a certain radius the curvature loss becomes observable. This type of bends is known as macrobending losses or simply bending losses. This causes some of the light not to be

internally reflected but to propagate into the cladding and be lost. Other type of bends is called microbending loss which refers to nonuniformities in the manufacturing or nonuniform lateral pressures created when a fibre is wound in tension on to a drum. Bending losses become significant when the bend is extended over a long distance.

2.2.4 Dispersion

One of the fundamental bandwidth limitations in optical fibre is dispersion. Dispersion describes the spreading of an optical signal in time as it travels along a fibre. This leads to broadening of optical pulses and may cause overlapping of adjacent pulses. The broadening can be explained by examining the behaviour of the group velocities of the guided modes. There are three causes of dispersion namely modal dispersion, material dispersion and waveguide dispersion. Modal dispersion arises in waveguides with more than one propagating mode. The modes arrive at the end of the waveguide slightly delayed relative to each other. The time delay, $\Delta\tau$ for a step-index fibre is given by [9]

$$\Delta\tau = \frac{1}{2cn}(NA)^2 . \tag{2.10}$$

One way to eliminate mode dispersion is to use a single-mode fibre.

In an ideal optical fibre, the fundamental mode has two orthogonal polarisations that travel at the same speed. The signal that is transmitted over the fibre is however randomly polarised, i.e. a random superposition of these two polarisations. The two polarisation components will slowly separate, e.g. causing pulses to spread and overlap. The time separation or delay between the two principal polarisation modes is called differential group delay (DGD) which is proportional to the square root of propagation distance L.

Polarisation Mode Dispersion (PMD) is the average differential group delay one expects to see when measuring an optical fibre. The PMD in fibres can be compensated by using polarisation controllers, and applying differential delay to bring them back into synchronous.

For a single-mode optical fibre, the only source of dispersion is due to group velocity dispersion (GVD), or intramodal dispersion which consists of material dispersion and waveguide dispersion. This causes different spectral components to propagate along an optical fibre with different group velocities. For an optical fibre of length, L, the spectral component at a frequency, ω would exit the fibre at a time delay of $T = L/v_g$ [1]. The group velocity, v_g can be related to the phase (propagation) constant, β by

$$v_g = \left(\frac{d\beta}{d\omega}\right)^{-1} . \tag{2.11}$$

Due to the frequency dependence of β, one can show that a pulse having the spectral width of $\Delta\omega$ is broadened by

$$\Delta T = \beta_2 L \Delta\omega \tag{2.12}$$

where $\beta_2 = d^2\beta / d\omega^2$, which is generally called the GVD parameter, with units of ps^2/km. The β_2 can be interpreted as the dispersion per unit transmission distance per unit frequency spread of the signal. The broadening of the pulses only applies to initially unchirped Gaussian pulses. In optical fibre communication systems, the wavelength unit is more commonly used than the frequency unit, and Eq. (2.12) can be rewritten as

$$\Delta T = DL\Delta\lambda \tag{2.13}$$

where $\Delta\lambda$ is the signal spectral width in wavelength units, and D is the dispersion parameter in the units of ps/(km·nm). The dispersion parameter, D can be related to β_2 by

$$D = \frac{d}{d\lambda}\left(\frac{1}{v_g}\right) = -\frac{2\pi c}{\lambda^2}\beta_2 \tag{2.14}$$

where c is the velocity of light in vacuum, and λ is the wavelength. Fig. 2.6 [1] shows the two main causes of intramodal dispersion. Material dispersion, D_M, is due to the spread of refractive index over the core as a function of wavelength. Dispersion caused by non-constant group velocity as a function of λ for a fixed mode is called waveguide dispersion, D_w and depends on the V parameter of the fibre. Generally, the dispersion parameter, D can be written as the sum of both dispersions ($D \approx D_m + D_w$). It is clearly seen from Fig. 2.6 that the material dispersion increases with wavelength. The wavelength, λ_{zD} at which the material dispersion becomes zero is in the range of 1.27-1.29 μm depending primarily on the materials used to control the index of refraction of the core of the fibre [1]. The material dispersion becomes positive for wavelengths above λ_{zD} and negative in the entire wavelength range 0-1.6 μm. For a SSMF the dispersion D is zero near 1.31 μm. The typical value of D for a SSMF is around 15 to 18 ps/(km·nm) in the 1.55 μm wavelength window where the fibre attenuation is the lowest. Such a high value of D poses the major limitation on 1.55 μm systems. Although the material dispersion can be altered, significant changes are difficult to achieve in practice. On the other hand, waveguide dispersion can be modified fairly easily by changing the refractive index profile of core and cladding. By changing the refractive index profile of an optical fibre the variation of waveguide dispersion as a function of wavelength can be tailored so that the total dispersion is zero at 1.55 μm. This type of optical fibre is generally called dispersion-shifted fibre (DSF). Its

minimum dispersion at 1.55 μm wavelength region allows the effective use of the wavelength region where the fibre loss is minimum. The distance between the transmitter and the receiver can be enhanced considerably by employing DSF due to the small effect of dispersion. The total dispersion also can be made relatively small over a wide range extending 1.3 μm to 1.6 μm. Such fibres are called dispersion-flattened fibres (DFF). The dispersive effects, however, do not disappear completely although dispersion-modified fibre is employed, and thus play a role in pulse broadening. The dispersion establishes the maximum data rate that can be attained for a communication link.

Fig. 2.6. Dispersion of a single mode fibre [1].

2.3 Nonlinear effects in optical fibres

Nonlinear optics is a material phenomenon in which intense light induces a nonlinear response in the medium, and in return the medium modifies the optical fields in a nonlinear way. In fact, all media are nonlinear to a certain degree. The nonlinear effects in optical fibres are generally not negligible, although silica glass has very small nonlinear coefficients. This is because the optical intensity of a propagating signal is high despite the fact that the signal power is rather low (several milliwatts to tens of milliwatts). The small cross section of an optical fibre causes the intensity to be very high, which in effect is sufficient to induce significant effects of nonlinearity. The optical nonlinearity in the fibre is basically governed by Maxwell's equations. Based on Maxwell's equations a wave equation for the optical field is given by [10]

$$\nabla^2 E - \frac{1}{c^2}\frac{\partial^2 E}{\partial t^2} = \frac{1}{\varepsilon_o c^2}\frac{\partial^2 P}{\partial t^2} \tag{2.15}$$

where ε_o is the electric permittivity of free space and c is the speed of light in vacuum. E is the electric field vector of the optical field and P is the polarisation density arising inside the medium in response to the optical field. In general P is a complicated function of E and can be separated into a part, which is linear in E and a second part, which is a nonlinear function of E. On a formal level, the induced polarisation P can be expressed as [10]

$$P = \varepsilon_o\left(\chi^{(1)} \cdot E + \chi^{(2)} \cdot EE + \chi^{(3)} \cdot EEE + \ldots\right) \tag{2.16}$$

where $\chi^{(i)}$ is the ith order susceptibility. The constant of proportionality, $\chi^{(1)}$ is known as the linear susceptibility, and the quantities $\chi^{(2)}$ and $\chi^{(3)}$ are known as the second- and third-order susceptibilities, respectively. In optical fibres, the lowest-order nonlinear effects originate from the third-order susceptibility, $\chi^{(3)}$. This is because solid SiO_2 is a

glass and therefore $\chi^{(2)}$ vanishes for optical fibres. Hence, the dominant nonlinear contribution to P is due to $\chi^{(3)}$ which results in effects such as third harmonic generation (THG), four-wave-mixing (FWM), and nonlinear refraction. The nonlinear processes that involve generation of new frequencies such as THG and FWM are not efficient in optical fibres. Most of the nonlinear effects are originated from nonlinear refraction, a phenomenon referring to the intensity dependence of the refractive index, which is also known as Kerr nonlinearity; the most widely studied are self-phase modulation (SPM) and cross-phase modulation (XPM) [10]. The nonlinear effects caused by $\chi^{(3)}$ are elastic in the sense that no energy is exchanged between the electromagnetic fields and the medium. There are two important nonlinear effects where optical fields transfer part of its energy to the medium, which are known as stimulated Raman scattering (SRS) and stimulated Brillouin scattering (SBS). This is a result of inelastic stimulated scattering leading to an intensity dependent attenuation constant. Another difference between stimulated scattering and the effects of nonlinear refractive index is that the former is associated with threshold powers at which their effects become significant. All of these nonlinear effects are discussed in this section.

2.3.1 Self-phase modulation, SPM

SPM results in the conversion of intensity variation to phase variation. For a silica optical fibre, the refractive index, n is directly related to the nonlinear refractive index , n_2 and the optical intensity, I as [3]

$$n = n_o + n_2 I = n_o + n_2 \frac{P_s}{A_{eff}} \tag{2.17}$$

where n_o is the linear refractive index of the fibre, P_s is the signal peak power in Watts and A_{eff} is the effective mode area in meters which is defined by

$$A_{eff} = 2\pi \cdot \frac{\left[\int \psi(r)^2 r dr\right]^2}{\int \psi(r)^4 r dr}. \tag{2.18}$$

The evaluation of the effective mode area requires the use of the modal field distribution $\psi(r)$. The effective mode area clearly depends on fibre parameters such as a core radius, core refractive index, and core-cladding index difference. In an SMF with $V = 2.4048$, A_{eff} can be approximated as πr^2 where r is the core radius. For a propagation distance of L, the nonlinear phase shift induced by SPM is given by

$$\delta\phi_{SPM} = \frac{2\pi L_{eff} n_2 P_s}{\lambda_s A_{eff}} \tag{2.19}$$

where λ_s is the signal wavelength and the effective length, L_{eff} is related to the fibre loss, α as

$$L_{eff} = \frac{[1 - \exp(-\alpha L)]}{\alpha}. \tag{2.20}$$

The intensity dependence of refractive index causes a nonlinear phase shift between the peak and its low-intensity leading and trailing edges of a signal by itself, resulting in the spectral broadening of the signal as shown in Fig. 2.7. From Fig. 2.7, different parts of the signal undergo different phase shifts. This leads to what is known as frequency chirping such that the leading edge of the pulse is down-shifted (red shift) and the trailing edge of the pulse is up-shifted (blue shift) [3]. The spectrum broadening effect caused by SPM may result in interchannel crosstalk among channels in WDM systems. Although SPM alone does not affect the intensity profile of the signal, that is no longer true in the presence of dispersion. In terms of the sign of dispersion, the operating wavelength region is divided into two regimes: normal dispersion and anomalous dispersion regimes. These

two regimes can be obtained from Eq. (2.14), in that the normal dispersion regime corresponds to the wavelength range in which dispersion D is negative (β_2 is positive) whereas the anomalous dispersion regime is the wavelength region in which D is positive (β_2 is negative). For the propagation of an optical signal, the SPM enhances the effect of dispersion when the operating wavelength is in the normal dispersion regime. That is, the signal is broadened more severely than under the effect of dispersion alone in the normal dispersion regime. Conversely, the SPM negates the effect of dispersion in the anomalous dispersion regime.

Fig. 2.7. Spectral broadening of a pulse due to SPM [3].

2.3.2 Cross-phase modulation, XPM

XPM is the nonlinear phase shift caused by interaction between two or more copropagating signals that propagate synchronously along an optical fibre [11]. XPM is always accompanied by SPM and occurs because the effective refractive index of an optical signal in a nonlinear medium depends not only on the intensity of that signal but also on the intensity of the other signals. In other words, while SPM occurs by itself, XPM occurs by interplay between other copropagating signals through fibre nonlinearities. Actually, XPM can occur between two optical fields of both the same wavelength and different wavelength. Note that in XPM, the nonlinear refractive index is twice as large as that of SPM. As a result, the nonlinear phase shift induced by XPM is given by [10]

$$\delta\phi_{XPM} = \frac{4\pi L_{eff} n_2 P_p}{\lambda_s A_{eff}} \tag{2.21}$$

where λ_s is the weaker signal wavelength and P_p is the strong pump peak power. For XPM, the effective mode area A_{eff} is defined by both the signal and pump pulses as

$$A_{eff} = 2\pi \cdot \frac{\left[\int \psi_s^2 r dr\right]\left[\int \psi_p^2 r dr\right]}{\int \psi_s^2 \cdot \psi_p^2 r dr}. \tag{2.22}$$

When pulses at different wavelengths are considered, the effect of XPM depends on the relative temporal locations of those pulses. XPM is strongest when pulses completely overlap one another. The spectra of both pulses in XPM are expected to broaden and develop multiple peaks with the outermost peaks the most intense. However, because the spectra of the pulses are governed by the combined contributions of SPM and XPM, each pulse spectrum develops asymmetric spectral broadening. In the absence of the interaction of XPM, the spectrum of each pulse would be symmetric and would exhibit less broadening. Under the presence of dispersion pulses at different wavelengths travel at different group velocities, which in effect causes pulses to walk off from one another, thus

reducing the effect of XPM [12, 13]. The larger the dispersion differences among channels, the more rapidly the pulses walk off from one another. In other words, the effect of XPM is inversely proportional to dispersion differences among channels in WDM systems. Thus, in order to minimize the impairment caused by XPM, the channel separation and/or local dispersion have to be properly chosen in WDM systems.

2.3.3 Four wave mixing, FWM

FWM occurs when photons from one or more waves are annihilated to create new photons at different frequencies for energy conservation during the nonlinear process which involve the modulation of a medium parameter such as the refractive index [14, 15]. This gives rise to the process by which signals at different wavelengths are mixed together producing new signals at new wavelengths. The difference between the processes (SPM and XPM) causing the nonlinear phase shift and the FWM process is that energy transfer occurs in the FWM process. When signals at frequencies ω_i, ω_j, and ω_k propagate along an optical fibre, the nonlinear interactions among those signals by mean of FWM result in the generation of new signals at [3]

$$\omega_{ijk} = \omega_i + \omega_j - \omega_k \quad \text{with } i, j \neq k \tag{2.23}$$

In the simplest case (one of possible solution) when only two signals at frequencies ω_1 and ω_2 are involved, the FWM generates simultaneously two symmetric sidebands at frequencies ω_3 (down-shifted) and ω_4 (up-shifted) in frequency such that

$$\omega_3 + \omega_4 = \omega_1 + \omega_2 \tag{2.24}$$

$$\omega_3 = 2\omega_1 - \omega_2 \tag{2.25}$$

$$\omega_4 = 2\omega_2 - \omega_1 \tag{2.26}$$

as demonstrated in Fig. 2.8. If the frequencies of the two pump waves are equal, $\omega_1 = \omega_2$ it is relatively easy to satisfy the phase-matching requirement given by [10]

$$\Delta\beta = \frac{\left(n_3\omega_3 + n_4\omega_4 - n_1\omega_1 - n_2\omega_2\right)}{c} = 0. \tag{2.27}$$

This specific case is called degenerate FWM or three-wave mixing because only three distinct frequencies are involved in this nonlinear process. The phase mismatch $\Delta\beta$ in Eq. (2.27) generally represents the difference of propagation constants β of the original signals and the FWM-generated signals. The FWM efficiency decreases with the increase in the phase mismatch $\Delta\beta$. When N signals are involved in the FWM process, the number of FWM generated signals is given by [3]

$$M = \frac{N^2}{2}(N-1). \tag{2.28}$$

For example, when 10 signals are four-wave mixed together, 450 signals are generated. In WDM systems, not only does the FWM cause power depletion on the participating channels, but it also results in crosstalk among channels. The crosstalk comes from the fact that some of the FWM-generated signals can have the same frequencies as the WDM channels when all channels are equally spaced in frequency. One approach to avoid crosstalk is to employ unequally spaced channel allocation [16, 17]. In this method, all channels are allocated so that the FWM-generated signals do not have the same frequencies as the channels. It should be noted that in this method only crosstalk is avoided, but the signals still suffer excess power loss. In relation with the dispersion, the channel spacing has to be sufficiently large in the optical fibres with small dispersion, to avoid phase matching [17]. On the other hand, channels can be packed closer together if the dispersion is large.

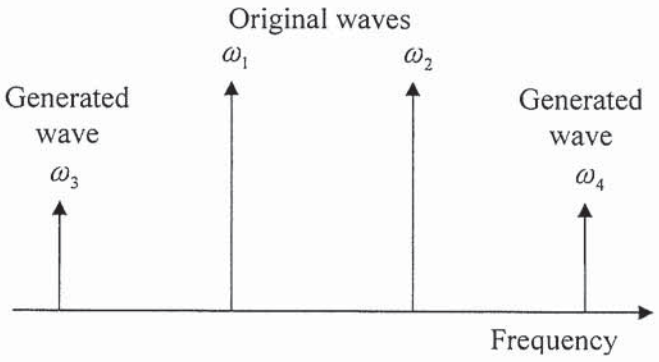

Fig. 2.8. Four wave mixing for two channels.

2.3.4 Stimulated Raman scattering, SRS

SRS is the result of interaction between incident light and molecular vibration. Some portion of the incident light is downshifted in frequency by an amount equal to the molecular-vibration frequency, which is generally called the Stokes shift [18]. This in effect depletes the optical power of the incident light. When there is only a single light wave propagating along the optical fibre, Raman scattering results in the generation of spontaneous Raman-scattered light waves at lower frequency. In general, the criterion used to determine the level of scattering effects is the threshold power, P_{th} defined as the input power level that can induce the scattering effect so that half of the power (3-dB power reduction) is lost at the output of an optical fibre of length, L. For single-channel lightwave systems, it has been shown that the threshold power, P_{th} is given by [10]

$$P_{th} \approx \frac{16A_{eff}}{g_R L_{eff}} = \frac{32\alpha A_{eff}}{g_R} \tag{2.29}$$

where α and A_{eff} are the attenuation coefficient and effective core area of an optical fibre given by Eq. (2.22), respectively, and g_R is the Raman gain coefficient. In general, g_R depends highly on composition and dopants of fibre core materials, and is inversely

proportional to the pump wavelength. Commonly, the transmitted power is well below 1 W; thus, the effect of SRS is negligible in single-channel systems. The effect of Raman scattering is different when two or more signals travel along an optical fibre. When two optical signals separated by the Stokes frequency travel along an optical fibre, the SRS would result in the energy transfer from the higher frequency signal to the lower frequency signal [18]. That is, one signal experiences excess loss whereas another signal gets amplified. The signal that is amplified is called the probe signal whereas the signal that suffers excess loss is called the pump signal. The effectiveness of the energy transfer depends on the frequency difference (Stokes frequency) between the pump and probe signals. In WDM systems, the channels at shorter wavelengths will act as pump signals and suffer excess loss. It is clearly seen that the SRS affects the two channels differently. In WDM systems, the chance that all channels transmit signals simultaneously decreases with the increase in the number of channels. This decreases the effect of SRS. The effect of SRS is also reduced under the presence of dispersion [19]. The walk-offs among channels decreases the effect of SRS, hence increasing the threshold power. In general, SRS is not the limiting factor in lightwave communication systems compared with the other nonlinear effects due to its high threshold power.

2.3.5 Stimulated Brillouin scattering, SBS

SBS is due to the interaction between the incident light and acoustic vibration in the optical fibre. SBS is also referred to as nonlinear collinear acousto-optics [20]. Similar to SRS, stimulated Brillouin scattering causes frequency down-conversion of the incident light, but the frequency shift in this case is equal to the frequency of the interacting acoustic wave. The frequency shift of the Stokes wave in SBS is smaller by three orders of magnitude than that of SRS. The acoustic waves generated by the optical power affect the

density of a material and thus change its refractive index. This refractive index fluctuation can scatter light; this effect is called the Brillouin scattering. However, unlike Raman-scattered light, the Brillouin-scattered light propagates in the backward direction. This in effect causes excess loss on the incident light similar to SRS. For SBS, the threshold power is given by [21]

$$P_{th} = 42\frac{\alpha A_{eff}}{g_B}\left(1+\frac{\nu_p}{\nu_B}\right) \tag{2.30}$$

where g_B is the Brillouin gain coefficient, ν_P is the signal linewidth, and ν_B is the Brillouin gain bandwidth. The fibre loss, α is the same at both the Stokes and pump frequencies due to the small value of the Brillouin shift. The Brillouin-gain coefficient g_B is larger than g_R by more than two orders of magnitude. When the ratio between the signal spectral width, ν_p and the Brillouin gain bandwidth, g_B in Eq. (2.30) is taken into account, the threshold power increases significantly, especially when the bit rate is high. Since the gain bandwidth, ν_B is very small, there are no nonlinear interactions among WDM channels due to SBS. Therefore, in order to avoid SBS the power of each WDM channels, not the total power of all transmitted channels, has to be kept below the threshold. Due to its high threshold power, P_{th}, the effect of SBS is negligible when the operating bit rate is sufficiently high, which is generally satisfied in practice.

2.4 Multichannel lightwave systems

In optical communication systems, the signal bandwidth can exceed 1 THz because of such a large carrier frequency associated with the optical signal, thus resulting in the potential of carrying information at bit rates in the order of 1 Tb/s [1]. In practice, however, the bit-rate is often limited to tens of Gb/s or less due to fibre impairments, such

as losses, dispersion, and nonlinearities, and the slow response time of electronic components required for optical signal processing. Therefore, the development of multichannel lightwave systems which transmit signal information through multiple optical channels over the same fibre has attracted considerable attention to enhance transmission capacity. High capacities in these systems can be achieved by using various multiplexing techniques. Channel multiplexing can mainly be performed in either time or wavelength using optical domain techniques. It is common to refer to the former case as Optical Time-Division Multiplexing (OTDM) and the latter case as Wavelength-Division Multiplexing (WDM). The light wave systems making use of such techniques are referred to as multi-channel communication systems.

2.4.1 Optical time-division multiplexing, OTDM

In OTDM systems, optical pulses from various sources carrying the information are time multiplexed [9]. In these systems, the pulse width reduces with the increase in number of users when bit rate per user is fixed. Such a system requires the optical sources which generate very narrow width optical pulses. The output of these sources is then externally modulated depending upon the information to be transmitted. If internal modulation is used on commonly used laser sources, pulse compression has to be applied to generate narrow pulses. Such a compression is generally achieved using nonlinear processing. In OTDM, the pulses from various sources require very tight delay adjustment so that pulses can be multiplexed together. Further, exact timing information is required at all the receivers for demultiplexing which can be obtained by centralised clock or synchronised distributed clocks. In high speed OTDM systems, each channel has to be extracted from an ultrahigh-speed signal stream at bit rates of gigabits per second. This requires the OTDM to have a very narrow transmission window of a few picoseconds. All-optical fibre

based nonlinear interferometric switches, such as nonlinear optical loop mirror, can provide narrow gating window for demultiplexing, but their size is bulky and they have poor efficiency. Semiconductor optical amplifier (SOA)-based interferometric switches, are small in size and require much less switching energy to switch out the selected OTDM channel.

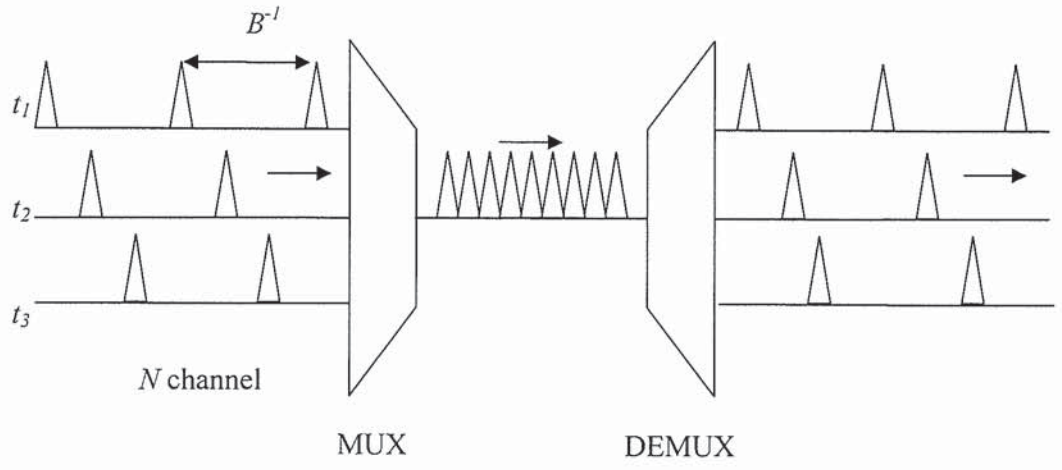

Fig. 2.9. Optical Time-Division Multiplexing systems.

From Fig. 2.9, optical signals modulated at the bit-rate B in each channel with different delay time are multiplexed optically to form a composite optical signal at the bit-rate NB, where N is the number of multiplexed optical channels. The width of the optical pulse generated by a transmitter should be less than $(NB)^{-1}$ to ensure that the pulse will fit within the allocated time slot. The multiplexing of N channels can be achieved by a delay technique with the fibre segments of controlled lengths, which is optically implemented such that the modulated optical signals in nth branch is delayed by an amount $(n-1)/(NB)$, where $n=1, \ldots, N$. The demultiplexing of the individual channels in OTDM systems can be achieved by either electro-optical or all-optical techniques. All-optical techniques are

more common because electro-optical techniques require a variety of components and its performance is limited by the speed of modulator. Moreover, all techniques for demultiplexing in OTDM systems require control signals at the same bit-rate of a single channel, requiring an all-optical scheme because of the high bit rates associated with OTDM systems.

2.4.2 Wavelength-Division Multiplexing, WDM

A WDM system is similar to frequency division multiplexed (FDM) radio broadcasting systems. A technique by which two or more optical signals having different wavelengths are combined and simultaneously transmitted in the same direction over one fibre. At the end of the transmission link, they are demultiplexed into individual channels by means of optical techniques. Fig. 2.10 shows the basic diagram of WDM systems. Ideally, the information in various channels does not interfere with each other. However, interchannel interference may occur when the information passes through optical amplifiers or any other nonlinear device in the link. Generally, implementation of WDM systems require couplers, wavelength multiplexers and demultiplexers, tunable or fixed wavelength sources and detectors capable of operating over the entire wavelength range. There are two main issues which must be tackled in a WDM system i.e. wavelength stability of sources and channel spacing. If the transmitter source wavelength is not stable, it may drift towards the neighbouring wavelength channels. Consequently, channels spacing will reduce resulting in crosstalk. Various wavelength stabilizing schemes have been proposed to avoid drift [22]. Most of these schemes compare the transmitting wavelength with a reference and adjust the transmitting source wavelength continuously. Channel spacing is an important issue. Smaller spacing implies more channels in a given spectral range. But

the demultiplexers resolution decides the spacing. For smaller channel spacing, narrow bandwidth filters are required.

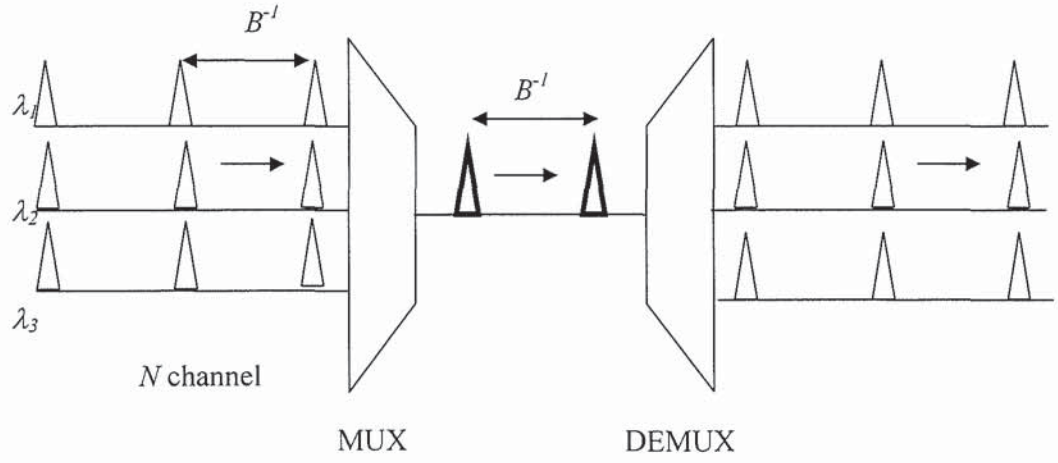

Fig. 2.10. Wavelength-Division Multiplexing systems.

Chapter 3

Semiconductor Optical Amplifier Nonlinear Loop Mirror (SOA-NOLM)

3.1 Introduction

Semiconductor optical amplifiers (SOA) constitute important building blocks as nonlinear elements in all-optical signal processing applications. The widespread use of SOAs [23-31] has arisen due to several of their advantageous attributes. They are generally small in size, reasonably efficient, maintenance free, and relatively inexpensive. They require only low power current sources, can be frequency modulated by a direct modulation of injection current, and have been demonstrated to operate at longer wavelengths from the near ultraviolet to the far infrared [23]. The disadvantage of the SOA as a nonlinear medium is however, that most nonlinear effects are associated with the dynamics of the carrier density. As a result, the response time is limited by the recovery time of the carrier density in the SOA (carrier density dynamics), which is typically a few hundred picoseconds. However, the fast nonlinear gain dynamics in the SOA make them attractive candidates in a variety of nonlinear processing applications, such as wavelength conversion, regeneration and ultra fast switching in an optical network. Presently, the SOAs also known as semiconductor laser amplifiers (SLAs) are among the primary contenders for integrated all-optical devices. The large gain of SOAs allows switching with pulse energies on the order of or less than a picojoule, and various functionalities have been demonstrated in a number of different schemes at high speed e.g. wavelength conversion at 168 Gb/s [24]. All-optical processing schemes are often designed around a simple structure which exploits some of the nonlinear effects that occur in the SOAs. One of the most widely adopted schemes is the Nonlinear Optical Loop Mirror (NOLM) [25],

an interferometric structure which can be customized to obtain different behaviours. For example it can be used for pedestal suppression, noise reduction, wavelength conversion, and OTDM demultiplexing. The first NOLMs were based on a silica fibre nonlinearity, therefore it required long fibre lengths and high optical peak powers due to the small nonlinear coefficient. More recently, NOLMs have been constructed which do not depend on the fibre nonlinearity but on the optical nonlinearity of the SOA. This device, referred to as an SOA-NOLM or SLALOM (SLA in a Loop Mirror), can be integrated on a chip. The extended SOA-NOLM, known as a TOAD (Terahertz Optical Asymmetric Demultiplexer), has been widely used for demultiplexing applications [26-31]. The TOAD consists of the SOA which is asymmetrically placed within a short fibre loop. Data streams at rates as high as 160 Gb/s have been demultiplexed down to 10 GB/s using this device [31]. The SOA-NOLM therefore has great potential for use in future generation OTDM networks.

In this chapter, the basic properties and operating characteristics associated with an SOA are presented. Then, the operation of a NOLM and an SOA-NOLM are discussed in detail. The experimental results for an SOA-NOLM are shown and analysed. This device will be used in subsequent chapters in all-optical processing applications.

3.2 Semiconductor optical amplifier

A semiconductor optical amplifier is basically a semiconductor laser without feedback which is operated as a broadband single-pass device for amplification. Thus, analysis of the SOA stems from the well known analysis of semiconductor lasers: the creation of a population inversion that renders stimulated emission more prevalent than absorption. The population inversion is achieved by electric current injection into the p-n junction, as in a

semiconductor laser. The basic SOA structure, as depicted in Fig. 3.1, is similar to that of a laser in which the active region is comprised of a double heterostructure or quantum well structure. A SOA has two facets, and the reflectivities of these facets decide whether the device will operate as a SOA or a semiconductor laser. When the facet reflectivities are zero, input signals pass through the device only once. Such an amplifier is called a travelling wave amplifier (TWSOA). If the reflectivities are non-zero but quite small, the signal passes through the cavity several times. This type of SOA is called a Fabry-Perot amplifier (FPSOA). The FPSOA enables considerable amplification at low injection currents, but it is more sensitive to fluctuations in bias current, temperature and signal polarisation compared to the TWSOA. In addition, the gain spectrum of the FPSOA exhibits ripples caused by the reflections at the end facets, which make the device strongly frequency dependent. The FPSOA also has disadvantages for pulsed applications due to the envelope waves produced by the optical waves running back and forth within the FP cavity. This exhibits multimode characteristics and leads to undesirable effects such as mode-hopping and pulse broadening, which limits the bit rate-distance, BL due to fibre dispersion. Therefore, the TWSOA has replaced the FPSOA in many applications.

In a double-heterostructure (DH) semiconductor laser, the active region consists of a material with a narrow band gap which is sandwiched between n-type and p-type cladding regions with wider band gaps. Carriers are injected into the device active region from the applied bias current and confined to the active region due to the potential barriers provided by the wide band gap materials as shown in Fig. 3.2. If large enough currents are applied, large concentrations of electrons and holes are built up in the active region, leading to population inversion. Photons passing through the active region can stimulate radiative recombination of the carriers, resulting in amplification of a light wave. It is in the central

intrinsic region that the carrier density is high enough to impart gain to the light wave. The carriers can also decay spontaneously, leading to amplified spontaneous emission (ASE), or they can decay through non-radiative processes. Thus, the carrier density or concentration is determined by the balance between the applied current and the decay of carriers. The amplification or gain of the SOA can be controlled by the injection current. The active region also has a higher refractive index than the cladding regions and so behaves as a dielectric waveguide with a rectangular cross-section [32]. The waveguided light must be efficiently coupled in and out of the amplifier usually to single-mode optical fibre. Single transverse mode operation with two polarisations, the TE and the TM, can improve the coupling efficiency from the device to optical fibre. There are two important parameters that describe the SOA i.e. optical gain and saturation output power. The amplifier gain will saturate if the input power is too high, and it is not possible to discriminate the signal from the spontaneous emission if the input signal is too low.

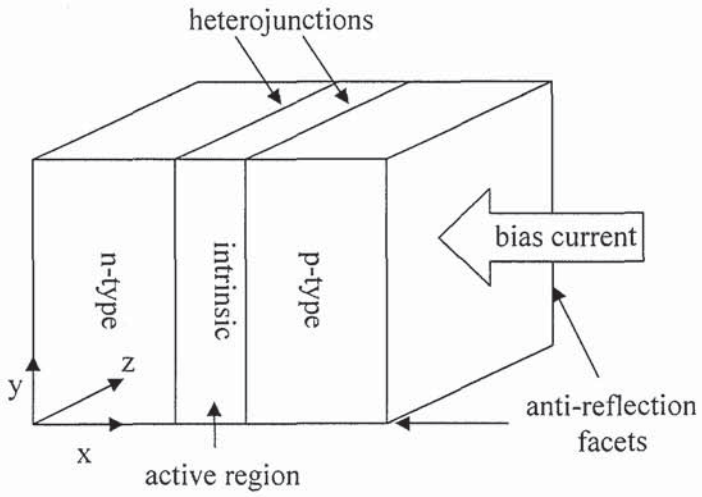

Fig. 3.1. Cross section of a SOA.

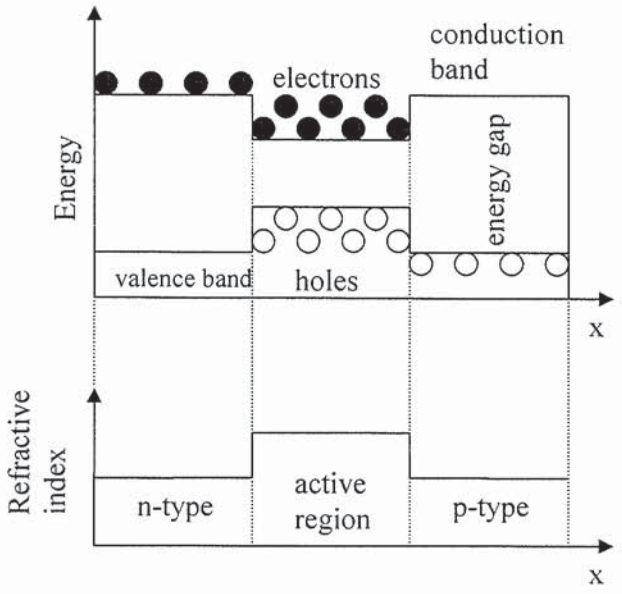

Fig. 3.2. Carrier confinement in a SOA.

3.2.1 Nonlinear gain

Gain in a semiconductor arises from the exchange of energy between the photons in the incident optical field and the electrons and holes in the semiconductor. This occurs via the processes of absorption, stimulated emission, and spontaneous emission. When an electron absorbs the energy in a photon, it is excited to a higher energy level (conduction band), leaving behind a hole at the lower energy level (valence band). Conversely, an electron at a high energy level may recombine with a hole at a lower energy level, emitting a photon in the process. When this process is initiated by an existing photon in the semiconductor, it is called stimulated emission. Otherwise, it is called spontaneous emission. The rate of these various processes is strongly dependent on the carrier population densities. The carrier density, N in the conduction band is a measure of the device gain, and is related to the optical power of the incident light stream $P(t)$ by the rate equation [33];

$$\frac{dN}{dt} = \frac{I}{eV} - \frac{N(t)}{\tau_e} - \frac{P(t)\Gamma g[N(t) - N_T]}{h\nu A} \tag{3.1}$$

where I is the effective injection current, e is the electron charge, V is volume of the active region, N_T is the carrier density at transparency, τ_e is the carrier lifetime, Γ is the mode confinement factor, g is the gain coefficient, $h\nu$ is the photon energy, and A is the cross-sectional area of the active region. The first term on the right-hand side of Eq. (3.1) refers to the amount of carriers pumped into the active layer, and subsequently allows population inversion to be achieved. The second term describes all non-radiative (i.e. carrier loss) processes through the carrier lifetime and also accounts for the spontaneous emission. The last term denotes the decrease in electrical carrier density through stimulated emission during the amplification process. In the steady state Eq. (3.1) is set to zero, and a solution may be obtained for N.

In optical amplifiers, it is experimentally observed that gain of amplifier reduces as the input signal power increases. This phenomenon is called gain saturation. The primary interest with this gain saturation phenomena is the output saturation power, P_{sat} which is defined as the amplifier output power when the gain has dropped to half of the value at very low input powers. This value of the output power at the -3 dB point, is defined by [34]

$$P_{sat} = \ln(2)\frac{h\nu A}{\Gamma A_g \tau_e} \tag{3.2}$$

where A_g is the differential gain coefficient (often expressed as dg/dN). The corresponding saturation output intensity I_{sat} can be used to describe the gain saturation effect in the optical amplifier by using equation [35]

$$G_s = \exp\left[\frac{g_o L}{1 + I_{out}/I_{sat}}\right] \tag{3.3}$$

where G_s is the single pass gain, g_o is the unsaturated gain coefficient, L is the length of the amplifier, and I_{out} is the output light intensity. The gain starts to decrease when the draining rate of inverted population is higher than the pumping rate. Thus, the amount of population inversion can not be maintained constantly because of the energy conservation. In a WDM system, if the total power of all the channels exceeds P_{sat}, the amplifier will be saturated. It is clearly seen from Eq. (3.2) that amplifier saturation is determined by the material properties A_g and τ_e. In practice τ_e is inversely proportional to carrier density, so operating at high bias currents leads to an increase in P_{sat}. High saturation output power is a desirable SOA property because it allows a wider range of input powers.

There are two other nonlinear gain effects which are known as spectral hole burning (SHB) and carrier heating (CH). The SHB is due to the fact that an incoming short optical pulse interacts only with a certain part of the carrier distribution, depending on the photon energy and the spectral width of the pulse. The pulse causes a reduction (hole) in the carrier distribution at the particular photon energy, resulting in a deviation from the Fermi distribution. This SHB decreases the gain in the gain regime and increases the gain in the absorption regime. The Fermi distribution is mainly restored by carrier-carrier scattering that leads to an increase in the effective carrier temperature, which is called carrier heating. The distribution cools down to the lattice temperature through phonon emission. The increase in temperature decreases the gain across the entire spectrum.

For amplification of optical signals, operation of the SOA within a linear region is preferred. However, in all-optical switching schemes, the nonlinear behaviour is exploited. Typically, the control pulse is used to modify the carrier density within the SOA. The signal pulse on the other hand, is weak such that it will not significantly alter the carrier dynamics of the SOA, but rather experience the altered SOA medium. The variation of the carrier density results in an associated phase change for an incident light pulse propagating through the SOA.

3.2.2 Noise figure

An SOA, along with the amplified signal, also produces amplified spontaneous emission (ASE) noise. The noise originates from the spontaneous emission in the active gain region. The ASE plays an important role in the SOA structure as it saturates the active medium, while reducing the gain. When the amplified signal and accompanying ASE noise are incident on a photo detector, the noise beats with itself and also with the signal. Thus ASE-ASE and ASE-signal beat noise components are produced. The noise figure, F_n defines as the signal-to-noise ratio at the input over the signal-to-noise ratio at the output can be expressed as [35]

$$F_n = \frac{(S/N)_{in}}{(S/N)_{out}} \tag{3.4}$$

where (S/N) is the signal-to-noise ratio. Essentially, the noise figure is determined by the ratio between ASE power and gain. The minimum F_n of an ordinary optical amplifier is 3 dB while a typical value for an SOA is in the range between 6-10 dB.

3.2.3 XPM and XGM

Nonlinearities in SOAs are generally caused by the amplifier input signals that change the distribution of the carrier density. There are two different types of nonlinear effects which are commonly used in all-optical processing systems. The first type includes nonlinear effects in which new frequency components are generated by the data and control signal inside the medium (e.g. FWM). The second type includes nonlinear effects in which the phase or amplitude of the data signal propagating through the medium is altered by changes of the nonlinear refractive index or gain, induced by optical control signals (e.g. XPM, cross-gain modulation (XGM)). In the absence of the control signal, a signal pulse will experience SPM. This SPM changes the pulse shape and its spectrum. If two signals are injected into the SOA, there will be XPM between the signals. The XPM only causes phase changes; therefore an interferometric configuration is necessary to convert phase changes to intensity changes. Three common interferometers used in SOA functional applications are the Mach-Zender, Michelson and Sagnac [37]. In all interferometers, the SOA is placed in one or more of the interferometer arms in order to change the phase of the propagating pulse. The fast recovery time of the SOA allows high speed switching at speeds comparable to typical data rates. Optical switching using a nonlinear interferometer makes it possible for one optical signal to control and switch another optical signal through the nonlinear interaction in the SOA. The presence of a strong control pulse (pump) changes the refractive index of the medium given by

$$\Delta n = n_2 I \tag{3.5}$$

where Δn is the change in the refractive index of the medium, n_2 is the nonlinear refraction coefficient and I is the intensity of light incident on the medium. A change in the index adds a phase shift between the two arms of the interferometer, so that the input signal

(probe) is switched over to a second output port. This method of switching based on XPM is schematically shown in Fig. 3.3.

One way to implement XPM-based switching is to use a Sagnac interferometer [38], where one of the output ports also serves as the input port for the signal to be switched. This configuration is commonly referred to as the Nonlinear Optical Loop Mirror (NOLM). If the SOA is present in the NOLM it is called a SOA-NOLM or TOAD/SLALOM. Other applications of SOAs may be found in the area of wavelength conversion and signal regeneration.

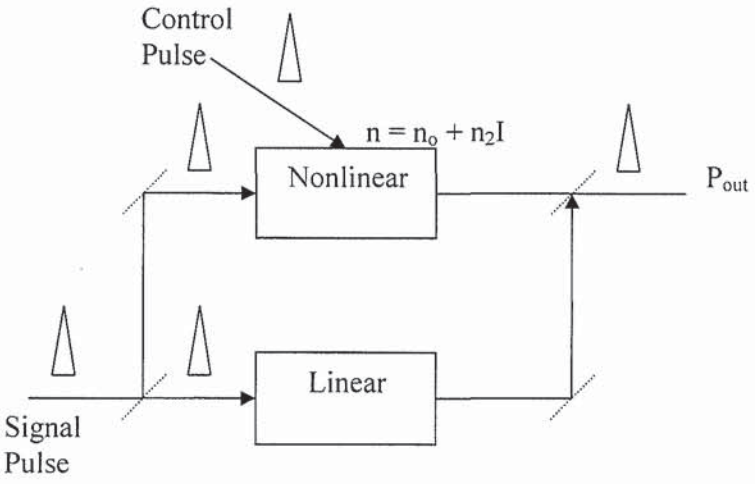

Fig. 3.3. All-optical interferometric switching using XPM.

Cross-gain modulation (XGM) uses an input signal to saturate the gain and thereby modulate a continuous wave (CW) signal at a desired output wavelength. Wavelength conversion at 100 Gbit/s using XGM in SOAs has been demonstrated [39]. Although simple to implement, the XGM gate has a number of shortcomings, such as inversion of the input-control signal and the relatively large chirp of the output signal due to the large gain modulation. The basic principle of cross-gain modulation is illustrated in Fig. 3.4. The input signal (pump) is used to saturate the gain and thereby modulate the CW signal

(probe) at the desired output wavelength. The output signal, λ_2, is inverted from its original signal, λ_1. This signal is typically smaller than the actual data because of the modulation when passing through the SOA. The output power is dependent on the gain characteristic of the SOA as shown in Fig. 3.4(b). Obviously, the injected current into the SOA can be adjusted to observe the maximum output power in this XGM effect.

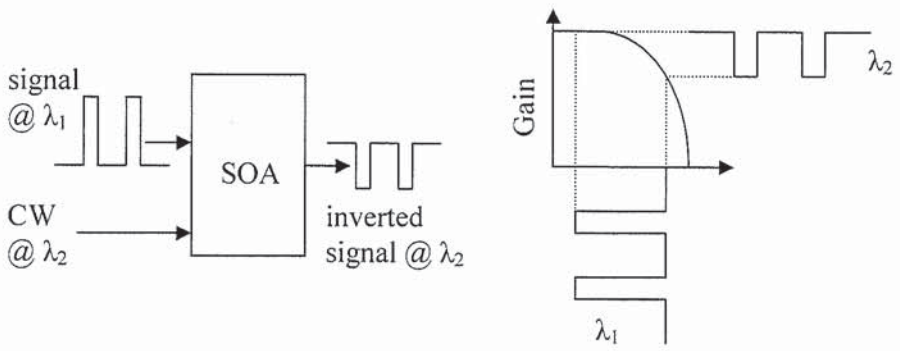

(a) SOA configuration (b) XGM mechanism

Fig. 3.4. Cross-gain modulation, XGM.

3.3 Nonlinear loop mirror, NOLM

The NOLM is actually a nonlinear Sagnac interferometer where one of the output ports also serves as the input port for the signal. The exploited nonlinear phenomenon can be self-phase modulation or cross-phase modulation. An XPM-based NOLM is shown in Fig. 3.5. This technique can be used for OTDM switching. Light entering the NOLM is split at the coupler and travels clockwise and counter clockwise around the loop, which subsequently combines again at the coupler. A strong control pulse (or pump) is injected into the loop such that it propagates in only one direction inducing a nonlinear phase shift only on the clockwise propagating wave. The nonlinear optical effect of the control pulse is to induce a refractive index change, Δn, which is experienced fully by a co-propagating

signal pulse. This refractive index change results in a differential phase shift, $\Delta\phi$, between the counter-propagating signal pulses as they arrive back at the input coupler, given by

$$\Delta\phi = k(\Delta n)L \tag{3.6}$$

where k is the wave vector and L is the path length over which the induced index change Δn is effective. The signal and the control must be at different wavelengths so that the second one can be suppressed using a band pass filter. The transmission equation for the NOLM may be stated as [42]

$$T = {}^{P_{out}}\!/_{P_{in}} = [1 - 2\alpha(1-\alpha)(1+\cos(\Delta\phi))] \tag{3.7}$$

where P_{in} is the power incident at the input port, P_{out} is the power transmitted to the output port, and α is the power split ratio on the input coupler. The NOLM transmission is maximised for the differential phase shift of odd multiples of π and minimized for even multiples of π phase shift. It was shown that for a phase difference of $\Delta\phi = 0$ the Sagnac interferometer works as a mirror and all incoming light is reflected. In the NOLM the phase difference is induced by XPM through optical control or pump pulses, inserted into the fibre loop via a second coupler.

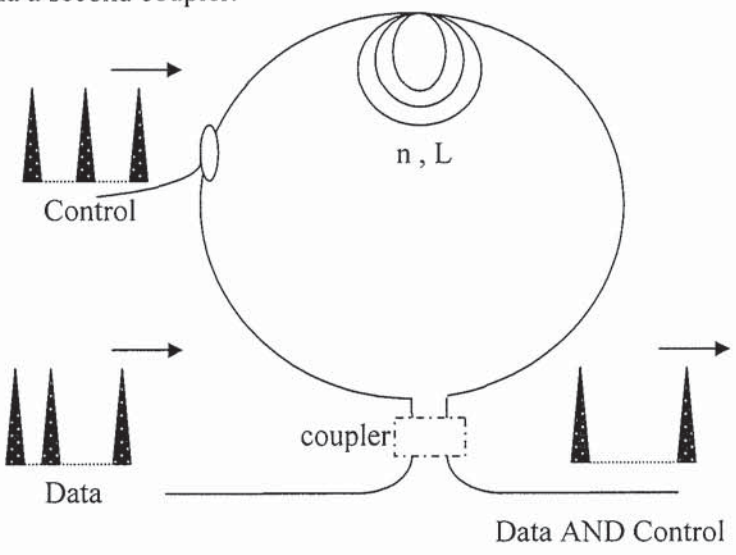

Fig. 3.5. The Nonlinear Optical Loop Mirror (NOLM).

3.4 SOA-NOLM

The SOA-NOLM (sometimes referred to as the TOAD) is essentially a nonlinear Sagnac interferometer. The optical nonlinearity is provided by gain saturation of the SOA [26, 33]. Many all-optical switching demonstrations have been performed using the SOA-NOLM [44-47]. In the SOA-NOLM switch, an incoming data signal is split by a 3 dB coupler into two components, which propagate through the fibre loop in opposite directions. The SOA is placed slightly asymmetrically in the fibre loop, so that the two data components reach the SOA at different times. After one circulation in the loop, both components interfere again at the 3 dB coupler. The nonlinear effect in the loop is a phase displacement induced by SOA saturation due to the presence of a control pulse. The control pulse induces a phase change between the two counter-propagating data components. The gain and phase curves for clockwise and anticlockwise propagation are not the same. The reason is that the clockwise pulse is co-propagating with the control pulse and experiences a constant gain and phase shift, while for the counter-propagating anticlockwise pulse the gain and phase shift is changing during propagation through the SOA. Fig. 3.6 shows the schematic of the SOA-NOLM. The displacement of the SOA, Δx, from the centre of the loop determines the switching window. Different widths of the switching windows are obtained by changing the position of the SOA in the fibre loop using an optical delay line (DL). If the control pulse passes through the SOA between co-propagating and counter-propagating pulses, only the last is affected by a phase shift due to the SOA saturation. So, if the phase difference between the pulses is π, then the two components interfere constructively at the 3 dB coupler. The polarization controller in the loop is used to adjust the birefringence of the loop, thereby adding a fixed relative phase shift between the two signal pulses. If they are in phase, they will be directed to the output

port. If they are out of phase, they will be reflected back to the input port. The transmission and reflection intensities are [54]

$$I_r = I_{in}\alpha(1-\alpha)x[G_{cw} + G_{ccw} + 2\sqrt{G_{cw}G_{ccw}}\cos(\phi_{cw} - \phi_{ccw}) \tag{3.8}$$

$$I_t = I_{in}[\alpha^2 G_{cw} + (1-\alpha)^2 G_{ccw} - 2\alpha(1-\alpha)\sqrt{G_{cw}G_{ccw}}\cos(\phi_{cw} - \phi_{ccw}) \tag{3.9}$$

where I_r is the reflected intensity, I_t is the transmitted intensity, I_{in} is the input intensity, G and ϕ are the gain and phase changes for clockwise (cw) and counter clockwise (ccw) components respectively. There are mainly three ways to achieve phase and gain differences [33] i.e. by

1) saturating the SOA by a single pulse travelling in the cw direction,
2) saturating the SOA by two pulses, separated by time T, travelling in the ccw direction, or
3) saturating the SOA by the control pulse between the transition of the cw and ccw pulses.

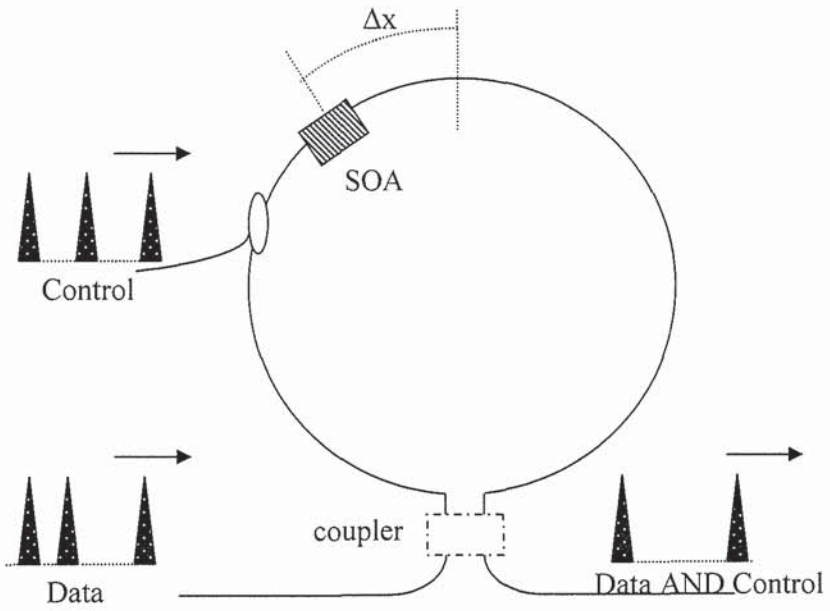

Fig. 3.6. The SOA-NOLM.

The SOA-NOLM is quite versatile in terms of possible wavelength and polarisation assignments for the control and signal pulses. In principle, it can be made to operate independent of the signal and control polarisations. This mode of operation requires that the signal and control pulses be at different wavelengths so that a band pass filter may be used to distinguish them at the output of the switch. On the other hand, if the incoming signal polarisation is fixed, one can make the control pulse polarisation orthogonal to the signal. In this configuration, the signal and control inputs may operate at the same wavelength and a polariser may be used to distinguish between the two at the switch output.

There have been successful demonstrations of different optical functionalities using configurations based on the SOA-NOLM. These include demultiplexers [48, 49] and the implementation of simple Boolean functions such as AND, NOT and XOR for address recognition [33, 50]. More sophisticated Boolean functions such as bit adders [51, 52] and parity bit generators [53] have been demonstrated using a combination of several SOA-NOLM-based gates.

3.5 Experiment and results

Nonlinear effects in a semiconductor optical amplifier (SOA), i.e. self-phase modulation (SPM) or cross-phase modulation (XPM), have been used in this thesis to achieve the presented optical signal processing functions. These nonlinear effects are the results of nonlinear gain and index dynamics in the SOA. In this section, data are presented about the SOAs used in the experiments. Two SOAs which are labelled SOA#1 and SOA#2 are characterised in terms of gain, saturation output power, and gain recovery time. The

SOA#1 is a 500 μm module SOA1550MRI supplied by Opto Speed while the second is a 1000 μm bulk 1550-SOA-01778 packaged by BT Laboratories. Firstly the SOA gain is shown as a function of the driving current. Afterwards, the SOA gain saturation is presented as a function of the optical CW output power. The recovery time of the SOA is achieved by using a pump-probe technique. Then, these two SOAs are used as a nonlinear element in SOA-NOLM#1 and SOA-NOLM#2 respectively. Switching curves for both SOA-NOLMs are plotted and discussed in this section too.

3.5.1 Gain saturation

The experimental setup employed to characterise the SOA gain as a function of the driving current as well as a function of the optical output power is shown in Fig. 3.7.

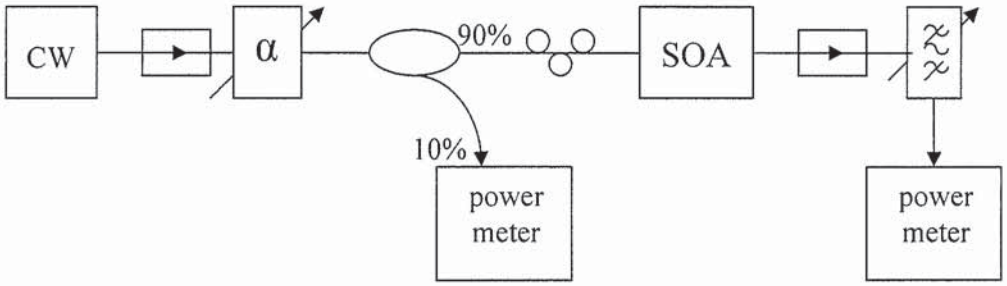

Fig. 3.7. Setup for measurement of SOA's gain.

The scheme consists of a laser source emitting CW light at a wavelength of 1550.5 nm. The CW light is passed through an isolator and a variable attenuator, before being split using a 90:10 coupler. The 10% branch is used to monitor the input power into the SOA. The remaining 90% light is injected into the SOA via a polarisation controller placed at the input of the SOA. The polarisation controller allows the light source to be aligned with

the high-gain (TE) mode of the SOA. Another isolator is employed at the output of the SOA to isolate the device from possible reflection. A band pass filter (BPF) is centred at the probe wavelength to filter any ASE generated by the SOA. This is because the amplified ASE is present in the amplifier output along with the amplified light.

Firstly the fibre-to-fibre SOA gain is measured as a function of the driving current. In this case, the input light is fixed at an input power of -20 dBm to avoid device saturation. The SOA is initially driven at low injection current and gradually increased to the maximum current. The coupling losses at the back-to-back connector are estimated to be 0.5 dB (i.e. average measured losses in the loop) at each side of the SOA. The measured SOA gains versus drive currents at two different operating temperatures and wavelengths are shown in Fig. 3.8 and Fig. 3.9 respectively. These two figures show that the SOA's gain is temperature and wavelength dependent. The choice of the wavelength for both SOAs is in the region of 1550 nm. There is a 2 dB variation in the SOA's gain within the operating wavelength region of 1540 nm to 1550 nm. The above procedure is repeated for drive currents at 120 mA, 160 mA and 200 mA for SOA#1, and 80 mA, 120 mA and 180 mA for SOA#2, and varying input power at 20°C. Note that the maximum possible injected current into SOA#1 is 200 mA and SOA#2 is 180 mA. The fibre-to-fibre SOA gain is shown as a function of the optical output power, P_{out} in Fig. 3.10. The gain of SOAs reduces with the increase in input power level. This reduction arises due to gain saturation. It is observed that the fibre-to-fibre gain for SOA#1 is 20 dB when biased at 200 mA, where as for SOA#2 is 12 dB when biased at 180 mA. The saturation output power of the SOA#1 and SOA#2 is measured to be equal to 3.85 dBm and 0.5 dBm respectively.

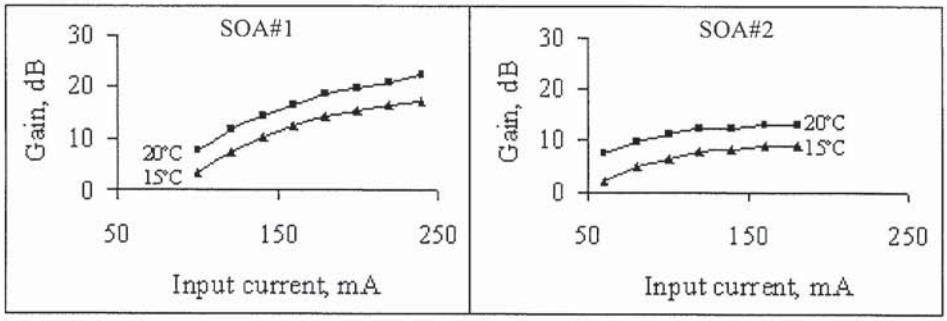

(a) (b)

Fig. 3.8. Gain dependency on temperature for (a) SOA#1 and (b) SOA#2.

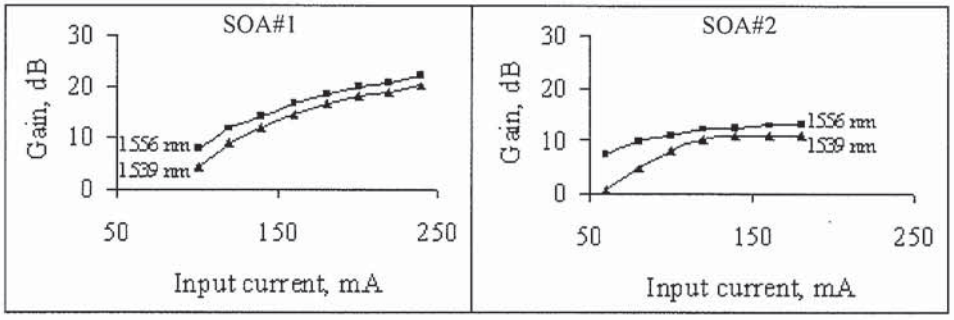

(a) (b)

Fig. 3.9. Gain dependency on wavelength for (a) SOA#1 and (b) SOA#2.

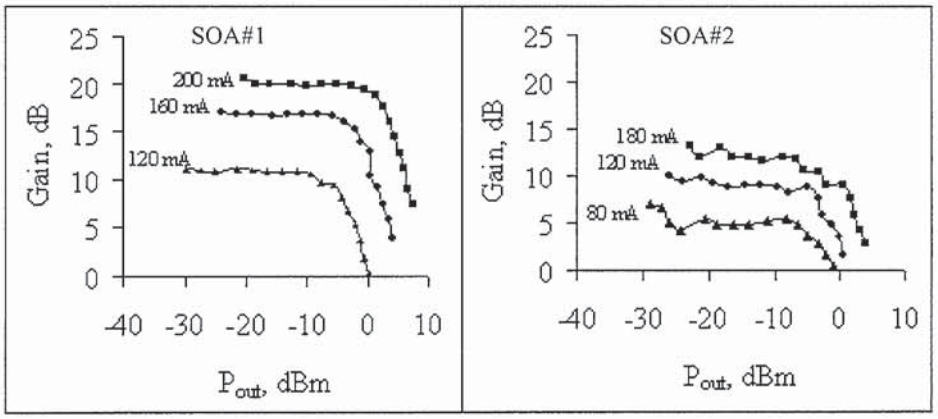

(a) (b)

Fig. 3.10. Saturation output power for (a) SOA#1 and (b) SOA#2.

3.5.2 Gain recovery time

The gain recovery time is measured using an experimental setup shown schematically in Fig. 3.11. A pump-probe technique is used, where weak probe pulses sample the gain and phase changes induced by strong pump pulses. The optical pulse for the pump is generated by a gain-switched distributed feedback laser (DFB) laser with a 1557.4 nm wavelength and a 2.5 GHz repetition rate, the full wave half maximum (FWHM) width of the pulses is 25 ps. A 1550.5 nm CW-DFB laser is used as the probe beam. The pump or control pulse is amplified before being sent through an isolator into a 50:50 coupler. The probe signal is coupled via the same 3 dB coupler and then both signals are injected into the SOA through a polarisation controller. The state of polarisation is adjusted to the maximum gain, which corresponds to the TE mode. The probe beam is filtered at the output and monitored using a sampling oscilloscope. The pump and probe powers are 6 dBm and -5 dBm respectively.

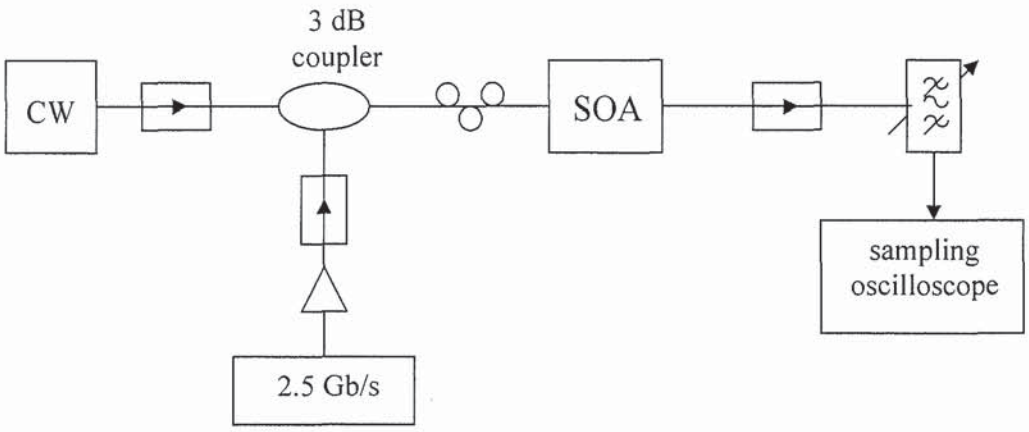

Fig. 3.11. Gain recovery time measurement technique.

Fig. 3.12 depicts the gain recovery for both SOA#1 and SOA#2. For a drive current of 200 mA, the gain recovery is 300 ps in the case of SOA#1. In SOA#2, the gain recovery is 400 ps.

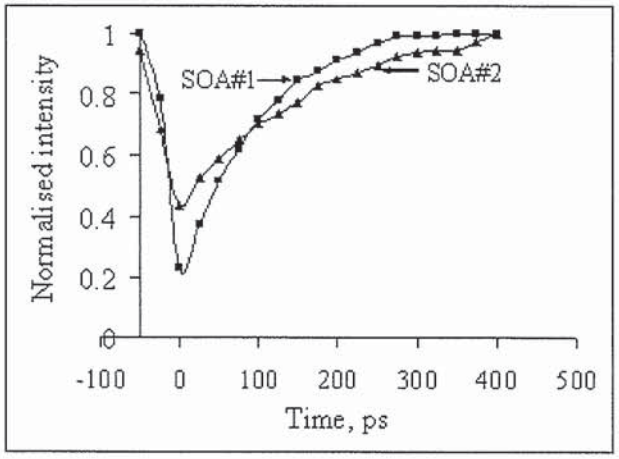

Fig. 3.12. Gain recovery of SOA#1 and SOA#2.

3.5.3 All-optical switching

The experimental setup for switching with SOA-NOLMs is the same as Fig. 3.6 given in section 3.4, but no control pulse is applied. An SOA is offset in the loop by varying the delay line to give a switching window of ~140 ps. Two polarisation controllers are employed to switch the pulse into minimum transmission or maximum reflection state. The power of the input pulses is controlled using an optical attenuator. The power of the reflected, R, and transmitted, T, pulses is measured after being filtered by a band pass filter. This procedure is repeated for different injection currents of the SOA. The SOA is biased in the gain regime. The results are plotted as shown in Figs. 3.13 and 3.14. Note that in these figures the horizontal axis represents the average input energy. It is expected to see more significant nonlinear switching when P_{in} is sufficiently large. The switching energies are 0.46 pJ for SOA-NOLM#1 and 1.2 pJ for SOA-NOLM#2 when driven by their maximum biased current of 200 mA and 180 mA respectively.

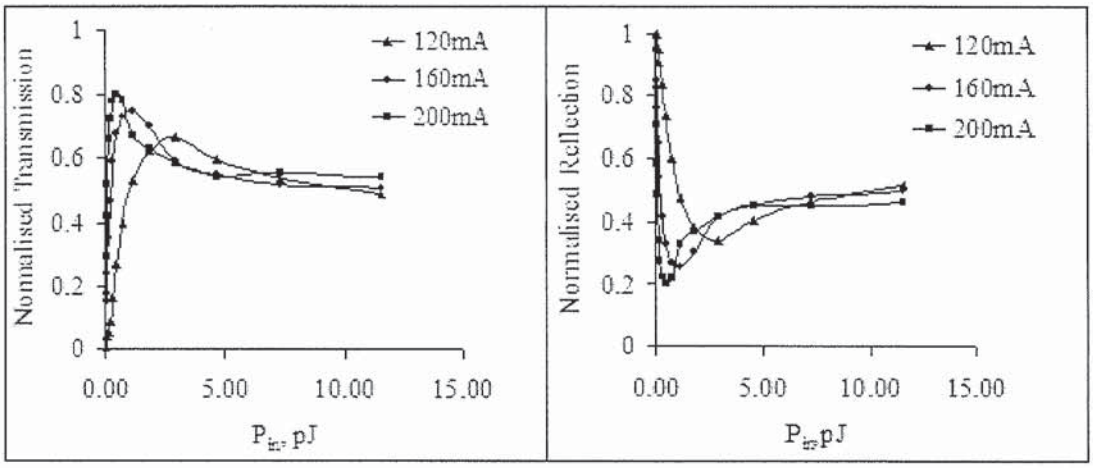

(a) (b)

Fig. 3.13. Self-switching of SOA-NOLM#1 for bias currents of 120 mA, 160 mA, and 200 mA : (a) Transmitted power, and (b) Reflected power.

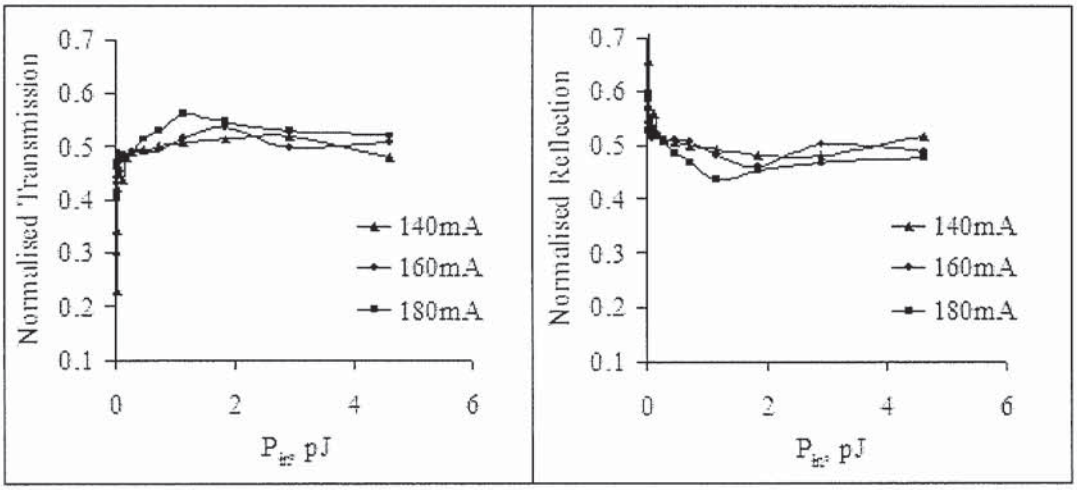

(a) (b)

Fig. 3.14. Self-switching of SOA-NOLM#2 for bias currents of 140 mA, 160 mA, and 180 mA : (a) Transmitted power, and (b) Reflected power.

A simulated result for SOA-NOLM#1 for two injected currents i.e. 120 mA and 200 mA is shown in Fig. 3.15. The simulation results are obtained from a SLALOM model developed by W.M.Wong [55]. The modelled switching curves show good agreement with the measurements for all currents.

However, there are no results from the model similar to experimentally observed switching curves of SOA-NOLM#2. This is because no good match could be found. All the switching curves which are obtained from the model have similar trend with the plotted graphs in Fig. 3.15. The same trend for the simulated and the experiment is not observed in the case of SOA-NOLM#2.

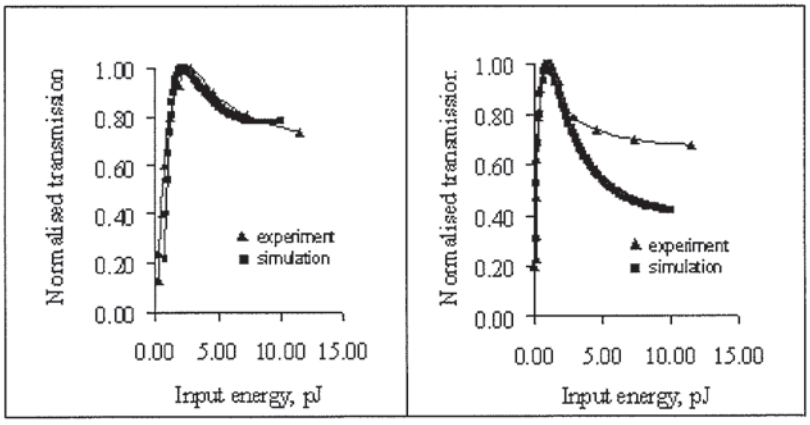

(a) (b)

Fig. 3.15. Simulation results for transmission of SOA-NOLM#1 at (a) 120 mA, and (b) 200 mA.

The maximum transmitted power, denoted as P_p, corresponds to π phase difference and is plotted against the input current as shown in Fig. 3.16(a). In this figure, 70% to 80% power is transmitted if the SOA#1 is biased in corresponding to a current of 140 to 200 mA. For SOA-NOLM#2, only 50% power is transmitted if the SOA is biased between 120

to 180 mA. The reduction of the transmitted power is due to the fact that there are losses in the loop including coupling-losses. Fig. 3.16(b) demonstrates the maximum switching energy for each injected current. It is clearly seen that the switching energy decreased with the injected current. This is because the carrier density is higher when the bias current is increased. Thus, less energy is required to perform switching.

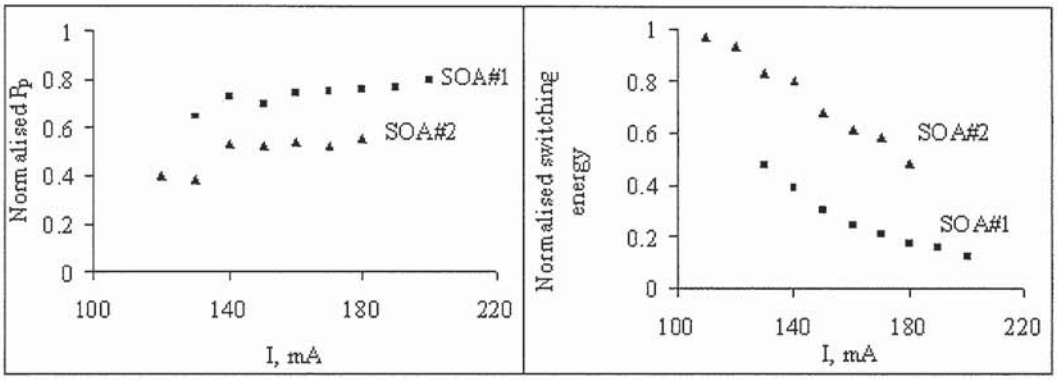

(a) (b)

Fig. 3.16. Normalised switching characteristics of SOA-NOLM#1 and SOA-NOLM#2 for (a) maximum transmitted power and (b) switching energy.

3.6 Conclusion

From the above results, SOA-NOLM#1 has been chosen for studying the application of SOA-NOLMs in the next chapters. This is because the SOA-NOLM#2 did not show good agreement with the theoretical model. It is worth to mention that SOA#2 is possibly partially damaged and is not suitable for future works. The gain and the saturation output power for SOA-NOLM#1 are 20 dB and 3.85 dBm respectively.

Chapter 4

Carrier-Suppressed Return-To-Zero (CSRZ): Generation and Transmission

4.1 Introduction

During the past decade, tremendous advances have been made to fully use the optical bandwidth provided by the fibre in high speed optical systems and networks. The traditional ways of encoding i.e. non return-to-zero, NRZ and return-to-zero, RZ have been challenged by various modulation formats. Carrier-suppressed return-to-zero (CSRZ) modulation is one of the recently proposed modulation formats for high bit rate transmission systems, which has been numerically and experimentally investigated [56, 57]. This format is RZ-based modulation and has been demonstrated as one of solutions to relieve optical systems impairments such as nonlinearities and dispersion. The main target of this modulation format is a reduction of the nonlinear impacts in a transmission line and an improvement of the spectral efficiency in high bit rate WDM systems. The CSRZ optical signal has no carrier component and therefore in multi wavelength systems, it is less sensitive to four wave-mixing (FWM) if compared to NRZ. Additionally, the dispersion tolerance of the transmission can be improved due to its reduced spectral width compared to conventional RZ modulation [58, 59].

In this chapter, CSRZ generation using an SOA-NOLM will be introduced. The generated CSRZ is characterised for one wavelength and multiple wavelengths within the SOA's spectral bandwidth. This is followed by single channel and four channel WDM transmission in a 194 km fibre recirculation loop. The transmission section of this chapter

has been done in collaboration with Dr.M.M.Nahas who was also a Ph.D. research student in PRG, Aston University.

4.2 Carrier-suppressed return-to-zero, CSRZ

Optical carrier suppression can be used in applications where one wishes to eliminate the carrier or increase the modulation depth of an optically modulated signal. A conventional technique for carrier suppression is to bias a Mach-Zehnder modulator around the minimum transmission point, such that the optical carrier destructively interferes at the interferometer's output, leaving only the sideband modulations. Fig. 4.1(a) shows the setup of the conventional 40 Gb/s CSRZ generation [60].

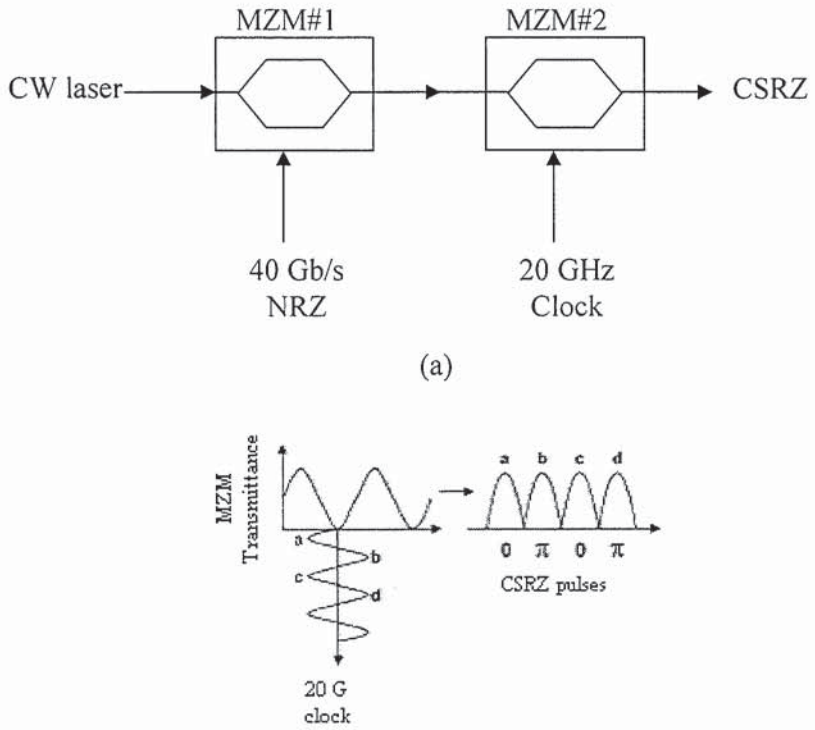

Fig. 4.1. (a) Conventional setup for 40 Gb/s CSRZ signal and (b) CSRZ pulses.

The first modulator, MZM#1 is driven with a 40 GHz electrical NRZ signal at the quadrature point of the modulator power function. This will generate a 40 Gb/s NRZ optical signal at the wavelength of the external CW-pump light. The second modulator is driven by a 20 GHz clock signal and biased at a minimum transmission point so that the relative optical phase of the generated RZ signal alternately takes values of 0 and π. Therefore, the phase difference is kept constant at π. The cascading of these two modulators provides a means to generate 40 Gb/s RZ modulation with carrier suppression. The CSRZ signal is realised in the second modulator, MZM#2 which can be described mathematically [61] as,

$$E_{out} = jE_{in}\sin\left[\frac{(\phi_1 - \phi_2)}{2}\right]\exp\left[\frac{(\phi_1 + \phi_2)}{2}\right] \tag{4.1}$$

where E_{out} and E_{in} describe the optical input and output fields of the MZM#2. ϕ_1 and ϕ_2 are the optical phases of the two modulator arms which are defined as

$$\phi_1 = \frac{\pi}{2}\sin(\omega_o t + \pi) = -\frac{\pi}{2}\sin(\omega_o t) \tag{4.2}$$

$$\phi_2 = \frac{\pi}{2}\sin(\omega_o t) \tag{4.3}$$

respectively. The frequency of the sine-clock amounts to $f_o = 20\,\text{GHz}$. It is important to notice that there is a π phase difference between adjacent pulses as shown in Fig. 4.1(b). The CSRZ pulses possess a RZ signal shape.

4.3 CSRZ generated by SOA-NOLM

The SOA-NOLM has proven to be an attractive device in performing all-optical format conversion [62, 63]. The format conversion is based on gain variation by an intensity-dependent phase change in the SOA-NOLM. Fig. 4.2 shows the schematic diagram for

format conversion from RZ and NRZ to CSRZ. This set up can also be used to change the converted CSRZ back to their original formats RZ and NRZ.

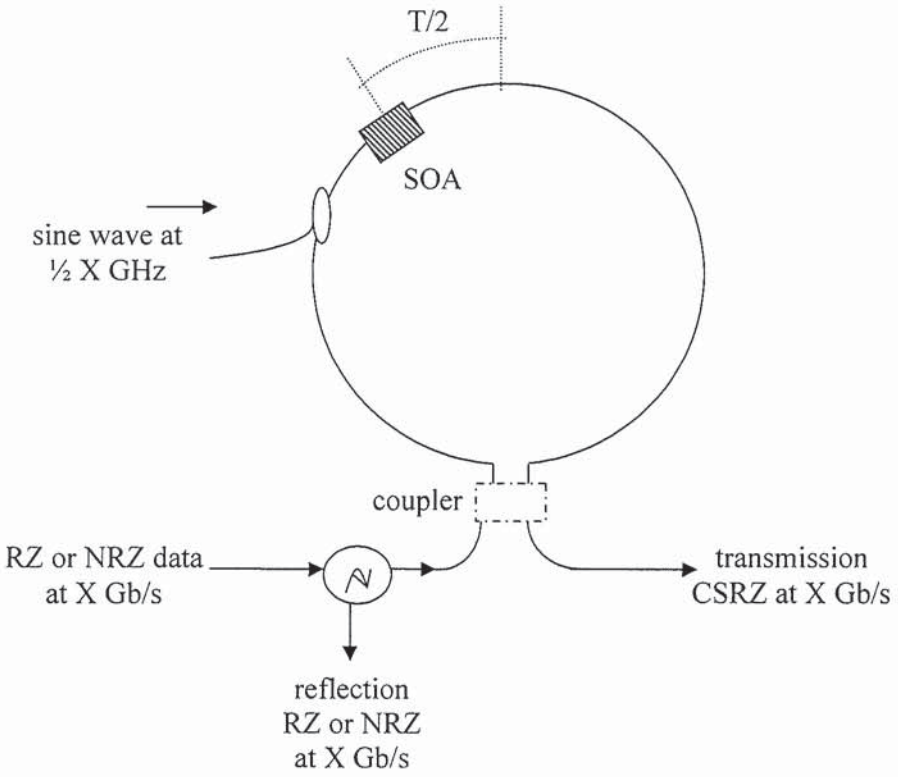

Fig. 4.2. SOA-NOLM converter.

The signal at the reflection and transmission port of the SOA-NOLM can be described by Eqs. (3.8) and (3.9) respectively. The optical spectra for both ports are illustrated in Fig. 4.3. These spectra are obtained from a VPI model of the CSRZ generation using an SOA-NOLM [64] developed at Aston University. The carrier component of the CSRZ signal spectrum in Fig. 4.3(a) is suppressed due to the modulation of the phase delay. The spectrum of the optical data can be seen at the reflection port as in Fig. 4.3(b).

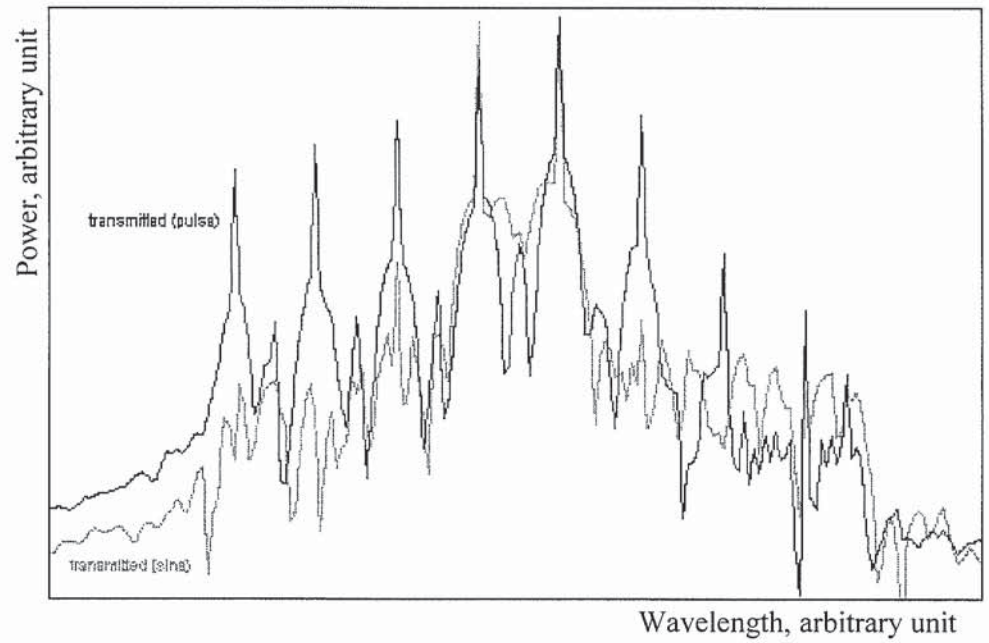

(a)

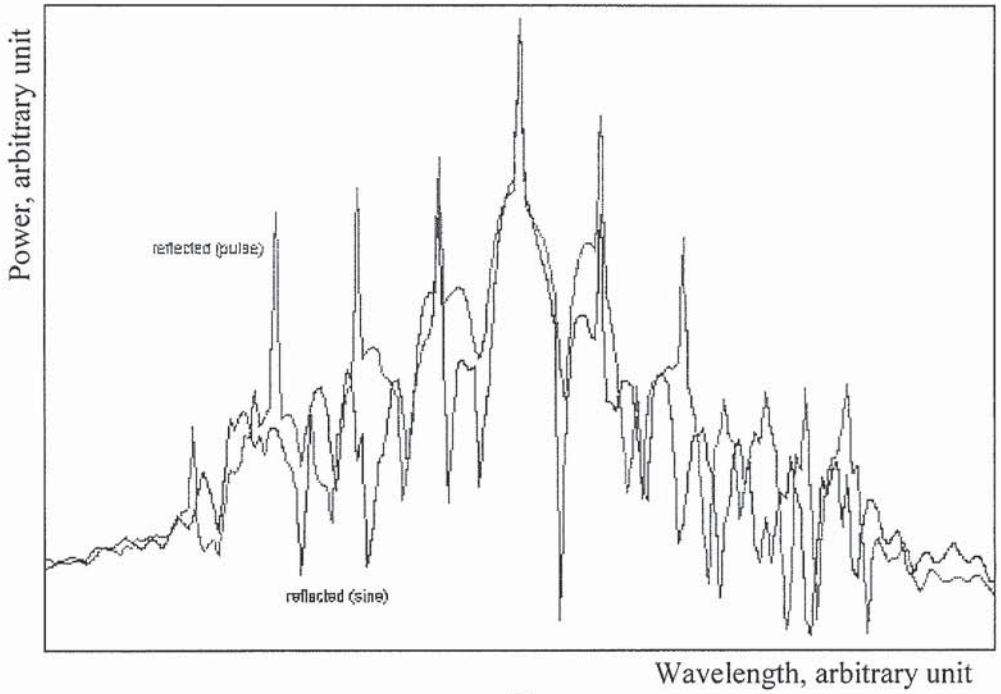

(b)

Fig. 4.3. Simulated spectra of SOA-NOLM converter at (a) transmission port and (b) reflection port.

From Fig. 4.2, if the control pulse is absent, the clockwise, cw, and counter clockwise, ccw, signal experiences the same gain and phase changes in the loop. Therefore, no output will be seen at the transmission port because of the destructive interference between the two signals. The converted signal will be observed only when the control signal is properly applied into the loop. This can be explained by a diagram shown in Fig. 4.4.

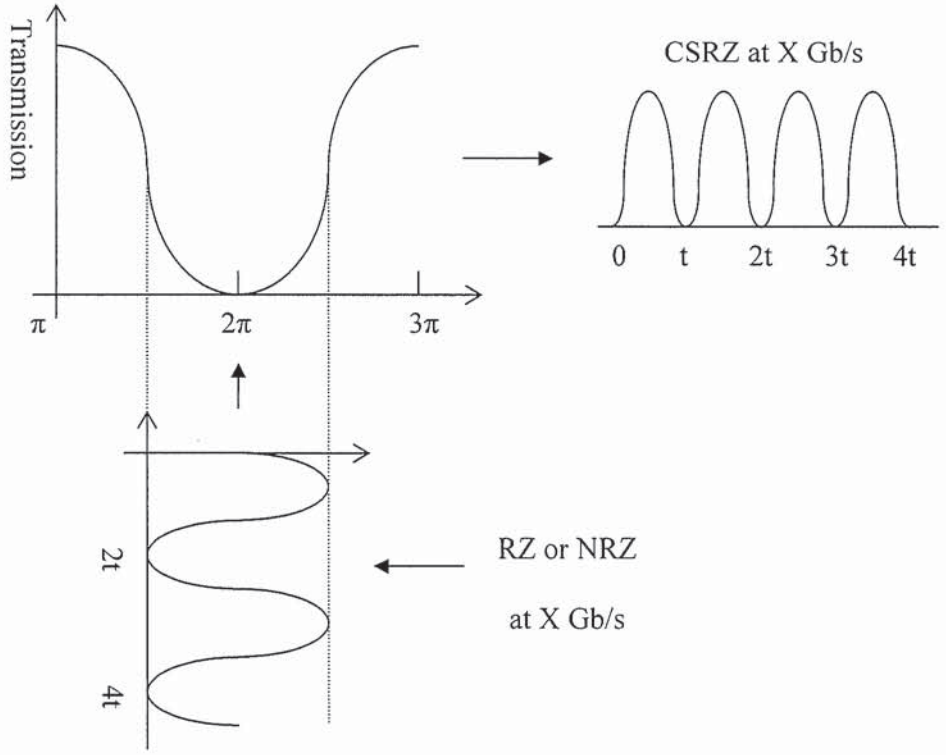

Fig. 4.4. CSRZ generation.

The conversion is implemented by biasing the loop mirror at around (0, 2π, ..) i.e. a minimum transmission point. The control beam which is a sinusoidal optical wave at half the data channel clock frequency is used to modulate the phase delay of the cw and ccw signal. This beam will cause the refractive index in the SOA's active region to change periodically. The refractive index change results in a differential phase shift, $\Delta\phi$, which is given by Eq. (3.6). Upon entering the coupler the differential phase modulation is converted to amplitude modulation. The output will show a sequence of data bits

alternating in phase between zero and π and therefore the input NRZ or RZ data signal is converted into a CSRZ signal. According to the theory in [33], the reflection port sees an original data signal i.e. RZ or NRZ. If the phase delay is adjusted from 2π to π, the interference will be constructive; hence the input NRZ or RZ signal is switched out of the SOA-NOLM without changing its modulation format [44]. The recovery time of the SOA will be the limiting factor at high speed operation because of the inadequate phase modulation depth due to the long recovery time. The SOA's recovery time can be enhanced (i.e. reduced) by injecting CW light that couples with the control signal [65]. The converter can be extended to higher speeds by properly optimising the input power ratio of the optical clock and CW [62].

The same results are observed using an OptSim model of CSRZ converter as given in Fig. 4.5. The simulated spectra are depicted in Fig. 4.6. The OptSim model in Fig. 4.5(a) is classified into seven building blocks. Each block is represented in Fig. 4.5(b) with its specified function. Blocks III and V represent the optical inputs for multi-channels (WDM) system and the receiver sensitivity measurement respectively. All parameters that are used in the simulation are almost the same as the experimental values except the SOA's bias current which is slightly higher i.e. 300 mA. Blocks I and II are control pulses at 10 Gb/s and CW source that generates sine wave at 5 GHz respectively. The delays and the attenuators in I, control the arrival of the pulses and the optical power at the SOAs. The simulated results using the OptSim for single channel and WDM system are presented in sections 4.4 and 4.5.

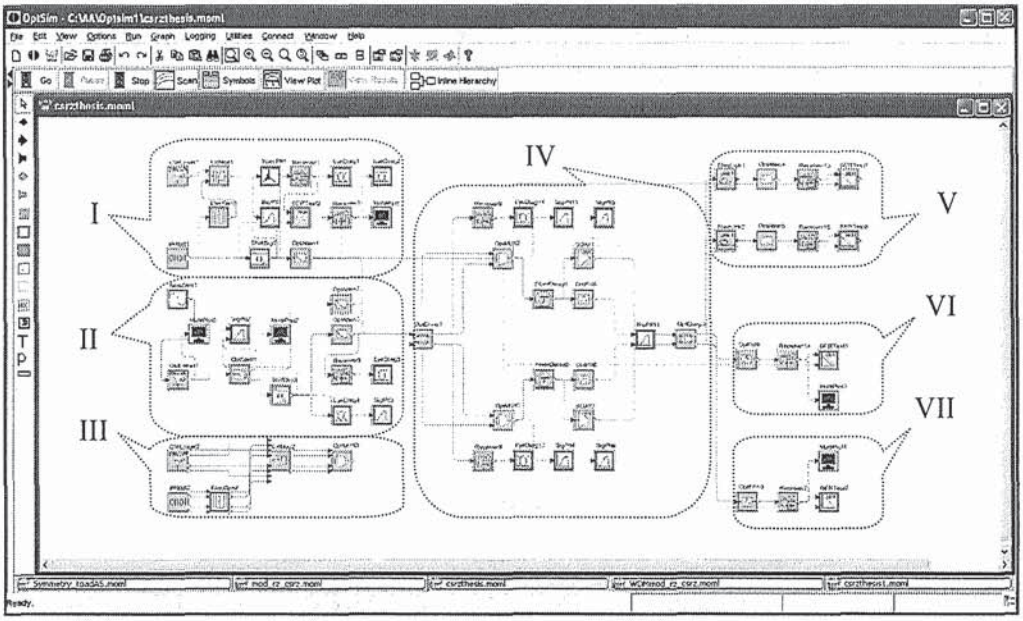

(a)

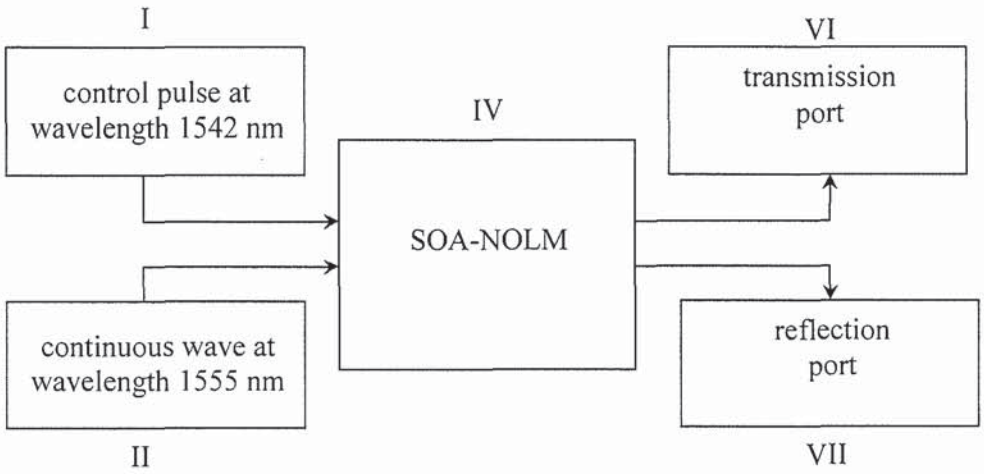

(b)

Fig. 4.5. (a) SOA-NOLM converter obtained from OptSim. (b) Simplified SOA-NOLM converter from (a).

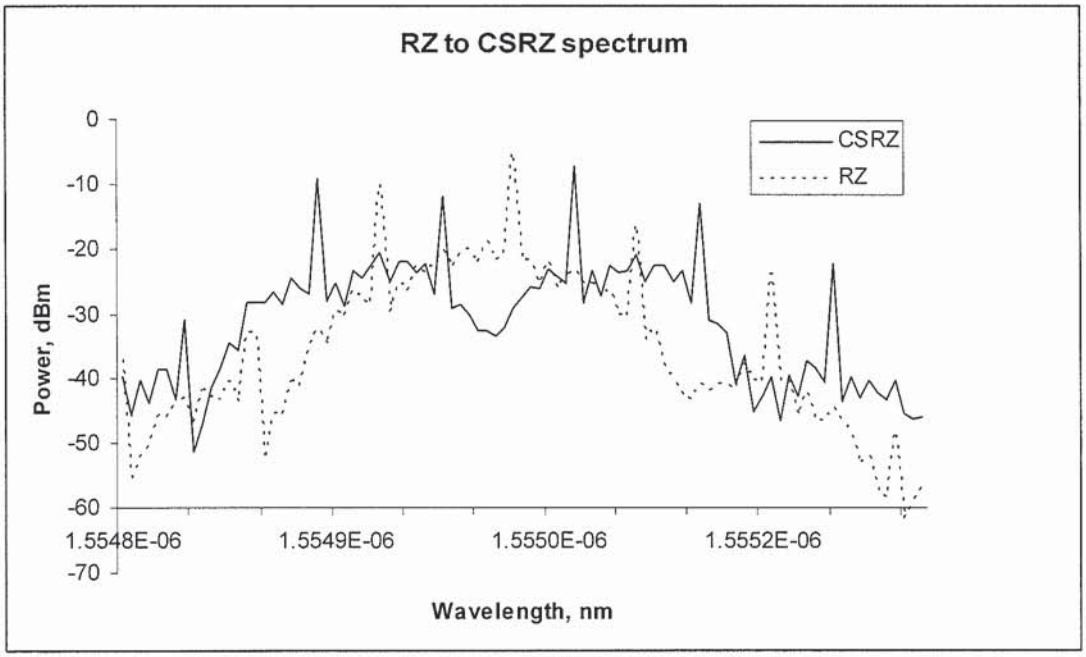

(a)

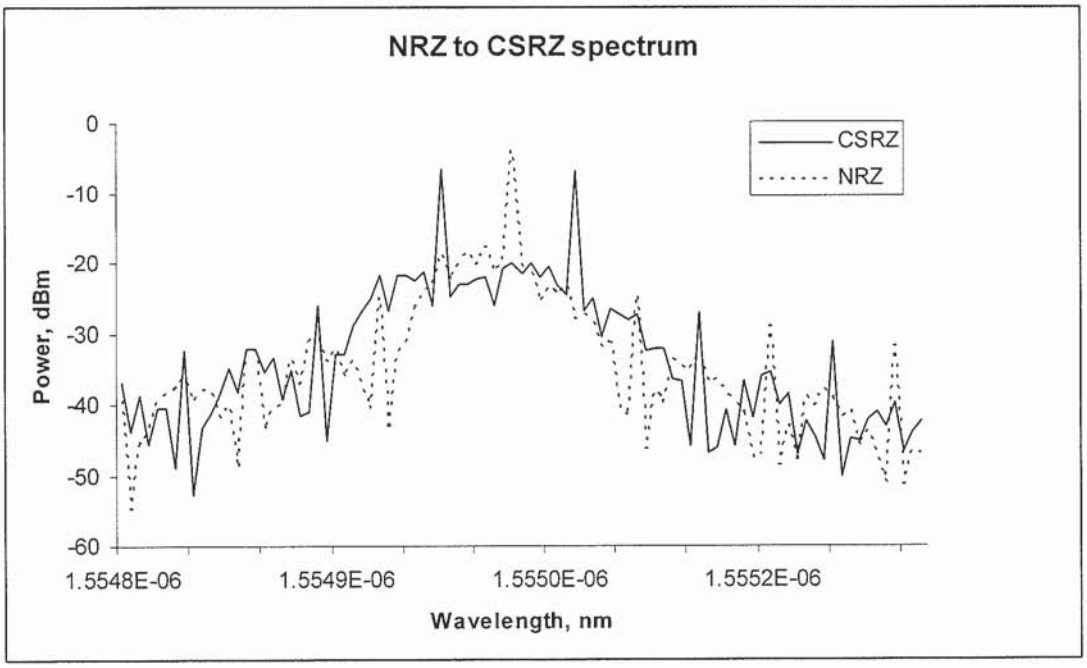

(b)

Fig. 4.6. Simulated spectra of SOA-NOLM converter for (a) RZ to CSRZ and (b) NRZ to CSRZ.

4.4 CSRZ generation: experiment and results

This section investigates the CSRZ generated for a single channel and a four channel WDM system. Fig. 4.7 shows the experimental setup for the format conversion using the SOA-NOLM. The optical data is generated by driving the $LiNbO_3$ electrooptic modulator with a pulse pattern generator (PPG) at 10.7 GHz producing a pseudorandom bit sequence (PRBS) of length 2^{31}-1. A tuneable laser unit with multiple channels is used as a CW source for the single channel and WDM system. In the WDM experiment, the four channels are evenly separated. These sources are chosen to be within the SOA's gain bandwidth range i.e. from 1528 nm to 1565 nm. The resultant data stream is amplified and launched into the converter. The SOA-NOLM comprised of a 50/50 coupler with polarisation controllers (PCs) on each arm, a 50/50 coupler on the clockwise path and a 140 ps SOA offset from the centre by a variable optical delay line on the clockwise arm. The SOA provided a peak fibre-to-fibre gain of 20 dB, and a saturation output power of 3.85 dBm when biased at 200 mA. A CW DFB laser with a wavelength of 1542.3 nm is modulated at 5.35 GHz, delayed and coupled, via a 50/50 coupler, into the SOA-NOLM at a power of 3.2 dBm. A variable optical delay line, to adjust the control pulse arrival time relative to the data, controlled the phase seen by the clockwise and counter clockwise data at the SOA. On the output of the SOA-NOLM a tuneable grating band pass filter with a 3 dB bandwidth of 0.24 nm is used to extract the 1542.3 nm control wavelength. This filter is employed only for a single channel conversion. In the WDM experiment, the tuneable grating filter is replaced by a WDM coupler with an extinction ratio of 37 dB. The WDM coupler allows all data to propagate along the fibre whilst it rejects the control pulse. For the SOA-NOLM bandwidth measurements, the WDM coupler is removed. The reason for this is to pass all the wavelengths within the SOA's bandwidth. However, the control pulse is filtered out by putting a fibre Bragg grating (FBG) with a 3 dB bandwidth of 1.1

nm and isolation of 19.8 dB in place of the WDM coupler. A circulator (Cir2) is used to prevent the filtered control pulse from re-entering the SOA-NOLM. The output of the SOA-NOLM is monitored and measured on a digital sampling oscilloscope, optical spectrum analyser (OSA), power meter and bit error rate test (BERT) set.

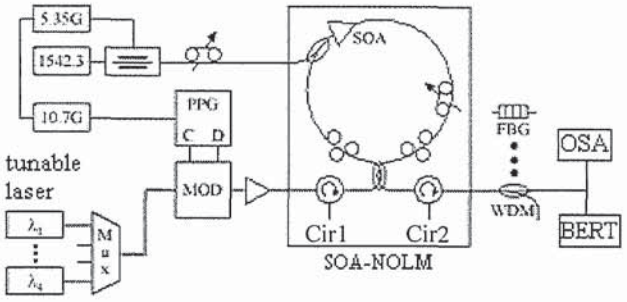

Fig. 4.7. Experimental setup of SOA-NOLM.

4.4.1 Single channel

Fig. 4.8 shows the spectrum and corresponding eye diagram for conversion of NRZ-to-CSRZ and RZ-to-CSRZ. It is observed from Fig. 4.8(b) and (d) that the spectrum of the CSRZ signal has two half-clock-rate frequency components at 5 GHz and the carrier is suppressed. The spectral width between the two first spectral side-bands is reduced. The length of these side-bands is 0.08 nm which corresponds to a 10 GHz data signal. The whole spectrum shows a narrower width by 0.015 nm if compared at the noise floor which is around -40 dBm in Fig. 4.8. This comparison is made for the same OSA's setting in all measurements. From the eye diagram (inset in Fig. 4.8), we see that the CSRZ pulses possess a RZ signal shape. The RZ signal shape is slightly wider than the converted CSRZ. The BER measurement shows an error rate of 10^{-10} before and after conversion. As the input power is changed the BER started to change. Fig. 4.9 shows the BER measurement with different input powers from the experiment and simulation. The optimum input power for both formats is -15.5 dBm. This is measured at a BER equal to

10^{-10}. The conversion is observed for other input powers but the BER is higher than 10^{-9}. The optimum input power range for this converter is approximately -15.5 ± 1.0 dBm. The same trend is observed in the simulated result but the optimum input power is -18.0 dBm. The 2.5 dB difference between the experimental and simulated optimum values of receiver power is due to sources of noise and loss not included in the simulation.

The receiver sensitivities at the output of the SOA-NOLM are measured at 1555.2 nm. It is found that in the case of NRZ-to-CSRZ, the received power (-18.2 dBm) required for the converted CSRZ at BER = 10^{-9} is less than that for the unconverted NRZ by 0.5 dB. Whereas, the same received power required for the converted and unconverted signal at BER = 10^{-9} is observed in RZ-to-CSRZ. Thus, for the back-to-back measurement the power penalty of RZ to CSRZ is 0 dB, while for NRZ to CSRZ is -0.5 dB. The negative power penalty means that we see an increase in receiver sensitivity, which is due to the change of data modulation. This could also be due to the change in the initial pulse format i.e. the CSRZ we derive from RZ is different to the CSRZ we derive from NRZ. Although both derived signals are CSRZ they are not necessarily identical to each other. The two converted CSRZ data streams will have different pulse widths and phase profile reflecting the properties of the original source they are derived from. This can be clearly seen from simulated results as shown in Fig. 4.10 and Fig. 4.11. The full wave at half-maximum (FWHM) for the RZ to CSRZ case is about 40 ps while for the NRZ to CSRZ is 60 ps. Fig. 4.12 and Fig. 4.13 depict both conversions at reflection port. The signals at this port are the same as the original input signals before the conversion takes place.

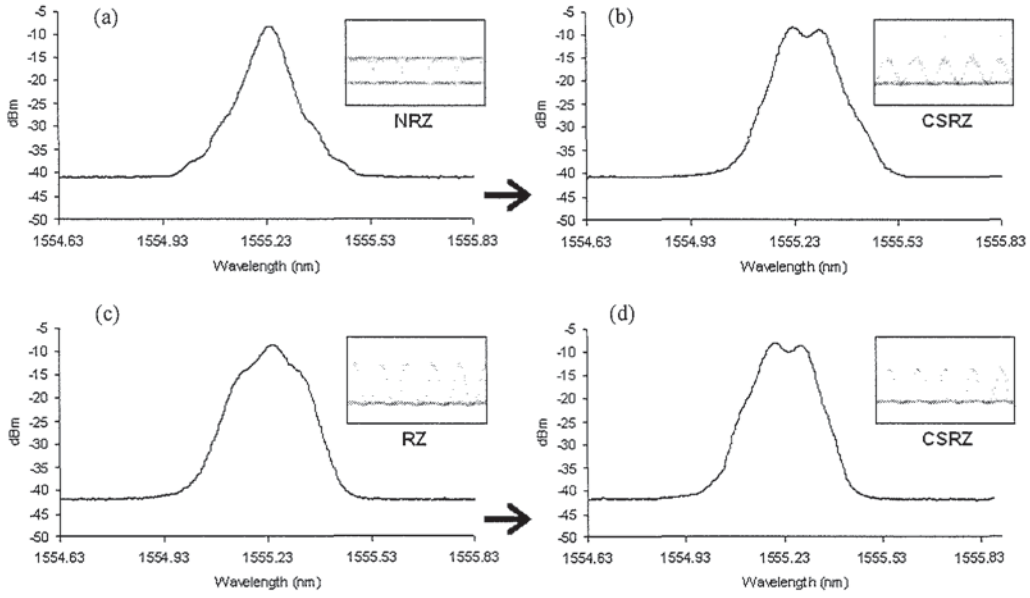

Fig. 4.8. Experimental spectrum and corresponding eye diagram (inset) for (a) NRZ, (b) CSRZ converted from NRZ, (c) RZ, and (d) CSRZ converted from RZ.

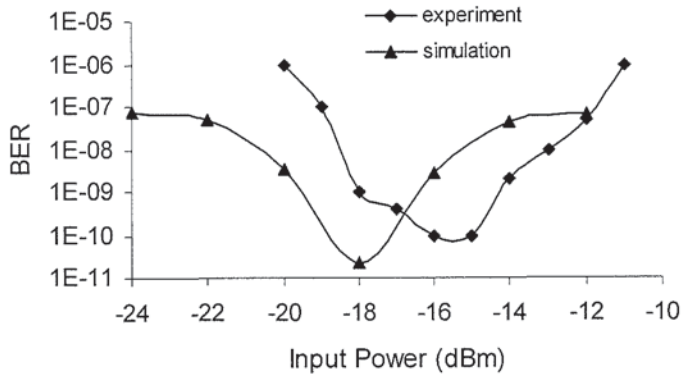

Fig. 4.9. BER versus input power into the converter.

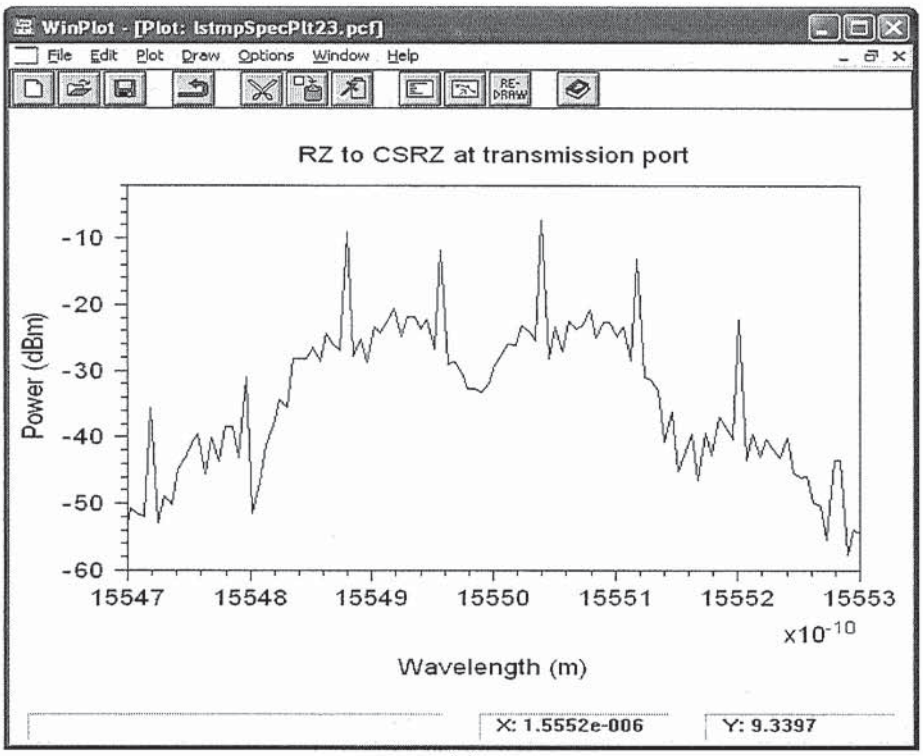

(a)

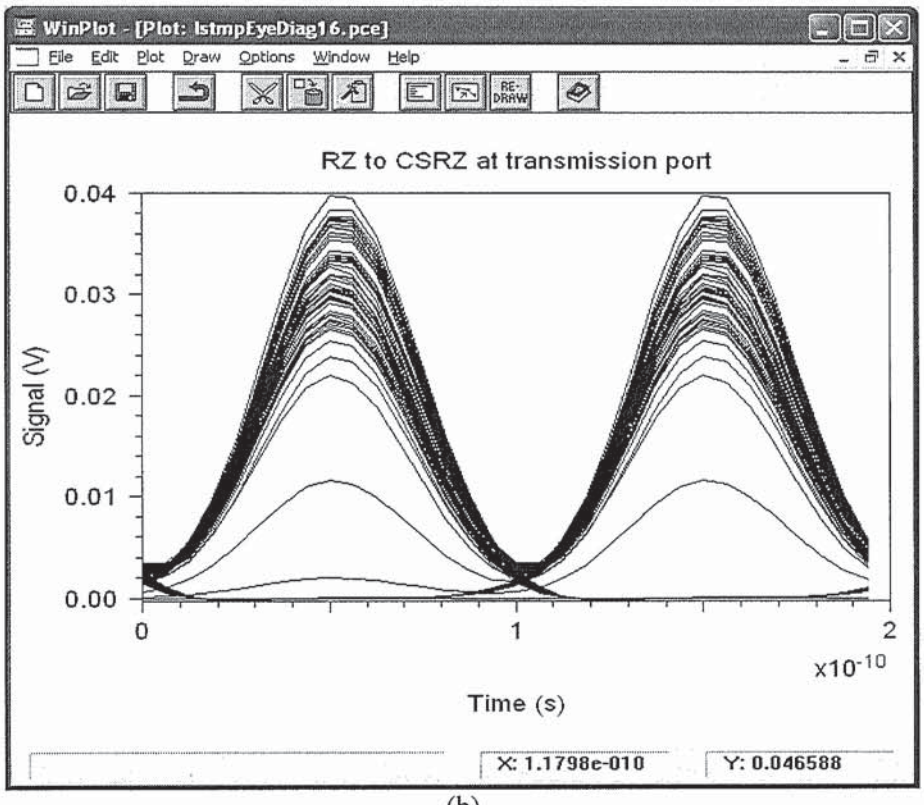

(b)

Fig. 4.10. Simulated (a) spectrum and (b) corresponding eye diagram for CSRZ converted from RZ.

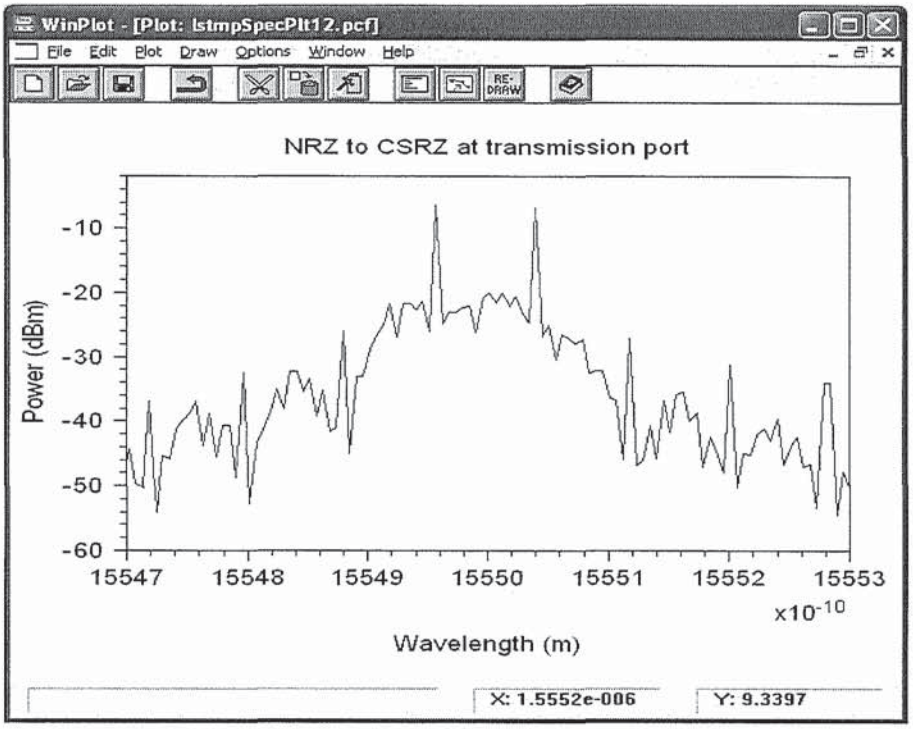

(a)

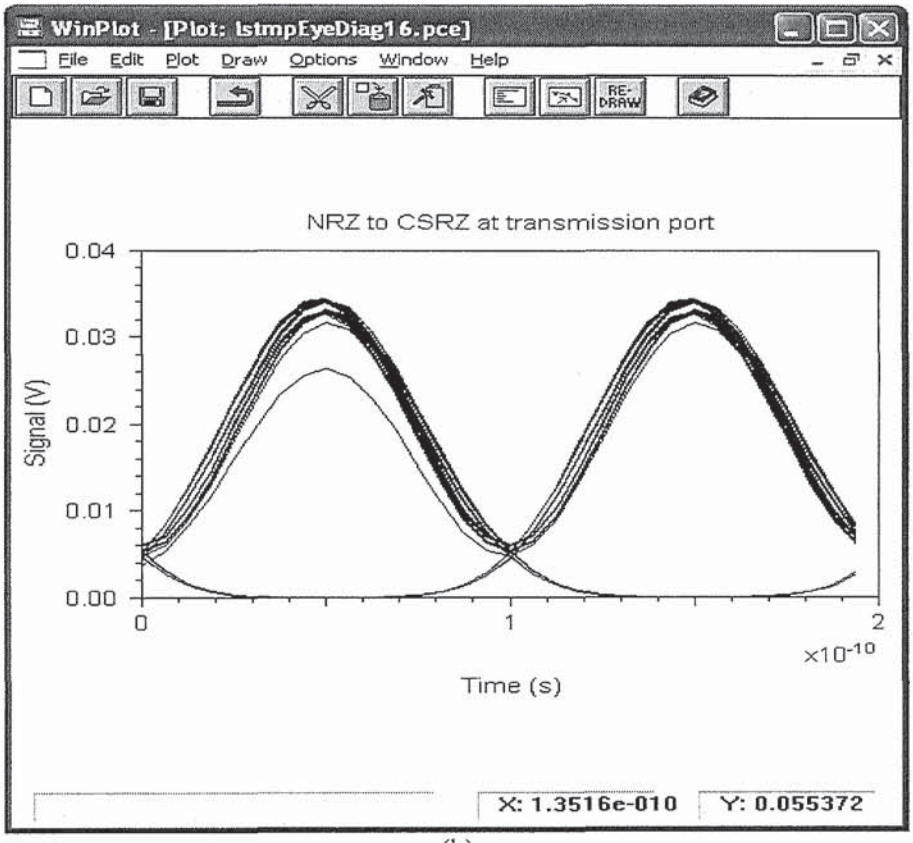

(b)

Fig. 4.11. Simulated (a) spectrum and (b) corresponding eye diagram for CSRZ converted from NRZ.

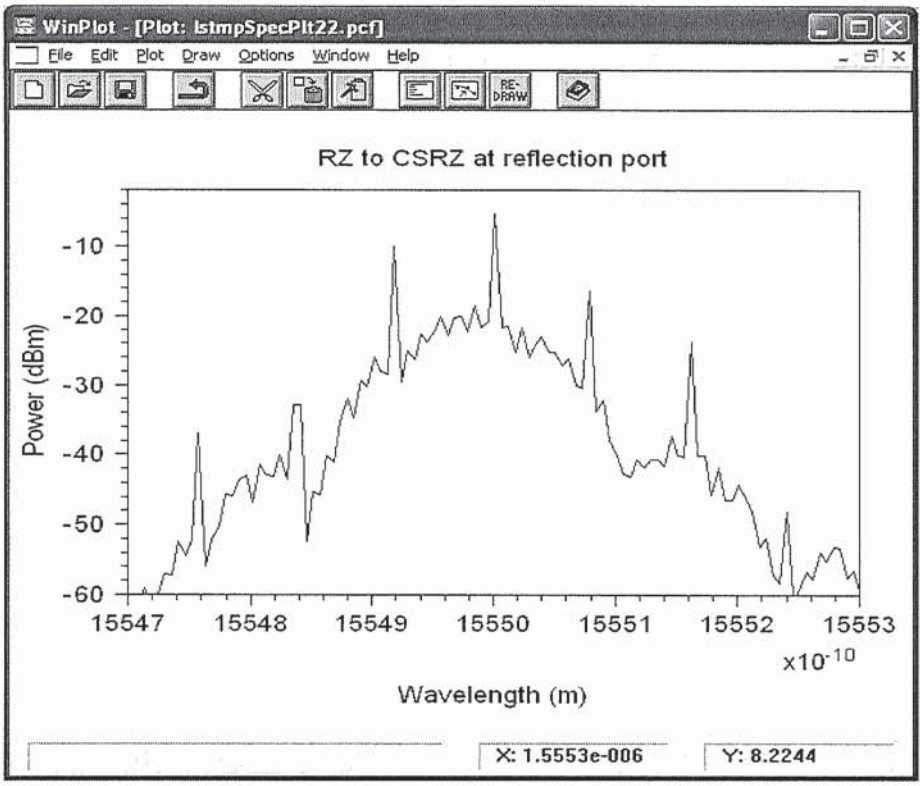

(a)

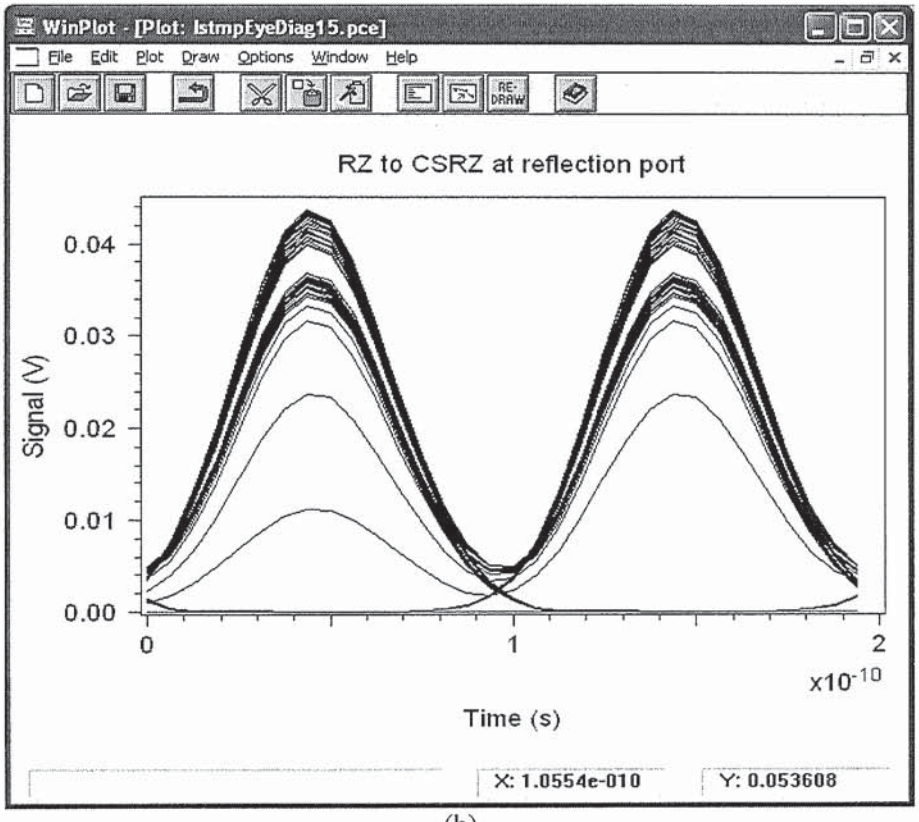

(b)

Fig. 4.12. Simulated RZ (a) spectrum and (b) corresponding eye diagram at reflection port.

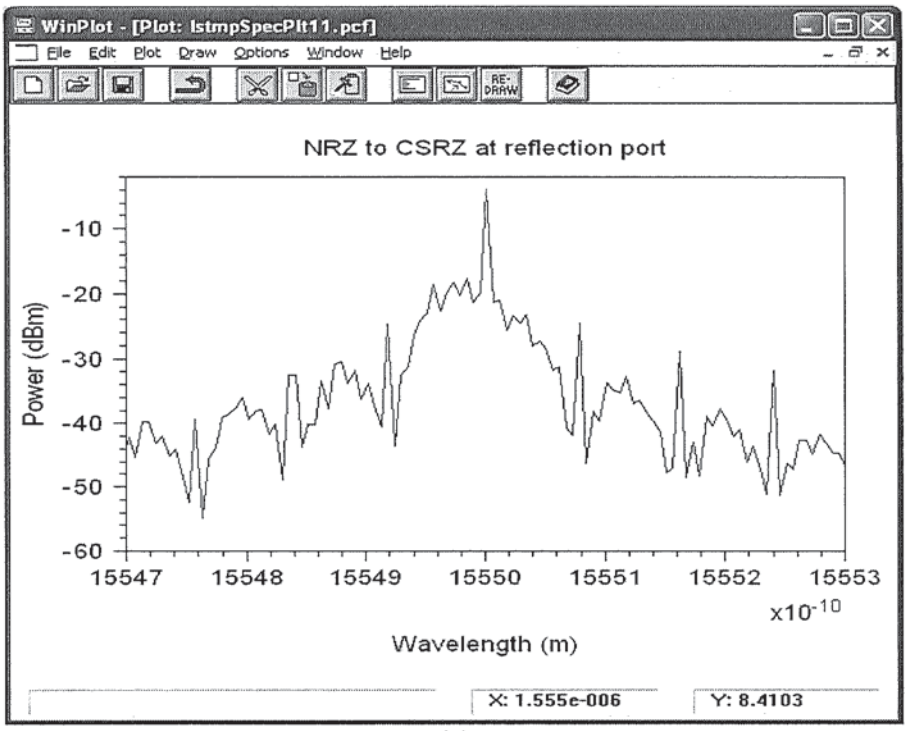

(a)

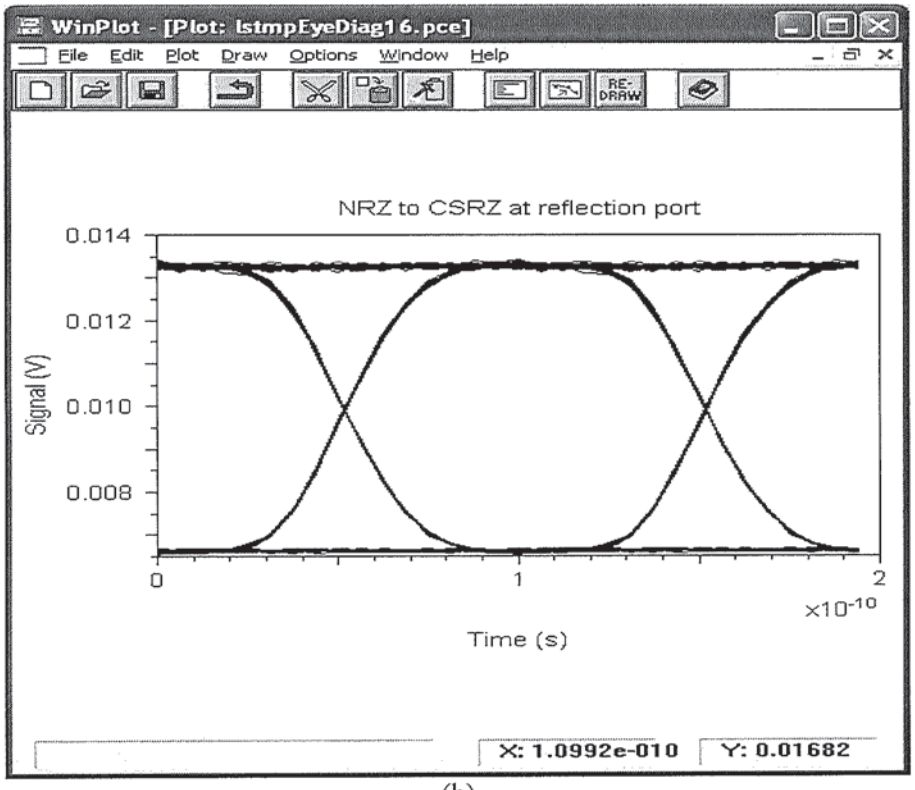

(b)

Fig. 4.13. Simulated NRZ (a) spectrum and (b) corresponding eye diagram at reflection port.

4.4.2 WDM system

In this experiment, the four channels are separated evenly in wavelength and we study the performance for different values of the separation. Fig. 4.14 shows the RZ-to-CSRZ and NRZ-to-CSRZ conversions for the WDM system with 0.8 nm spectral spacing between data signals.

Eye diagrams for each data format are similar for all channels which are given in Fig. 4.14. There are three different wavelength separations between the data that have been used for conversion of both formats i.e. 0.8 nm, 1.6 nm, and 3.2 nm. Fig. 4.15 depicts the CSRZ conversion and its original data for RZ-to-CSRZ, and NRZ-to-CSRZ with 3.2 nm data spacing. The results for the converted CSRZ for each spacing are shown in Fig. 4.16. The same results are observed for NRZ-to-CSRZ conversion. This spacing has also been increased to establish the maximum where the converted CSRZ signals are still observed. It is found that the maximum spacing for these four signals that permits the conversion is 12.0 nm. Although, an equal spacing has been used in all experiments, it does not mean that the spectral separations must be kept the same at all time. It can be seen that all the signals are converted to CSRZ. The maximum and minimum wavelengths that allowed the conversion using this device are plotted in Fig. 4.17. The lowest wavelength that allowed the conversion is 1528 nm, and the highest is 1564 nm. The same values are observed for both conversions. However, the BER is higher than 10^{-8} at these two limits. The best range with a BER equal to 10^{-10} is 1531.4 nm to 1562.2 nm, which is a total bandwidth of 28.8 nm as depicted in Fig. 4.18. This bandwidth is limited by the active region of the SOA as well as the wavelength of the control pulse used to saturate the SOA in the loop. Even with the additional 19.8 dB isolation provided by the fibre Bragg grating, a control pulse peak 2 dB above the noise floor at 1542.3 nm can be clearly seen. Such partial suppression

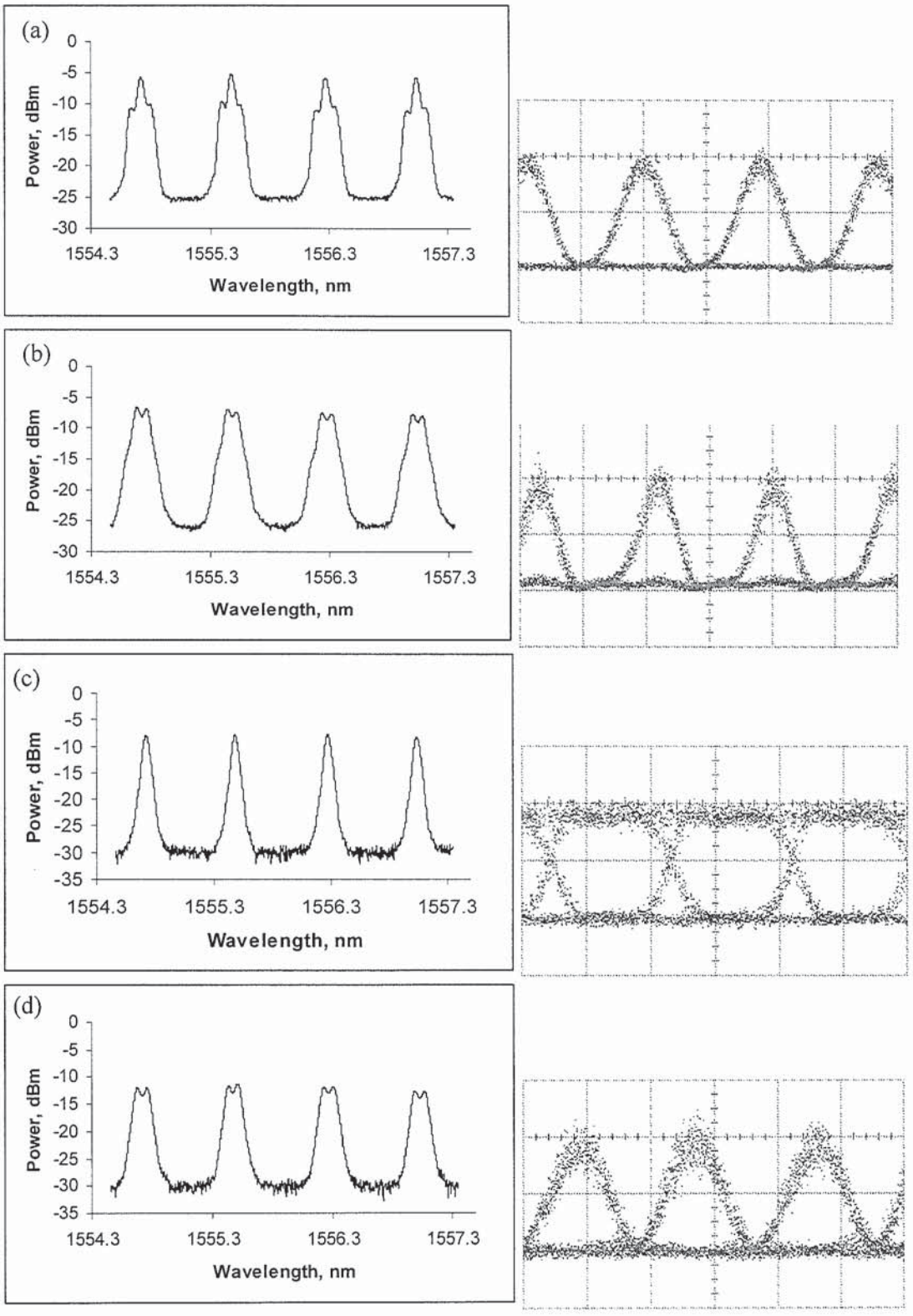

Fig. 4.14. Experimental spectra and corresponding eye diagrams for WDM signals of the formats: (a)RZ, (b)CSRZ converted from RZ, (c)NRZ and (d)CSRZ converted from NRZ.

of the switching signal reduces the conversion region by approximately 1 nm either side of the control signal as shown in Fig. 4.19. If the control pulse can be further suppressed, more channels can be added. It is estimated that 36 channels of 10 GHz signal can be multiplexed and converted by this device. It seems that the bandwidth of the SOA is a major limitation in defining the number of channels. The reflected signal is always the same format as the input signal in all the experiments.

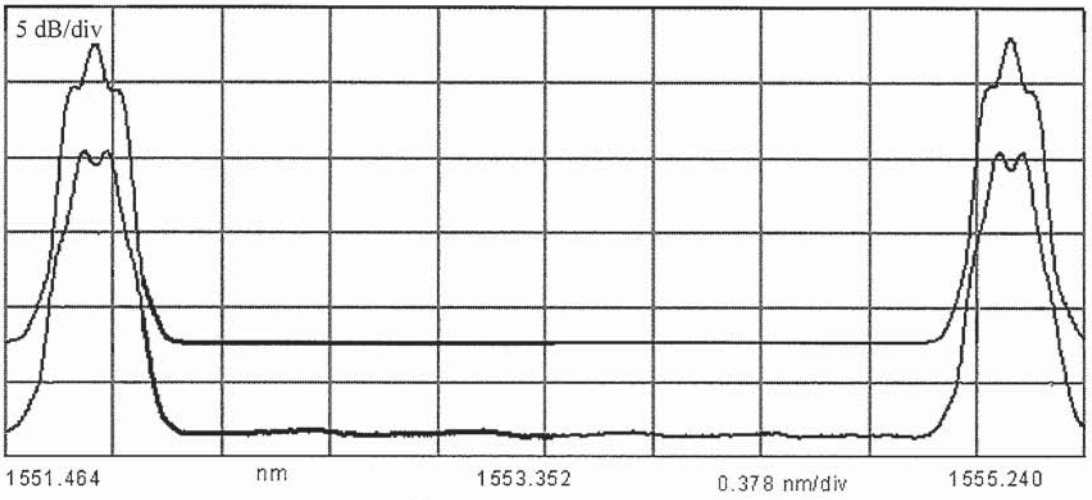

(a)

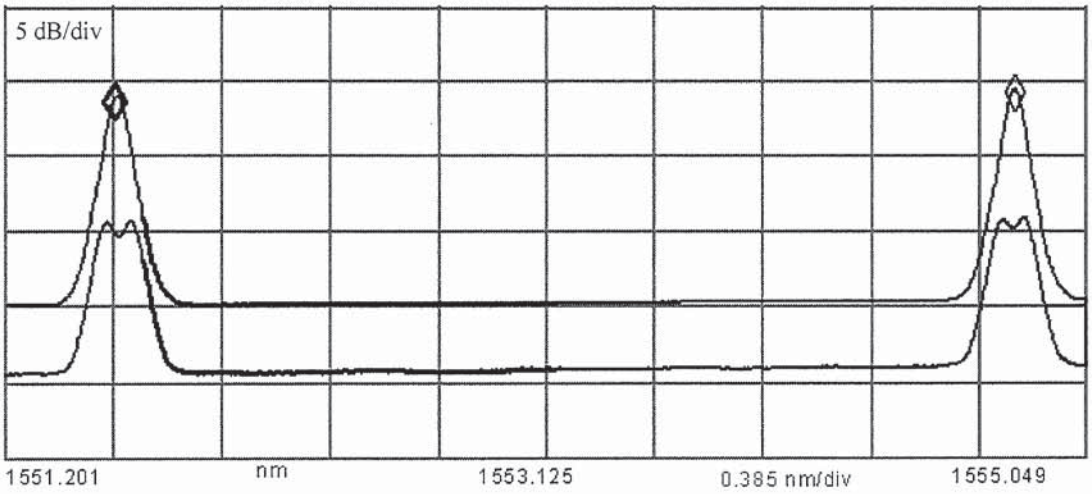

(b)

Fig. 4.15. Experimental spectra of (a) RZ-to-CSRZ and (b) NRZ-to-CSRZ for 3.2 nm spacing between signals.

(a)

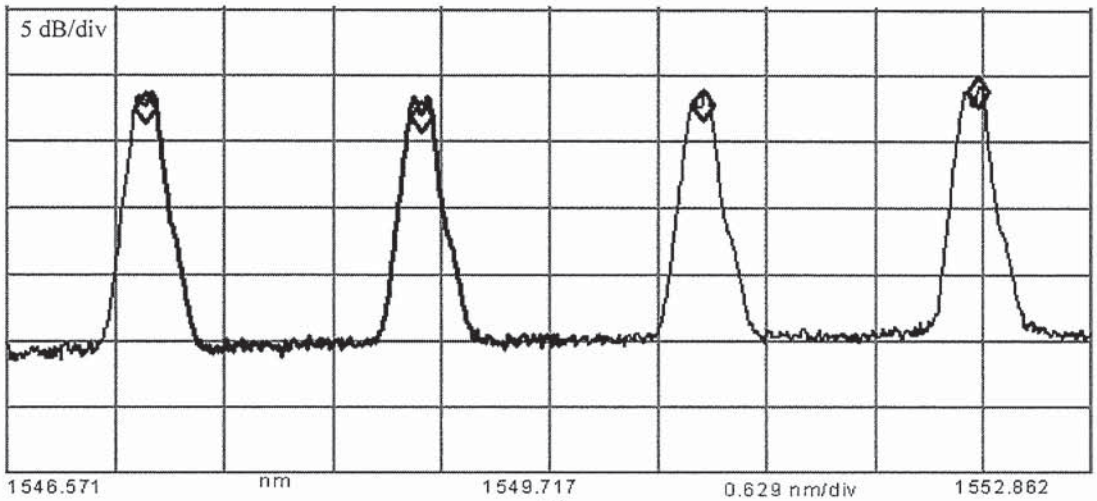

(b)

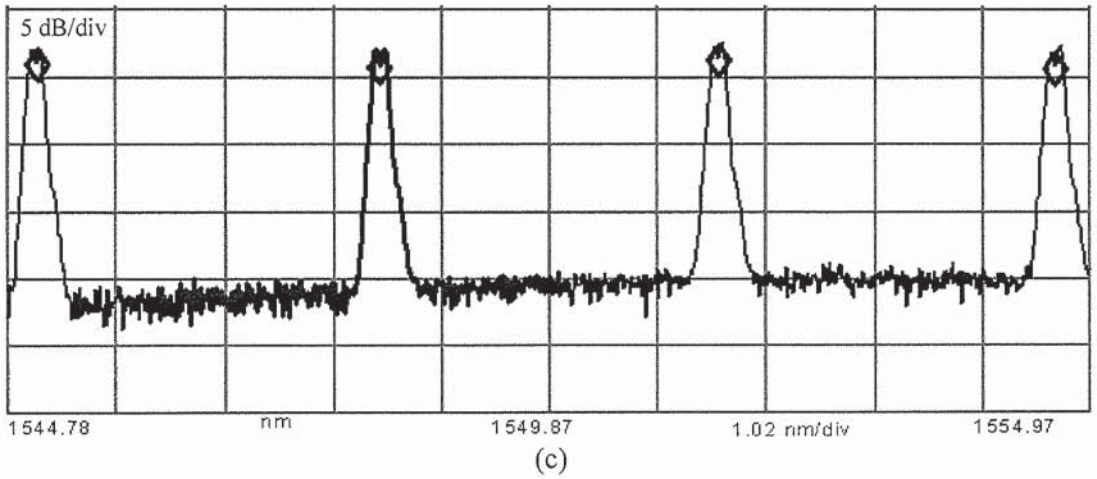

(c)

Fig. 4.16. Experimental spectra for CSRZ at different spectral separations between signals. (a) 0.8 nm, (b) 1.6 nm and (c) 3.2 nm.

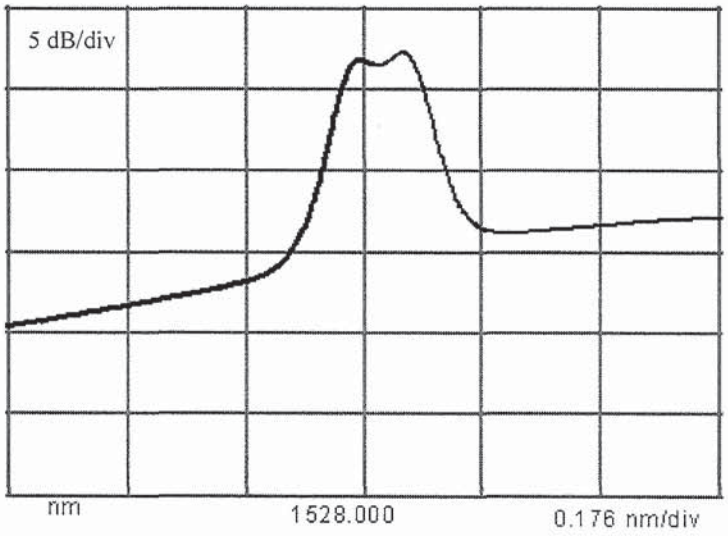

(a)

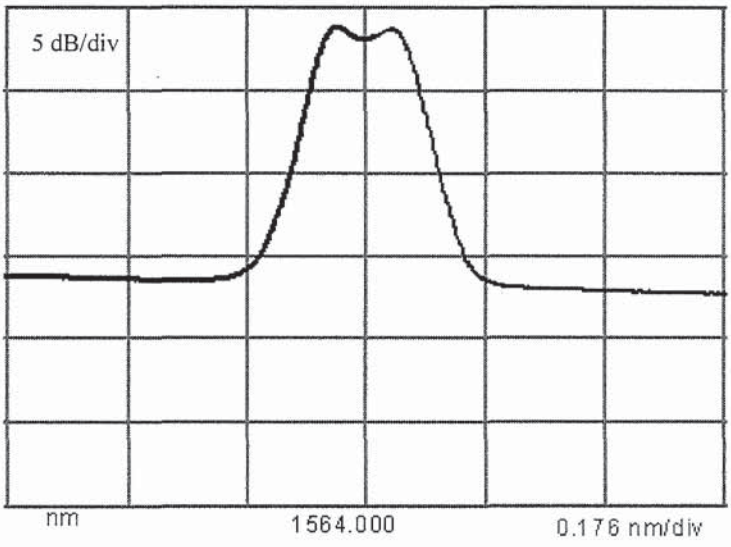

(b)

Fig. 4.17. Experimental spectra for CSRZ conversion at the edge of the available bandwidth. (a) Minimum wavelength and (b) Maximum wavelength.

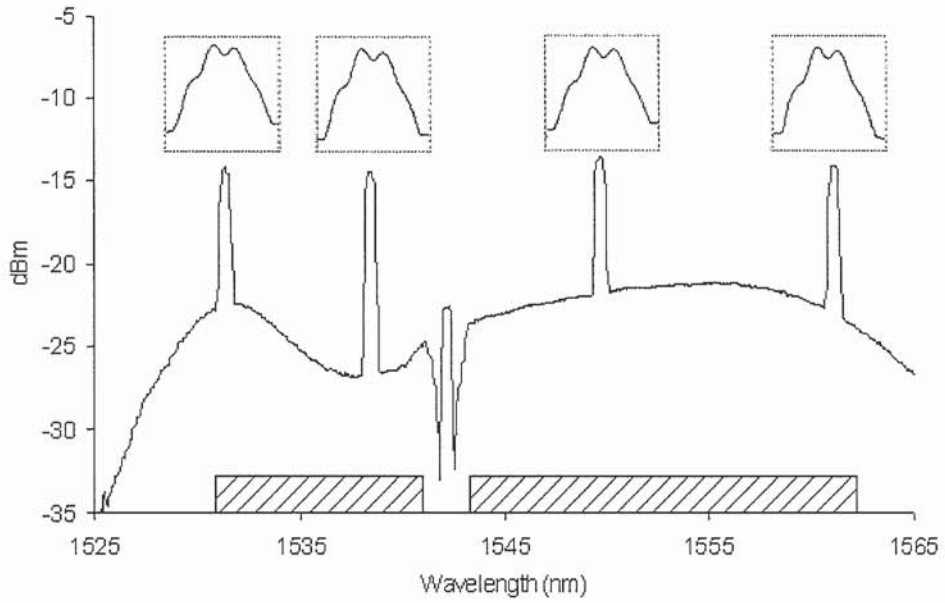

Fig. 4.18. Bandwidth limitation in the CSRZ conversion for a WDM system.

The simulation results have shown a good agreement with the experiments as given in Figs. 4.20 to 4.26. The CSRZ is observed at the transmission port for all conversions. Fig. 4.27 illustrates a block diagram whereby the converted CSRZ can be changed to RZ by employing the second SOA-NOLM with the same configuration as the first converter. The converted CSRZ is become the input to the second SOA-NOLM converter. Due to the limitation of the equipments this experiment has not been performed in the laboratory. However, the simulation results in Figs. 4.28 and 4.29 shows an agreement with the results reported earlier [62]. The typical input signals used for RZ to CSRZ and NRZ to CSRZ is given in Fig. 4.30.

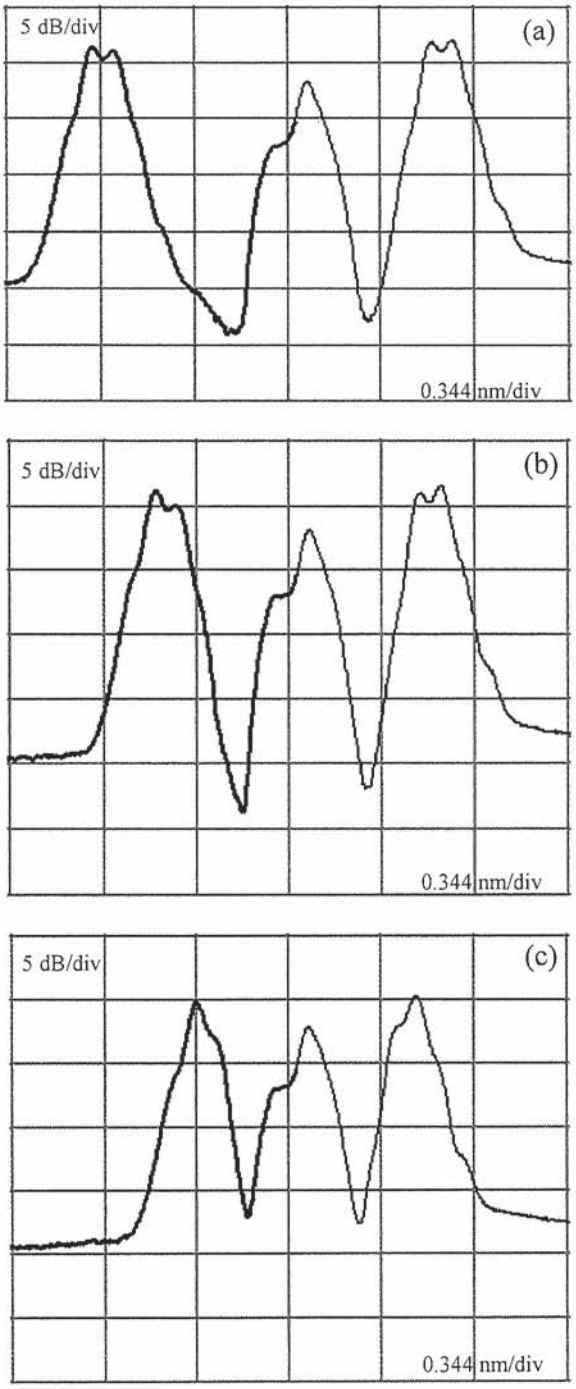

Fig. 4.19. Experimental spectra for evolution of the converted CSRZ as the signal wavelength approaches that of the control pulse at wavelength 1543 nm. (a) CSRZ is fully observed, (b) CSRZ is partly observed and (c) CSRZ is disappeared.

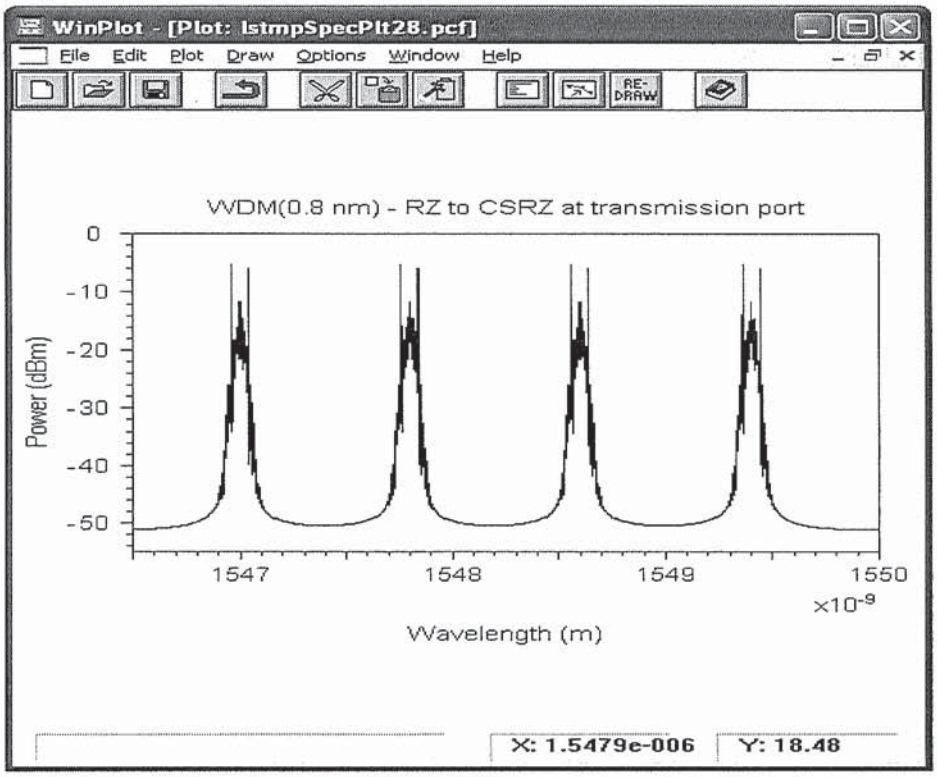

(a)

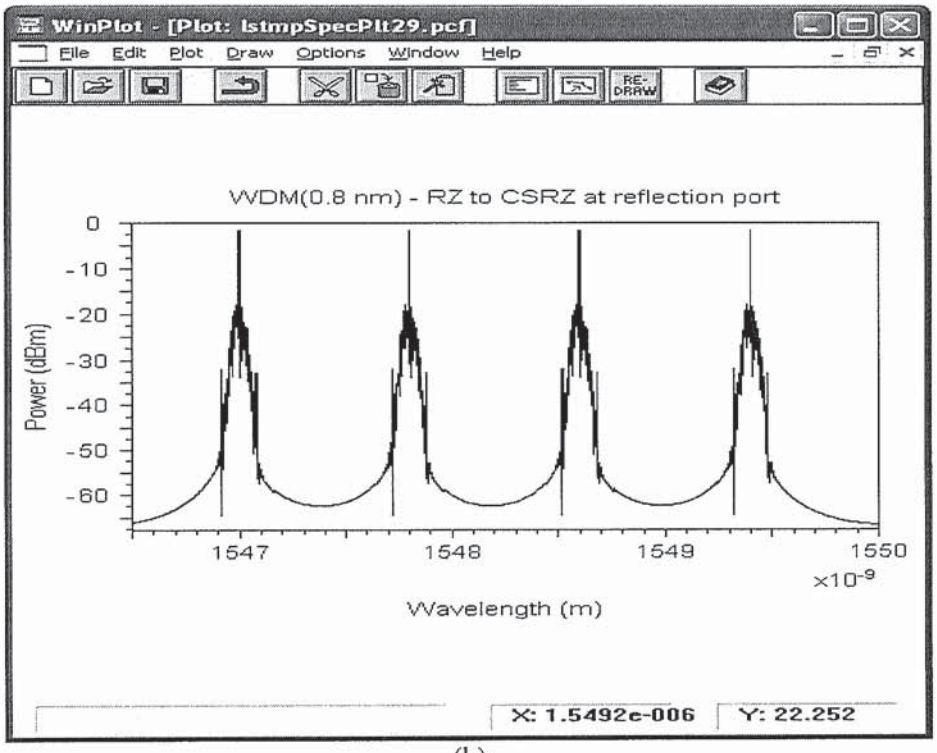

(b)

Fig. 4.20. Simulated spectra of RZ to CSRZ conversion for 0.8 nm spacing between signals at (a) transmission port and (b) reflection port.

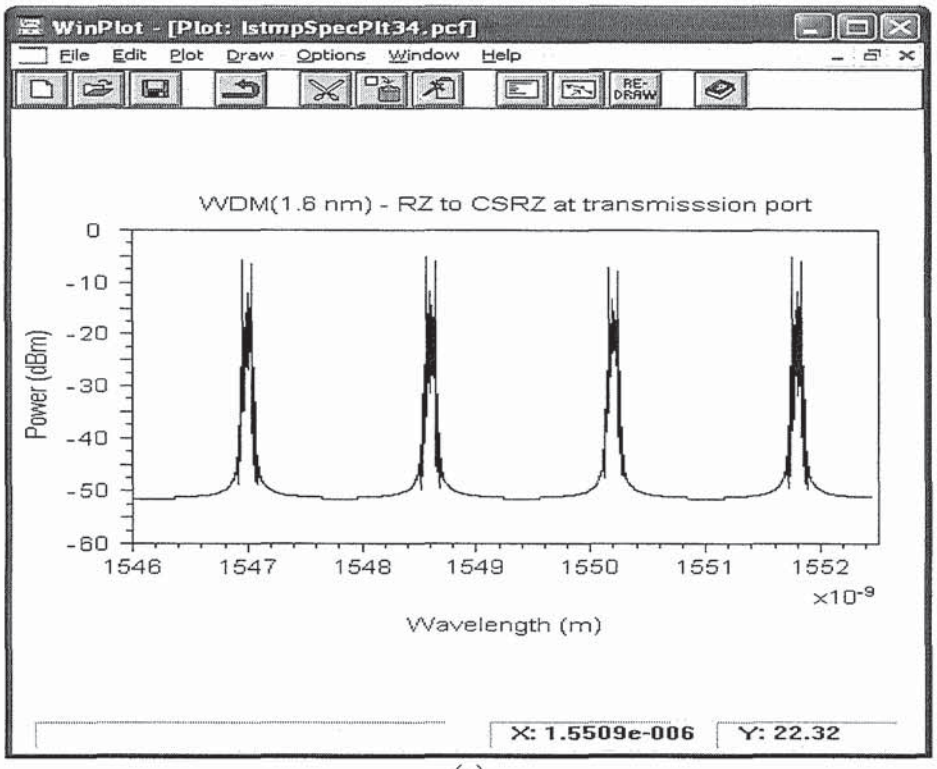

(a)

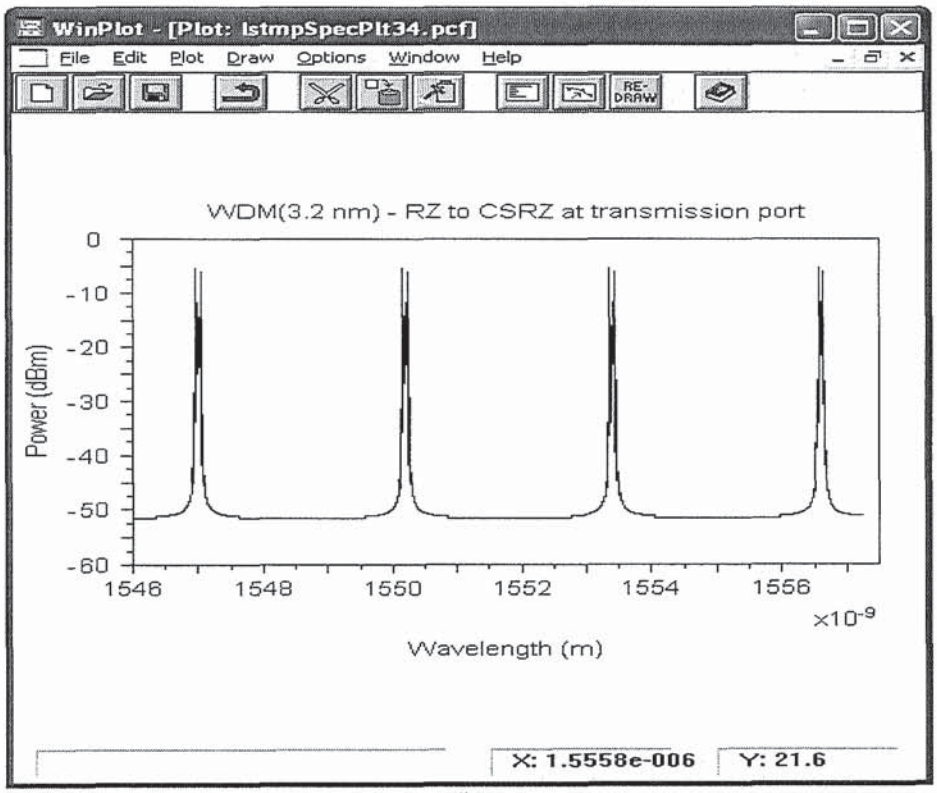

(b)

Fig. 4.21. Simulated spectra of RZ to CSRZ conversion at transmission port for (a) 1.6 nm and (b) 3.2 nm spacing between signals.

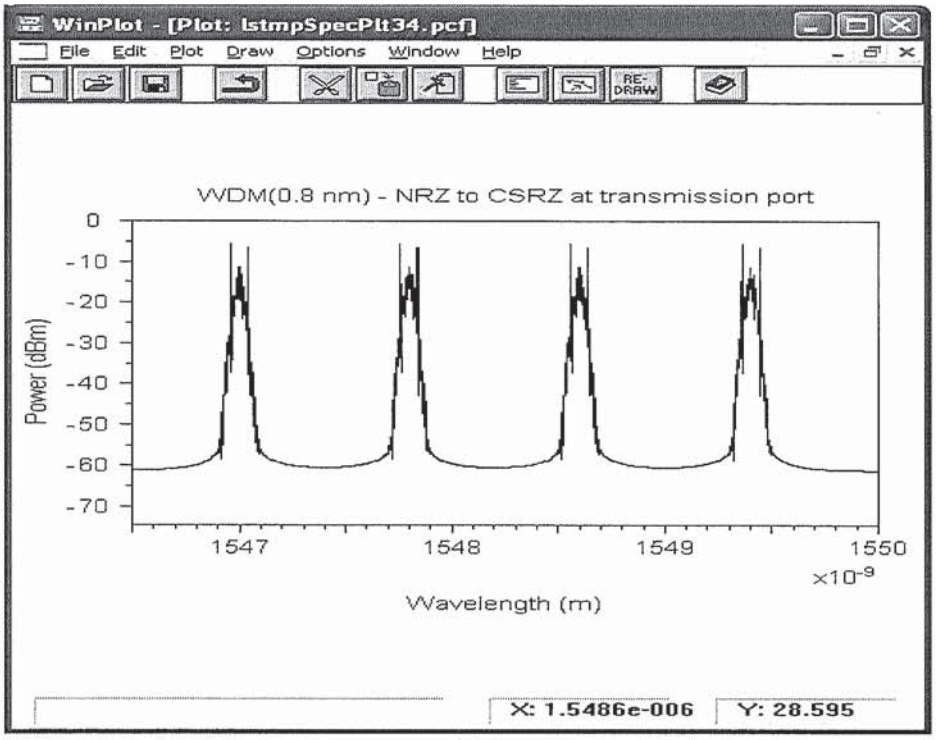

(a)

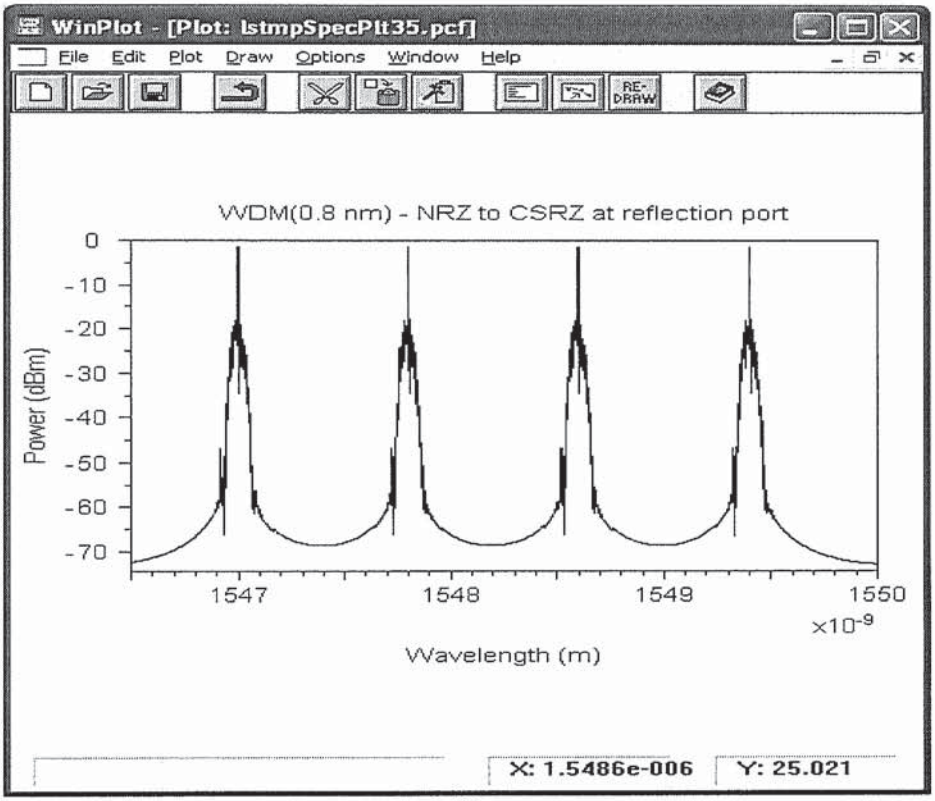

(b)

Fig. 4.22. Simulated spectra of NRZ to CSRZ conversion for 0.8 nm spacing between signals at (a) transmission port and (b) reflection port.

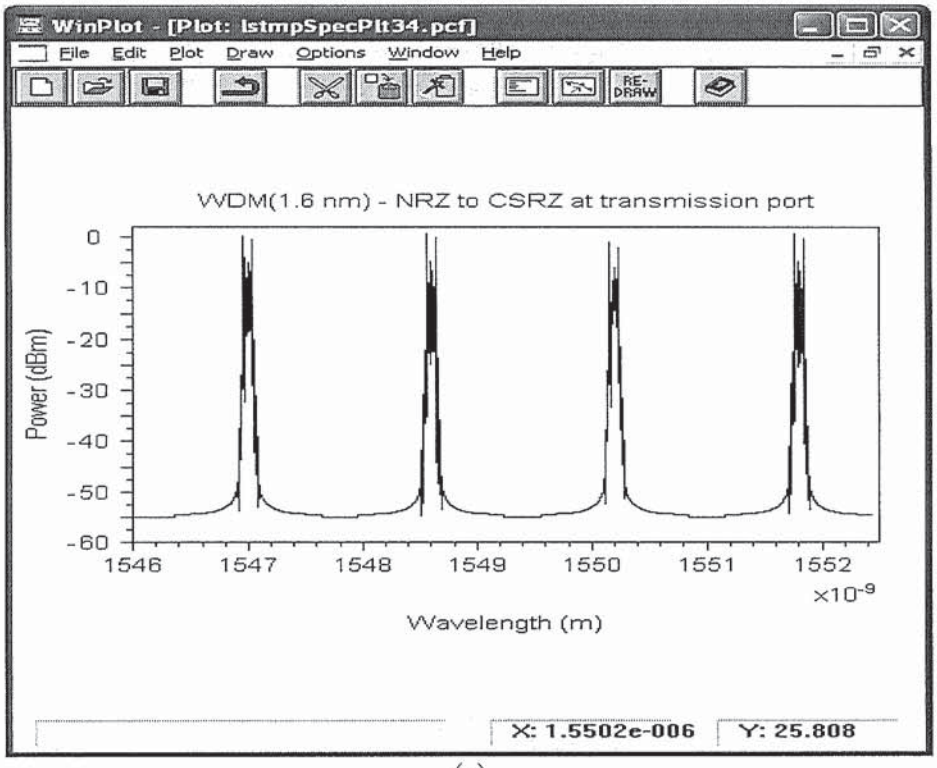

(a)

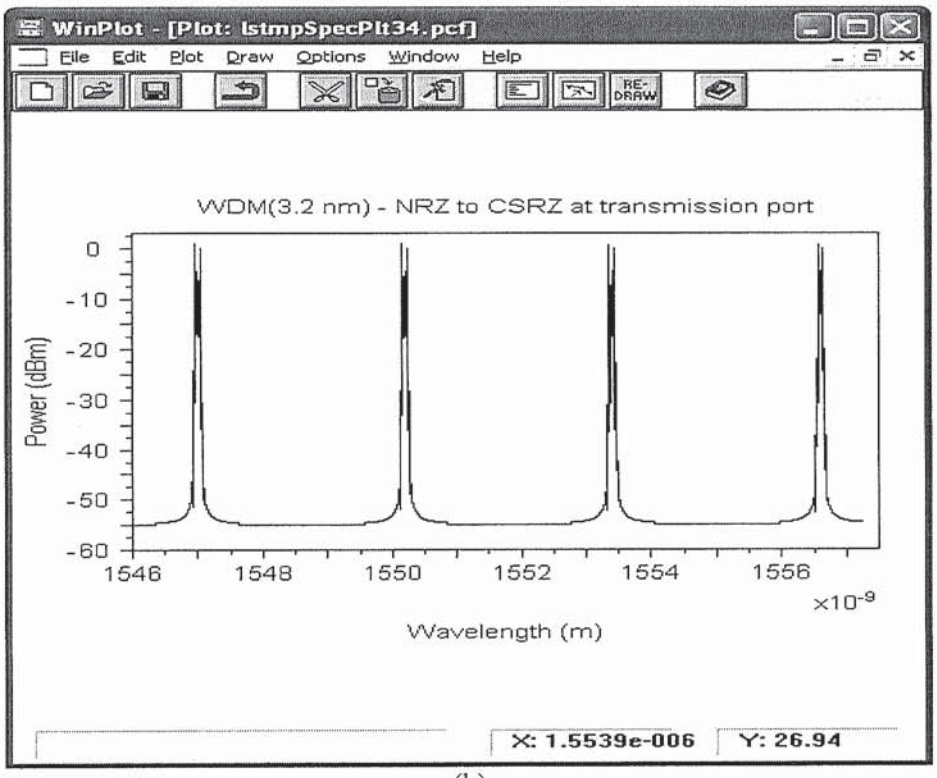

(b)

Fig. 4.23. Simulated spectra of NRZ to CSRZ conversion at transmission port for (a) 1.6 nm and (b) 3.2 nm spacing between signals.

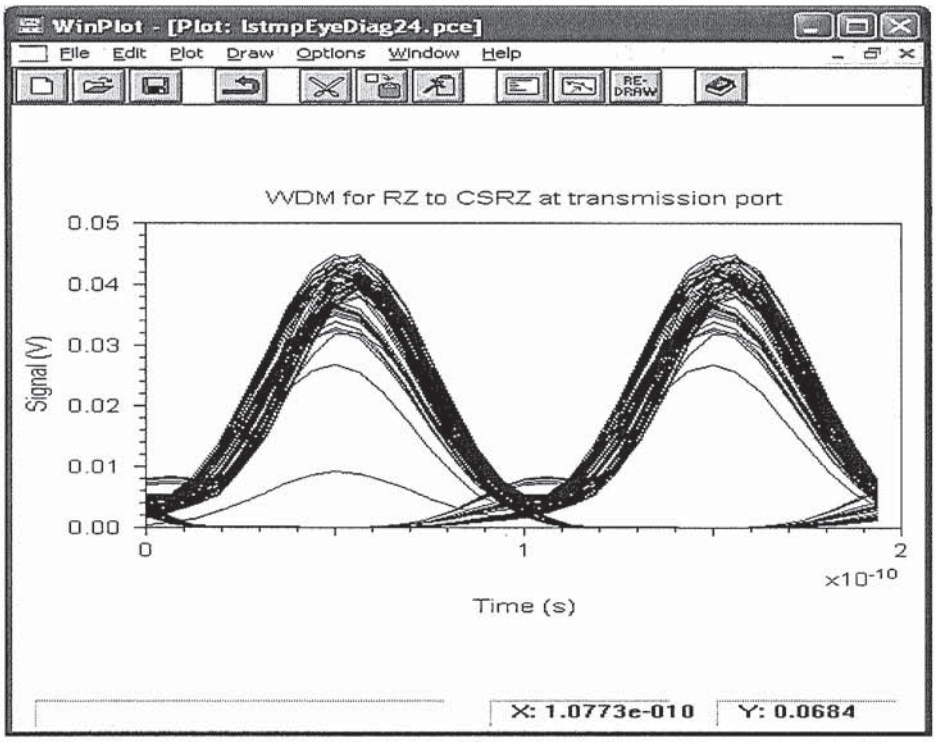

(a)

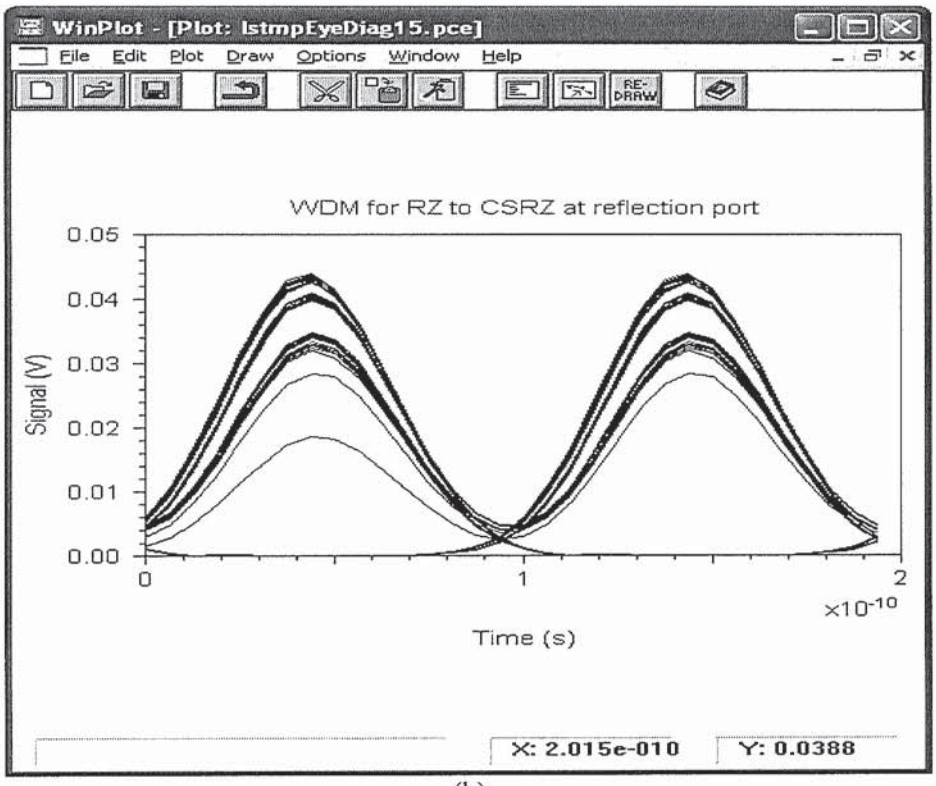

(b)

Fig. 4.24. Simulated eye diagrams of RZ to CSRZ conversion for WDM signals at (a) transmission port and (b) reflection port.

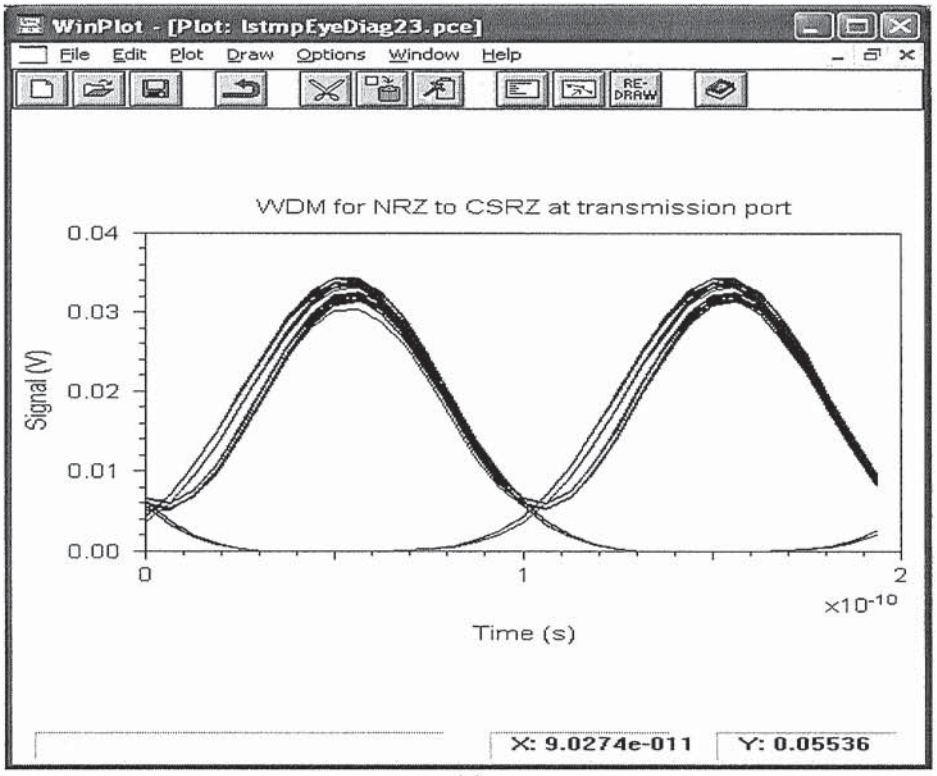

(a)

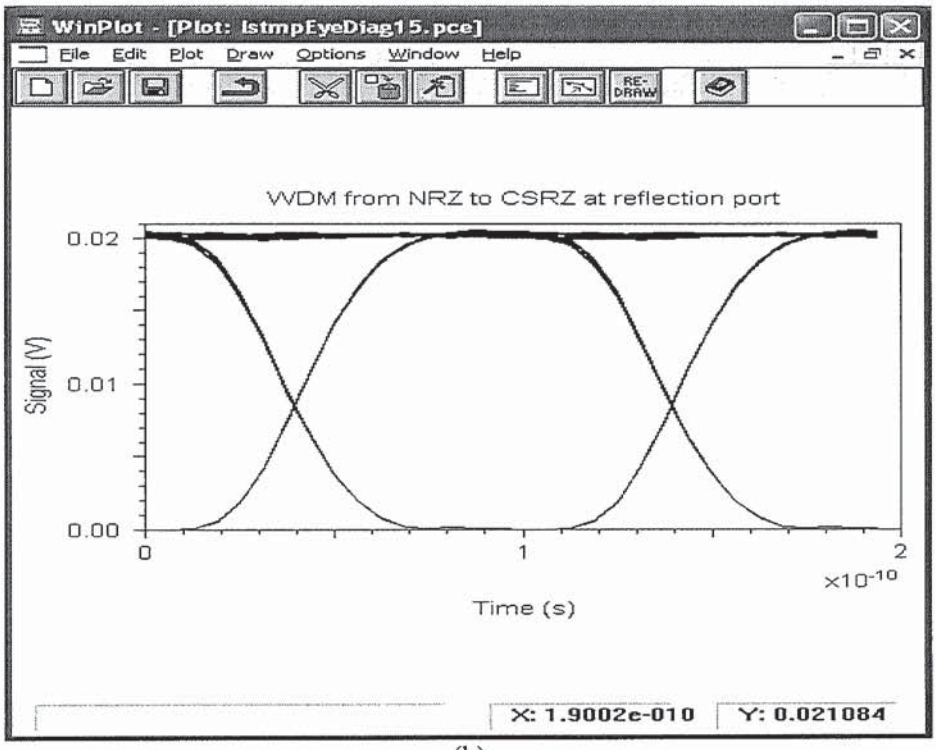

(b)

Fig. 4.25. Simulated eye diagrams of NRZ to CSRZ conversion for WDM signals at (a) transmission port and (b) reflection port.

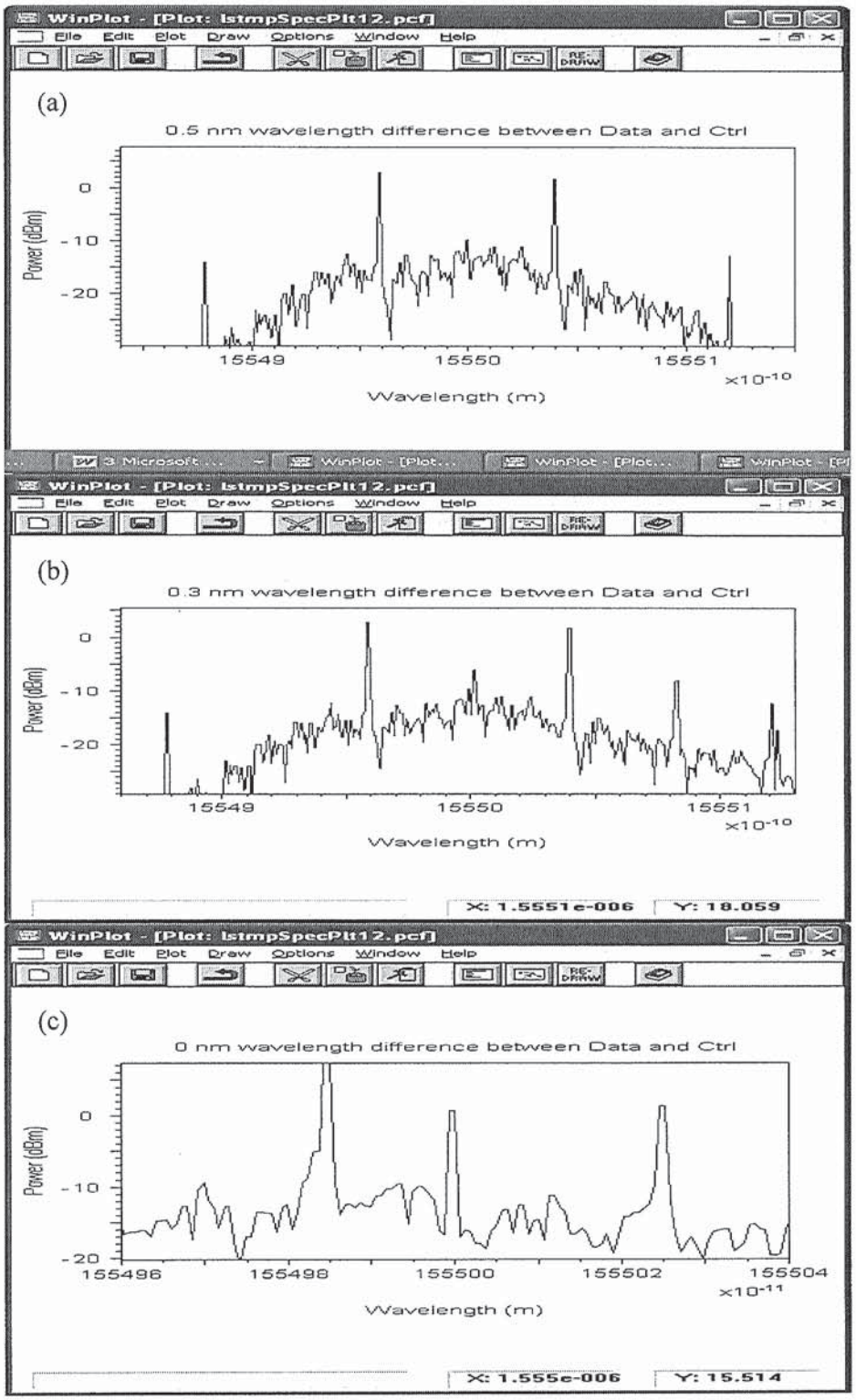

Fig. 4.26. Simulated spectra for evolution of the converted CSRZ as the signal wavelength approaches that of the control pulse. (a) CSRZ is fully observed, (b) CSRZ is partly observed and (c) CSRZ is disappeared.

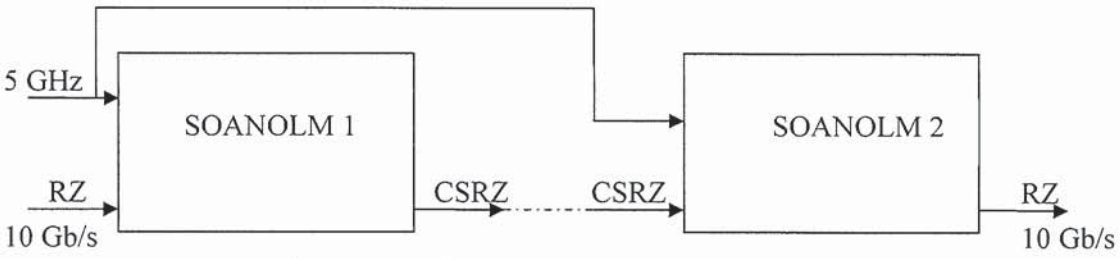

Fig. 4.27. A block diagram for converted CSRZ to RZ.

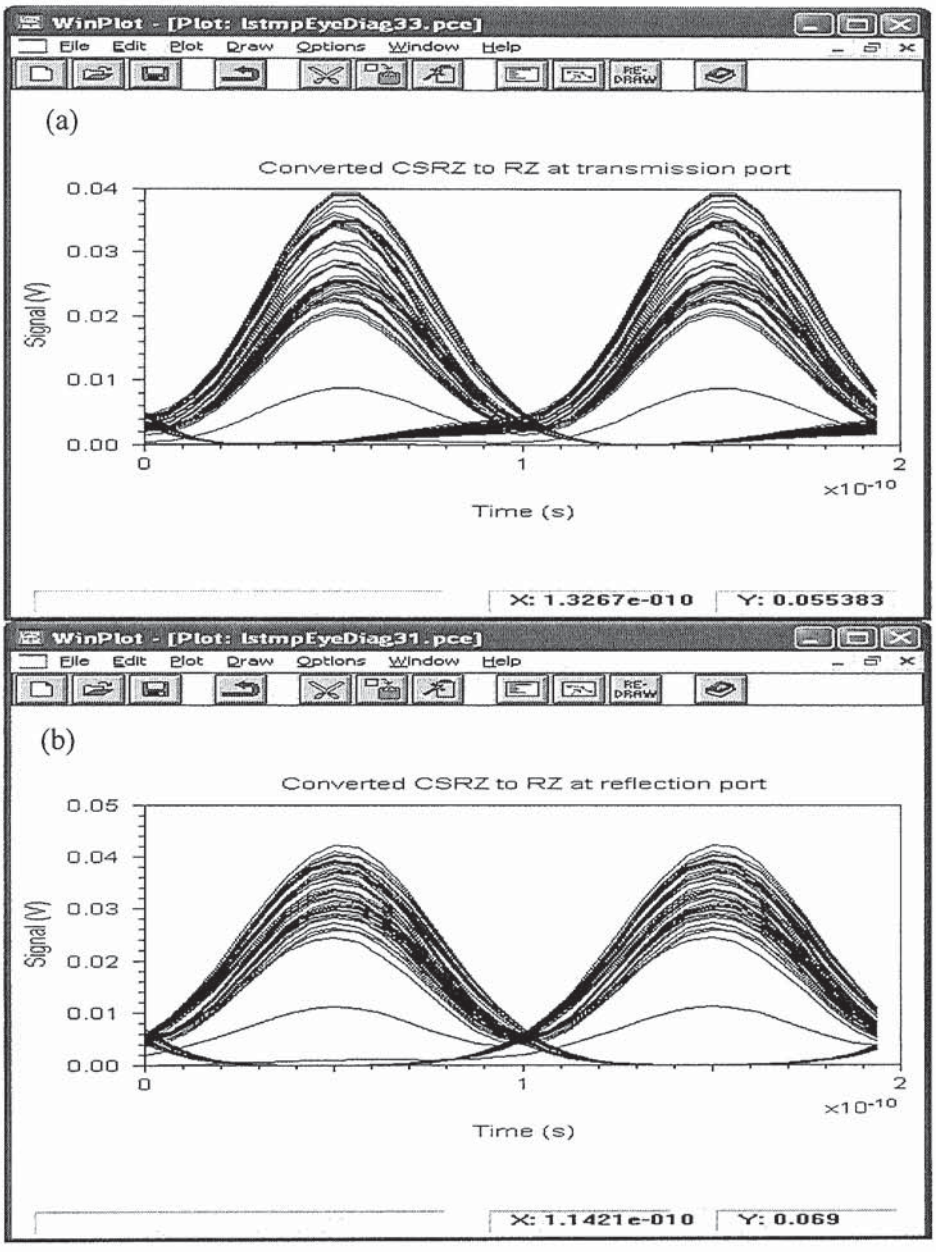

Fig. 4.28. Simulated eye diagrams for CSRZ to RZ conversion at (a) transmission port and (b) reflection port.

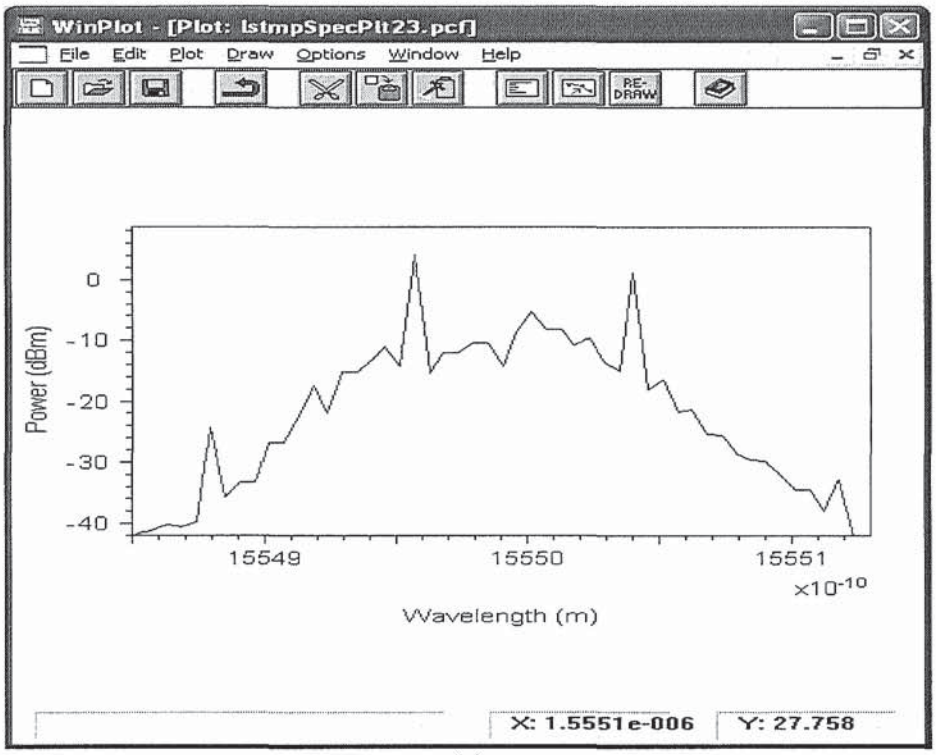

(a)

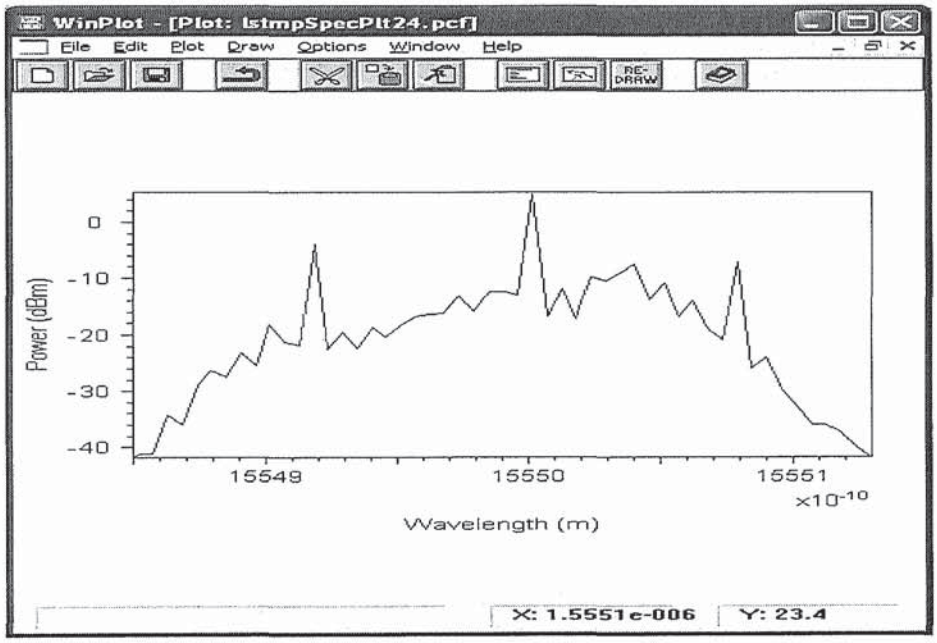

(b)

Fig. 4.29. Simulated spectra for CSRZ to RZ conversion at (a) transmission port and (b) reflection port.

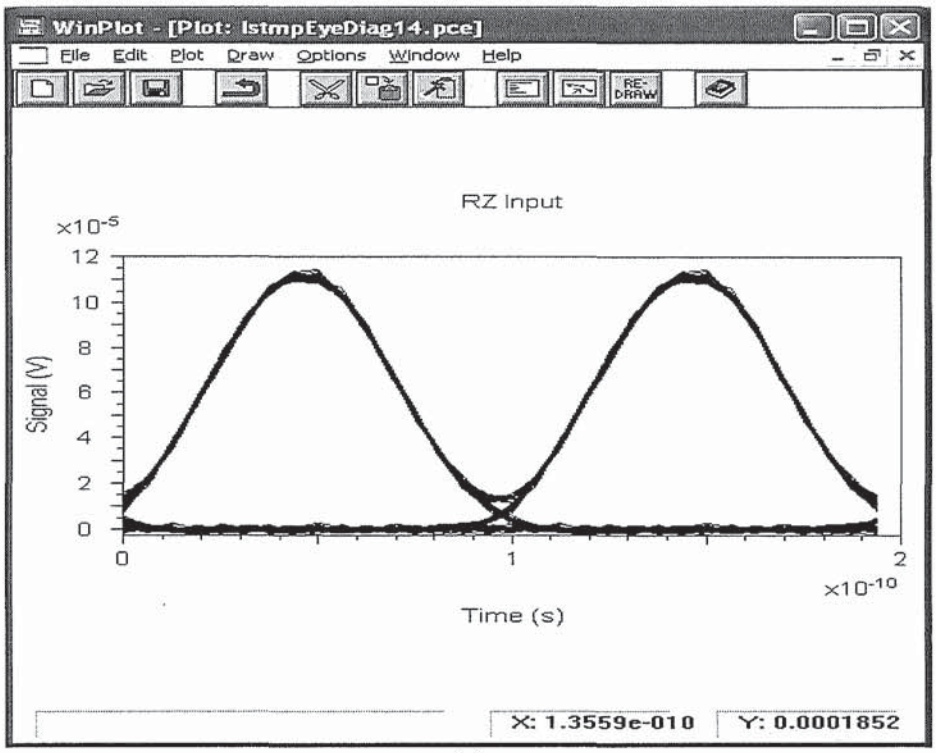

(a)

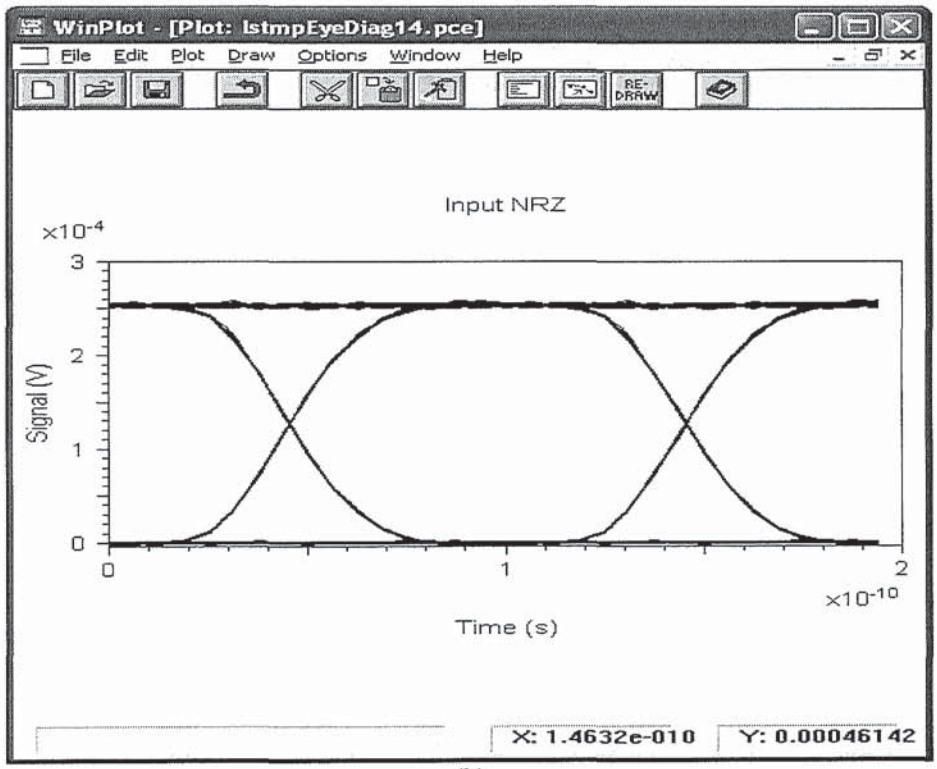

(b)

Fig. 4.30. Simulated input signals used in all conversions for (a) RZ and (b) NRZ.

4.5 CSRZ transmission: experiment and results

Fig. 4.31 shows the setup for CSRZ transmission experiment. This is actually a link from the converter in the previous section 4.4 with a 194 km recirculating transmission loop. The loop consists of two nearly symmetric dispersion managed fibre sections of approximately 40.5 km of SMF, 16 km of DCF and 40.5 km SMF. The SMFs have an attenuation coefficient of 0.2 dB/km and dispersion of 17 ps/nm/km at 1550 nm, while the DCF units each have a negative dispersion of about 1385 ps/nm and an insertion loss of 7.9 dB. The losses are compensated using two Erbium-doped fibre amplifier (EDFA) repeaters within each section. The EDFAs denoted A, in Fig. 4.31, have a 30 dB maximum small signal gain, while the EDFAs denoted B have a 40 dB maximum small signal gain. An ASE filter with an insertion loss of 3 dB is used before the pre-receiver amplifier to remove the ASE gain peak at 1530 nm. A tuneable grating filter, with a 0.24 nm 3 dB bandwidth, is used prior to the bit error rate analyser and the clock recovery unit in order to isolate an individual channel for error detection. The input power into the fibre span is 6.4 dBm, which is sufficiently high to allow nonlinear operation. This will be useful in comparing the tolerance of the converted and unconverted signals towards nonlinear effects. In fact, the SOA-NOLM deteriorates the quality of the converted signal before transmission. This is due to the ASE and other noise introduced by the SOA in addition to some other undesired nonlinear effects, i.e. cross-gain modulation and four-wave mixing, existing in the SOA. Therefore, for consistency, the comparisons are performed with the signal passing through the loop mirror before being transmitted over the fibre span. Thus, all signals have the same environmental condition where any impairment introduced by the loop mirror is common to all measurements. Furthermore, the optical signal to noise ratio (OSNR) and the extinction ratio are almost equalised before the transmission begins.

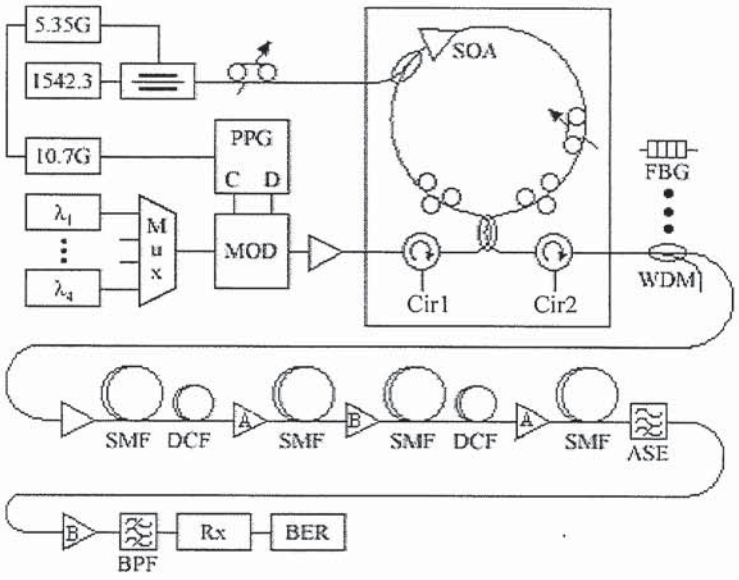

Fig. 4.31. Experimental setup for single channel and WDM transmission.

4.5.1 Single channel

In single channel transmission, only one wavelength is used. Fig. 4.32 depicts the BER versus transmission distance for the RZ and NRZ, and the converted CSRZ signals. It is clearly observed that the converted format i.e. CSRZ performs the longer transmission distance. Table 4.1 shows the maximum distance at 10^{-9} BER floor for all transmitted formats. The simulation result for a single span is shown in Table 4.2. It is agreed with the experimental observation. Note that the predicted variations in the maximum single span length match the experimentally observed maximum system lengths.

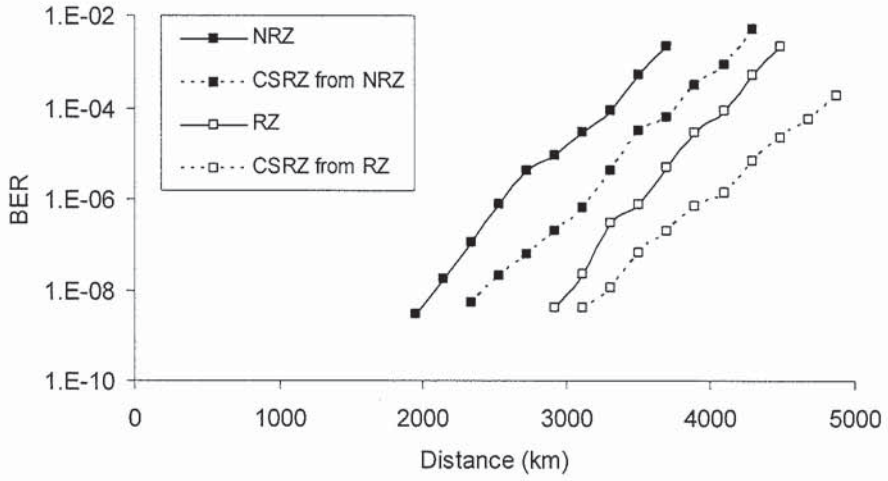

Fig. 4.32. Experimental results of BER versus transmission distance.

Transmission format	Maximum transmission distance, km
RZ	2800
CSRZ-converted-RZ	3000
NRZ	1800
CSRZ-converted-NRZ	2300

Table 4.1. Experimental results for maximum transmission distance of all formats in a recirculating loop.

Transmission format	Maximum transmission distance, km
RZ	272
CSRZ-converted-RZ	305
NRZ	150
CSRZ-converted-NRZ	193

Table 4.2. Simulated results for maximum transmission distance of all formats in a single span.

The CSRZ-converted-NRZ (i.e CSRZ converted from NRZ) improved by 500 km, while the CSRZ-converted-RZ (i.e. CSRZ converted from RZ) increased by 200 km more than its unconverted format. However, the CSRZ-converted-RZ has shown the best performance in terms of transmission distance. This distance can be optimised by slightly adjusting the bias current and tuning the polarisation controllers of the SOA-NOLM while the transmission takes place. The optimisation by using the above method is not suggested if comparison between different signals need to be performed. This is because the OSNR and the extinction ratio will not be the same for all formats. To further confirm that the signals are not chirped in the SOA-NOLM that may cause the improvement, the signals have been passed through SMF with different lengths and the pulse widths have been measured. Fig. 4.33 shows broadening of the signals for RZ and its converted CSRZ. There is an equal broadening for both formats; therefore the chirped does not influence the improvement of the transmission distance. If it does, one of the signals will experience broadening more rapidly than the other.

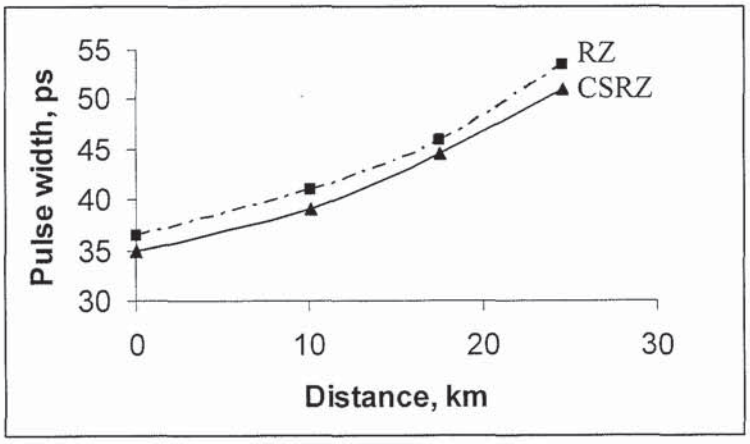

Fig. 4.33. Pulse width versus distance for RZ and its converted CSRZ.

4.5.2 WDM system

Unlike in the single channel case, the WDM system uses only a 194 km in-line fibre span without recirculation loop. Fig. 4.34 shows the BER results after transmission over the 194 km span for the four WDM channels with different formats. As can be seen in Fig. 4.34, CSRZ outperforms the other modulation formats in receiver sensitivities. A received power of -17.9 dBm per channel is required to achieve a BER of $1x10^{-9}$ for the NRZ format, whereas the converted format required a lower power of -18.8 dBm to attain the same error rate. For the RZ case, the received power required at BER equals $1x10^{-9}$ is -22 dBm, while for the converted format is -22.5 dBm. The slope of the BER-power curve for both converted carrier-suppressed formats decays slower than that of their original counterparts. At a BER of $1x10^{-5}$, the improvement in required received power has increased from 0.9 dB to 1.2 dB for NRZ and from 0.5 dB to 0.9 dB for RZ. By taking consideration of the receiver sensitivities which are measured in section 4.4.1, it can be concluded that the transmission improved the sensitivity of the CSRZ format by 0.4 dB in the case of NRZ, and 0.5 dB in the case of RZ format. However, as this system employed 194 km dispersion-managed fibre, using SSMF-DCF configuration, and 100 GHz channel spacing; it did not show large transmission penalties for the formats studied. More considerable penalties would be expected if the transmission configuration is modified to demonstrate significant four-wave mixing (FWM) by using lower local dispersion, e.g. DSF, or higher inter-channel interaction by using lower channel spacing.

The simulated transmission result for one WDM channel is shown in Fig. 4.35. At a BER of $1x10^{-9}$, the improvement in required received power has increased from 1.0 dB for NRZ and 0.6 dB for RZ. The curve also decays slower as observed in the experiment. The same trend of results is observed in the other channels.

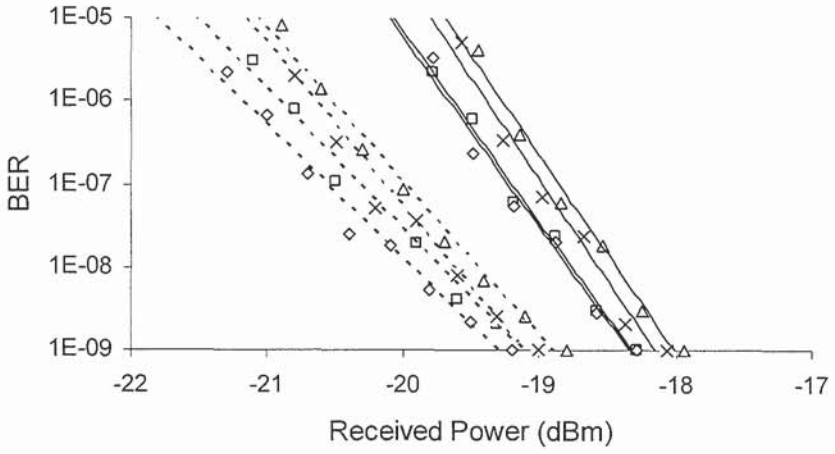

(a)

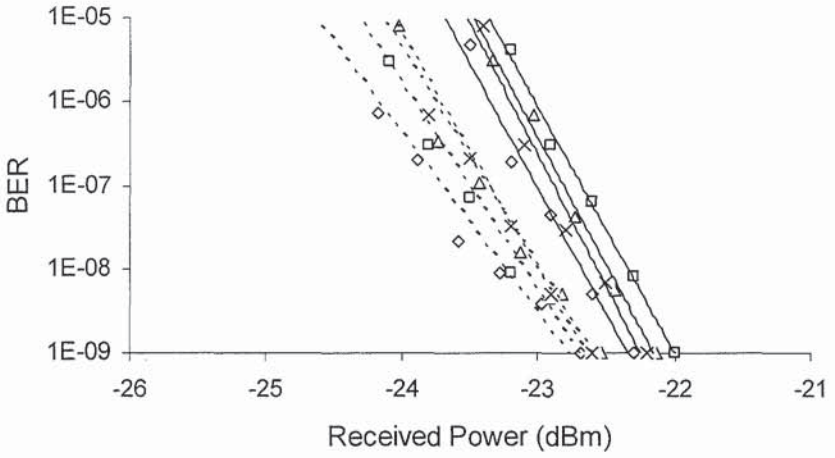

(b)

Fig. 4.34. Experimental result of BER characteristics for (a) NRZ (solid) and its converted CSRZ (dashed), and (b) RZ (solid) and its converted CSRZ (dashed).

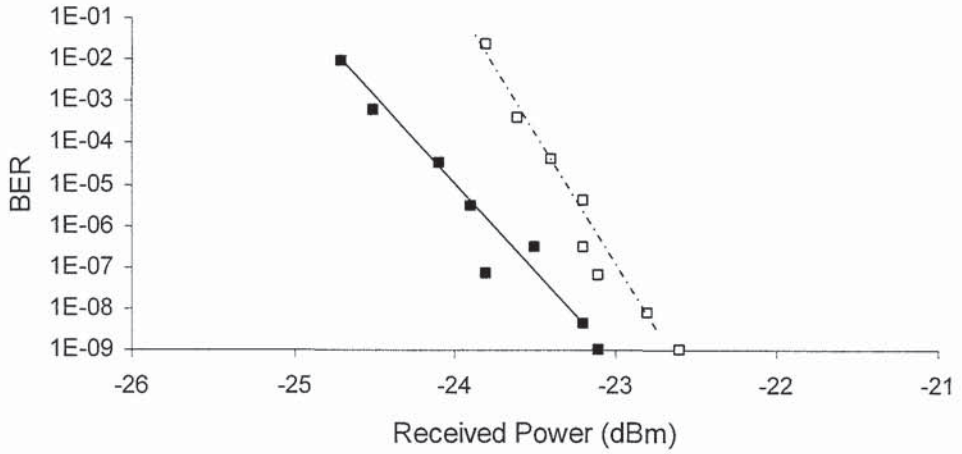

(a)

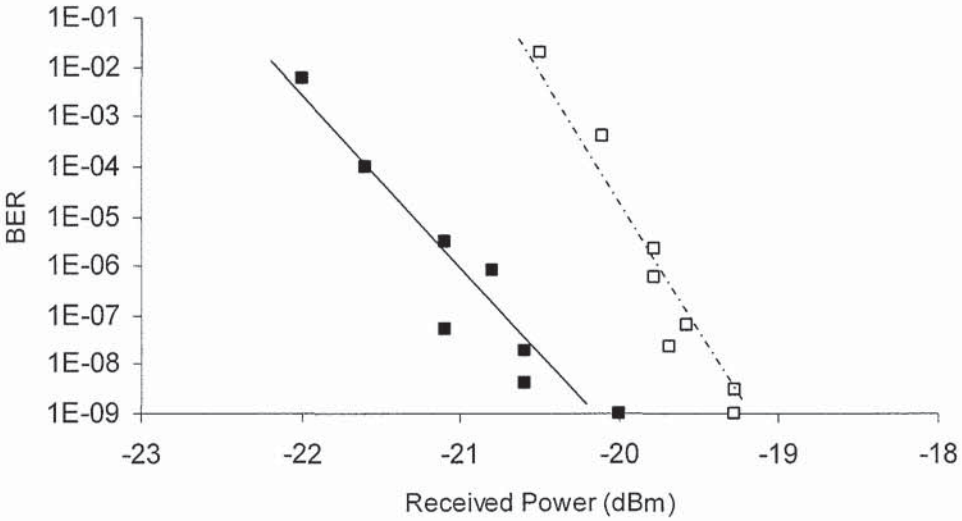

(b)

Fig. 4.35. Simulated result of BER characteristics for (a) CSRZ (solid) and its original format RZ (dashed), and (b) CSRZ (solid) and its original format RZ (dashed).

4.6 Conclusion

In this chapter, all-optical data format conversions between RZ to CSRZ and NRZ to CSRZ using SOA-NOLM have been demonstrated. The optical conversion bandwidth for this device has been presented. The multi-channel conversion has proved that the SOA-NOLM can be used as the CSRZ data source in WDM system. There is no significant chirp introduced into the converted data as shown by the pulse broadening measurement. The converted format, CSRZ has shown improved transmission performances as compared to that of the original formats. A 10 Gb/s error-free transmission for the CSRZ has been achieved up to 3000 km. This SOA-NOLM converter has shown the conversion and the transmission for 4 x 10 Gb/s WDM data with 100 GHz spacing. The receiver sensitivity for the converted four wavelengths is compared with the sensitivity of the original NRZ and RZ counterparts. The SOA-NOLM could serve as an important all-optical format converter in the OTDM and WDM networks.

Chapter 5

TOAD Symmetrical Switching Window

5.1 Introduction

All-optical switches and demultiplexers are fundamental building blocks for enabling future OTDM systems [66]. Semiconductor optical nonlinearities have been used to demonstrate efficient interferometric all-optical switches that promise to deliver switching on terabit/s data streams [28, 38]. Optical switches using an SOA as the nonlinear switching element have reduced the usage of long fibre lengths and high pulse energies. The first device, known as a SLALOM [33] or SOA-NOLM, was a major break through in realising all-optical switching. The SOA-NOLM incorporates an SOA placed off-centre in a loop mirror. The offset position of the SOA determines the temporal width of the switching window which controls the amount of switched and demultiplexed signals. The TOAD [26] further modifies the SOA-NOLM by reducing the SOA offset from the centre of the loop such that the transit time of the asymmetry is substantially less than the SOA recovery time. In this way, the fast rise time of the nonlinear response in the SOA can be utilised to generate a switching window that is much shorter than the SOA recovery time. The shortest possible switching window in the TOAD is limited by the rise time which is proportional to the SOA transit time. The edges of the switching window are dependent on the finite length of the SOA and the pulse widths [26]. As a result an asymmetrical switching window is produced. This is a main contribution to the channel crosstalk in TOAD/SOA-NOLM operation, which in turns affects the bit error rate (BER) performance and reduces switching speed [67]. An optical switch based on two cascaded TOADs that generates a narrow switching window has been reported to overcome this limitation [68]. However, in practice, the narrowest switching window does not

correspond to the best system performance. If the switching window is too narrow, the timing jitter in the received signal will be transformed into intensity noise in the switched signal and increase the BER [69]. Also, there is the possibility that a jittered pulse will fall outside of the switching window and hence be lost. Therefore, to trade off the effects of the crosstalk and the timing jitter, the switching window has to be optimised to realise the best performance. A symmetrical switching window has been proposed for a single TOAD switch by saturating the SOA from both directions using two identical pulses [70].

In this chapter, the TOAD's switching window is introduced. Then, the theoretical observation in [70] is experimentally conducted. It is believed this is the first time such an experiment has been demonstrated. The results are observed on a high resolution optical sampling oscilloscope ANDO AQ7750. This oscilloscope has capability to evaluate rising and falling time of pulses with its 0.6 ps resolution. It can also measure optical pulses for 2 ps or less in pulse width.

5.2 Switching window characteristic

Section 3.4 gives details about the operation of the SOA-NOLM or TOAD. The TOAD architecture is shown in Fig. 5.1, which is composed of an optical loop mirror, an SOA and an intra loop 3 dB coupler for injecting control pulses into the SOA. This section is not intended to repeat the explanation given in section 3.4, instead it will be focused mainly on the TOAD's switching window. A characteristic of the TOAD switching window is that the rising and falling edges have different timescales. The short rising edge is determined by the control pulse width whereas the long falling edge due to the length of the SOA. Mathematically, the switching window is given by a transfer function [33]

$$G(t)=\frac{1}{4}\left[G_{cw}(t)+G_{ccw}(t)-2\sqrt{G_{cw}(t)G_{ccw}(t)}\cos\Delta\phi(t)\right] \tag{5.1}$$

where

$$\Delta\phi(t)=\phi_{cw}-\phi_{ccw}=\frac{\alpha}{2}\ln\left(\frac{G_{ccw}(t)}{G_{cw}(t)}\right). \tag{5.2}$$

This transfer function is the ratio of the output to the input for the data pulse. The role of the loop asymmetry Δx in Fig. 5.1 is to shift both phase (and gain) responses ϕ_{cw} and ϕ_{ccw} (G_{cw} and G_{ccw}) relative to each other, thereby realising a differential switching window inside which data can be switched to the transmission port. The temporal width and height of the switching window can be adjusted with the delay, Δx in the fibre loop.

In the absence of the control pulse the TOAD operates as a linear loop mirror where all the optical power entering the input must be reflected. This is true provided that the relative polarisation of the two fields does not change as they traverse the loop. If a constant control pulse is applied to the SOA its optical characteristics will be modified. Modification of the SOA's gain and phase causes the clockwise, cw, and counter clock wise, ccw, pulses to experience power dependent interference when they arrive at the coupler. Since the loop is asymmetrically arranged, this creates a phase and gain difference as shown schematically in Fig. 5.2(a) and Fig. 5.2(b). The solid lines and the dashed lines are the gain and phase responses experienced by the cw and ccw pulses respectively. Initially, the gain is on the steady-state condition before the control pulse modifies an optical property of the SOA. The gain decreases once the pulse transits in the SOA. After this rapid transition, the gain recovers relatively slowly with time. Since, the ccw is delayed in time due to the SOA's offset, a switching window will be formed, in

effect from the difference in the phase shift. The phase shift is only needed to be introduced in one direction of the pulses in the loop. The corresponding phase differences are shown in Fig. 5.2(b). According to an Eq. 5.1, asymmetrical window will be generated as sketched in Fig. 5.2(c). This output intensity has a finite value determined by the delay time. Note that the width of the window is slightly larger than the delay between the two phase curves. The reason for this is that the phase change induced by the optical sampling pulse is not instantaneous in practice. As the switching offset, Δx, is decreased from a large offset, the window width decreases while the output amplitude remains constant. However, the amplitude begins to decrease in direct proportion with the window width until the effective switching point is zero at which the switching window nearly vanishes as shown in Fig. 5.2(d). The amplitude decrease is a result of the finite length of the SOA [71].

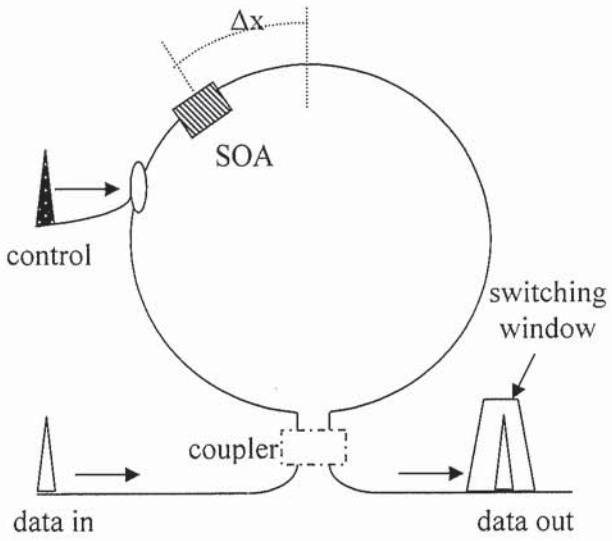

Fig. 5.1. The TOAD with switching window.

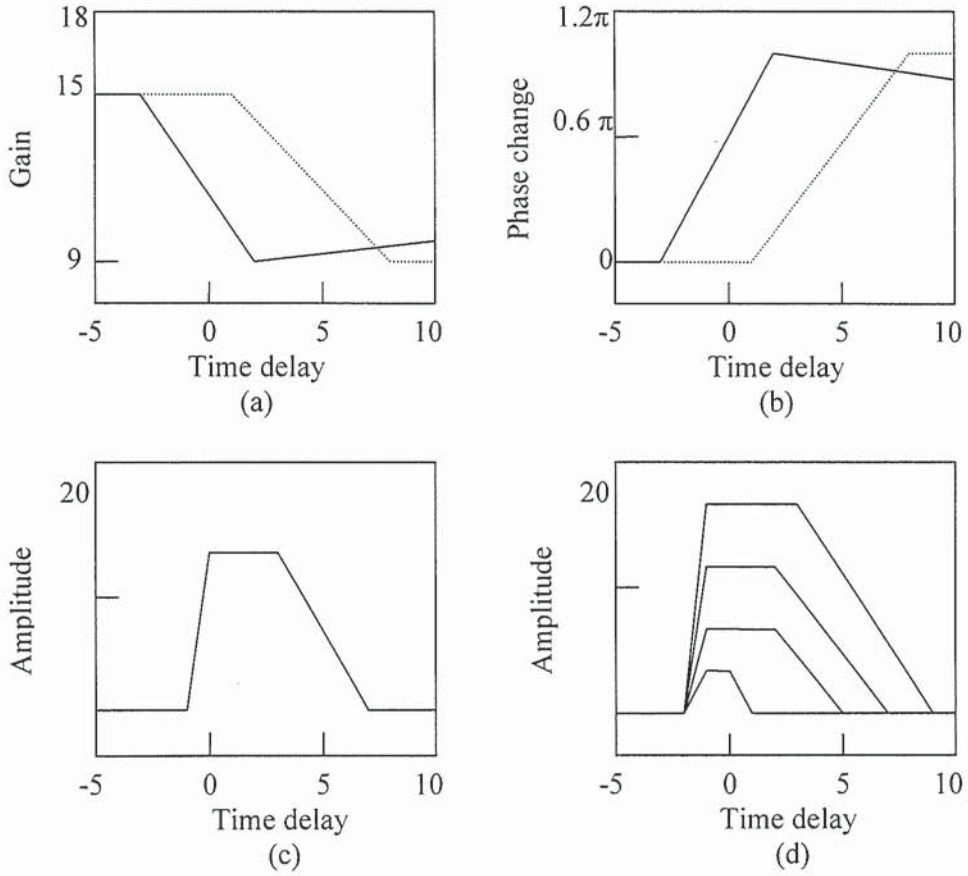

Fig. 5.2. (a) SOA gain response, (b) SOA phase response, (c) switching window, and (d) switching windows for difference offset.

5.3 Asymmetrical switching window

Fig. 5.3 shows a detailed profile of the asymmetrical switching window. The location of each edge is defined by the side of the fibre loop on which the SOA is located relative to the control signal. If the SOA is on the same side as the control, then the rising edge is very steep and the falling edge has a long slope. If the SOA is placed on the opposite side, the two edges are interchanged, the falling edge is steeper than the rising edge. The sharp rising edge in Fig. 5.3 is limited by the control pulse width. The slow falling edge is related to the propagation time of the SOA which is given by

$$T_{fall} = 2L/c, \tag{5.3}$$

where L is the SOA length and c is the speed of light in the SOA. The flat top width of the switching window is approximately equal to the time difference between the two counter propagating pulses separately arriving at the SOA, which is twice the temporal offset ($2\Delta x$) of the SOA from the fibre loop centre. There is an optimal injection current into the SOA to realise a high and flat switching window [69]. Insufficient injection current will reduce the signal gain and degrade the amplitude of the switching window as a result of the lower inversion. If the SOA is pumped too hard i.e. the response time is reduced, a greater phase and gain difference will result in a non-flat switching window. Therefore, the injection current which governs the carrier recovery time of the SOA must be properly adjusted according to the control pulse power. An ideal switching window has a flat top with 100% transmission inside the window (corresponding to a switch in its ON state) and 0% outside (OFF state) the switching window. In practise, these values are reduced by the losses and residual transmittance [72] in both the ON and OFF states. A small bump can also be seen outside the window if a high power control pulse is used. This is because of the combined effect of the gain and phase at the transition period in the interference term of the transfer function in Eq. 5.1 [73].

5.4 Symmetrical switching window

A symmetrical switching window that employs a single SOA has been theoretically predicted for the first time in H.L.Minh et. al. [70]. The window is created by applying simultaneously two identical control pulses into the SOA as shown in Fig. 5.4. In their calculation the SOA is divided into a number of small segments. Each segment is subjected to cw and ccw pulses independently. Thus the gain and phase modulations are the accumulation of the responses of all the segments. Hence, the cw and ccw data

components will experience the same amplification and saturation effects but delayed by $2\Delta x$. The gain profile for $G_{cw}(t)$ and $G_{ccw}(t)$ are the same but delayed in time as shown in Fig. 5.5 [70].

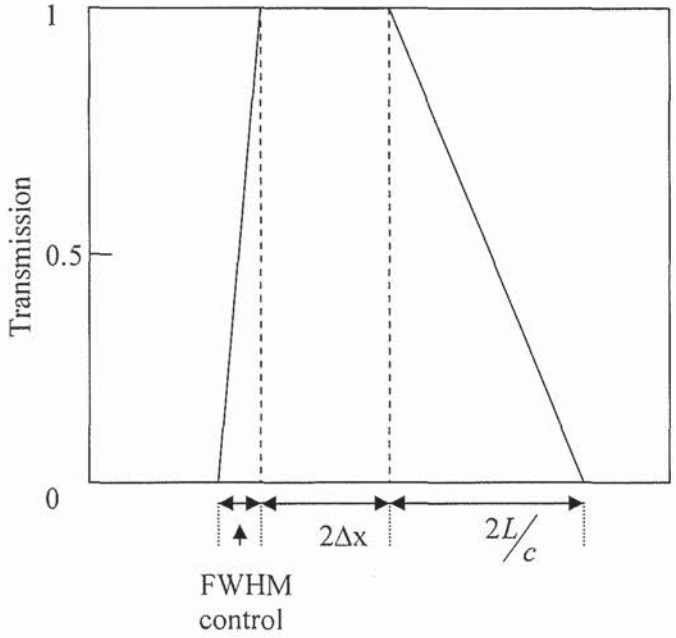

Fig. 5.3. The TOAD asymmetrical window.

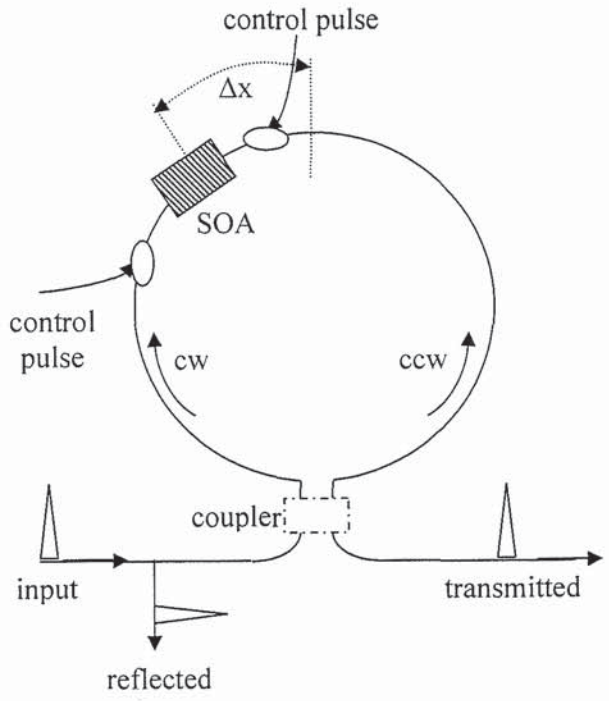

Fig. 5.4. The TOAD setup for symmetrical switching window.

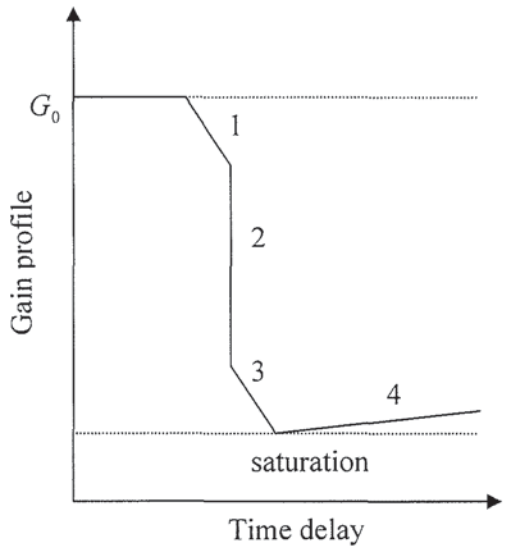

Fig. 5.5. The gain profile for symmetrical window.

There are four regions identified in the gain profiles shown in Fig. 5.5 i.e. 1, 2, 3, and 4. Region 1 displays identical slow responses of the gains when control pulses are at the first and last segments of the SOA as shown in Fig. 5.6. A steep transition in region 2 is because of the gain saturation. The SOA is further saturated with a slow response in region 3 due to the counter propagating control pulse. After both control pulses have left the SOA, the gain slowly recovers to its initial value. So, new data pulses will experience recovery gain characteristic in the region 4. Since both pulses undergo the same gain profile, a symmetrical window can be observed as shown in Fig. 5.7.

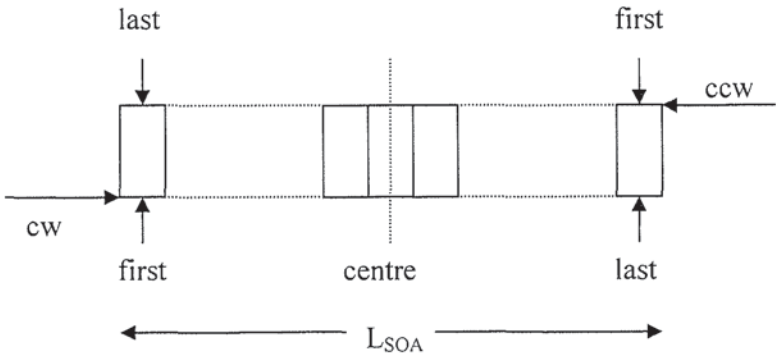

Fig. 5.6. SOA segments.

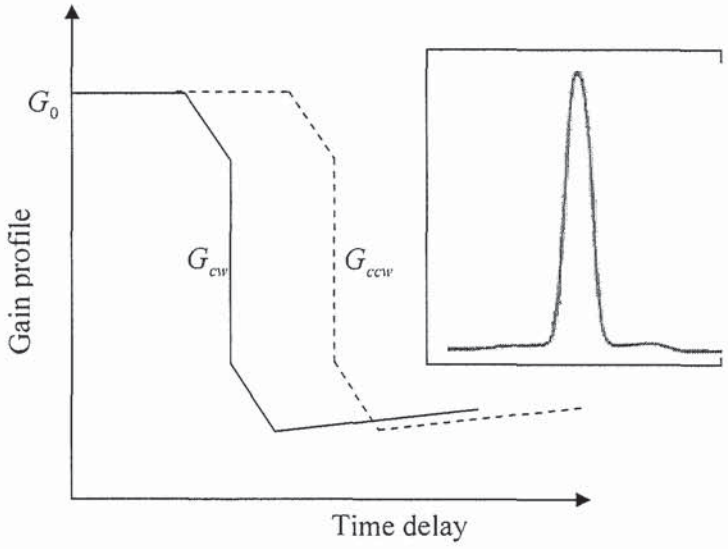

Fig. 5.7. The gain profile of the symmetrical window, and the switching window (inset) as shown in [70].

5.5 Experiment and results

The experimental setup for the symmetrical switching window measurement is depicted in Fig. 5.8. The control pulse at 1553 nm is generated by the Pritel laser source with 10 ps FWHM and 2.8 dBm average power. This control pulse is split into two equal branches to provide the two counter-propagating control pulses. An attenuator is added into one arm for controlling the power so that the two control pulses have equal power on entering the SOA. To make sure that the control pulses hit the first segment of the SOA at the same time from both directions, a delay line is used in the other arm. A continuous wave, CW at wavelength 1548 nm and average power of -14.0 dBm is introduced into the input port of the loop. The transmitted power is monitored by high resolution sampling oscilloscope ANDO AQ7750. The output intensity represents the switching or sampling window which is given by Eq. 5.1. Fig. 5.9 shows the switching windows for a single control pulse and

for dual control pulses. The falling edge is measured to be 15 ps, which is 1.6 ps wider than the calculated value by Eq. 5.3. In the case of dual control pulses, the rising and falling slope is equivalent to 15 ps. The symmetry of the switching window is observed at the expense of a lower peak value. The base of the switching window is not completely flat as shown in the circle of Fig. 5.10, because of the slow response in region 1 and 3 of the gain profile. A higher bump on the trailing edge is expected due to the relative delay of the control pulses. Fig. 5.11 depicts a 35 ps symmetrical switching window which is observed by increasing Δx in Fig. 5.8. The leading edge shows the same width with the trailing edge in this figure. This again confirms the symmetry of the switching window.

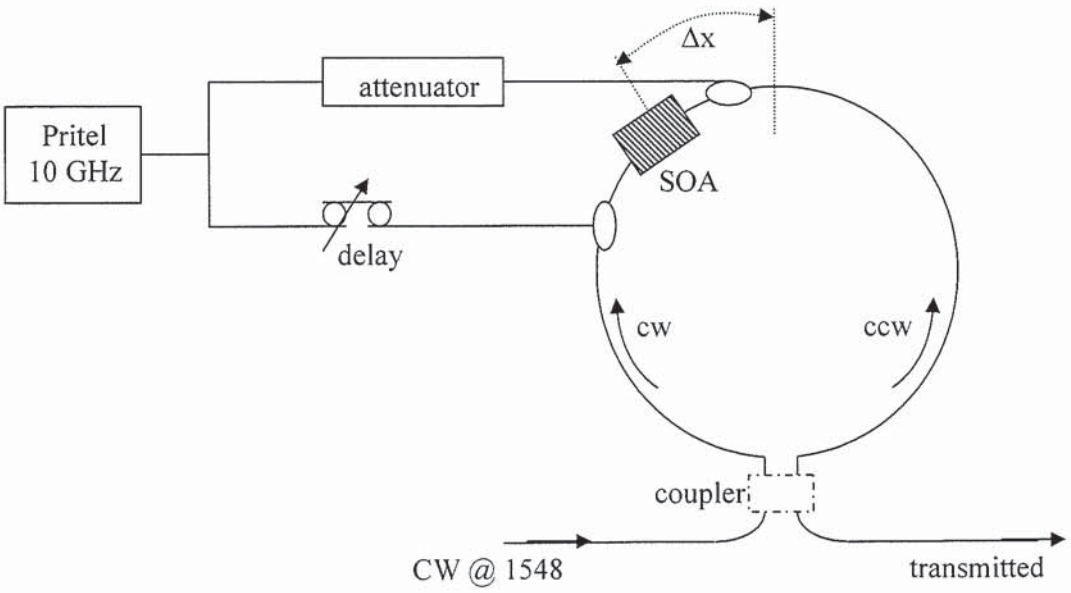

Fig. 5.8. Symmetrical TOAD switching window.

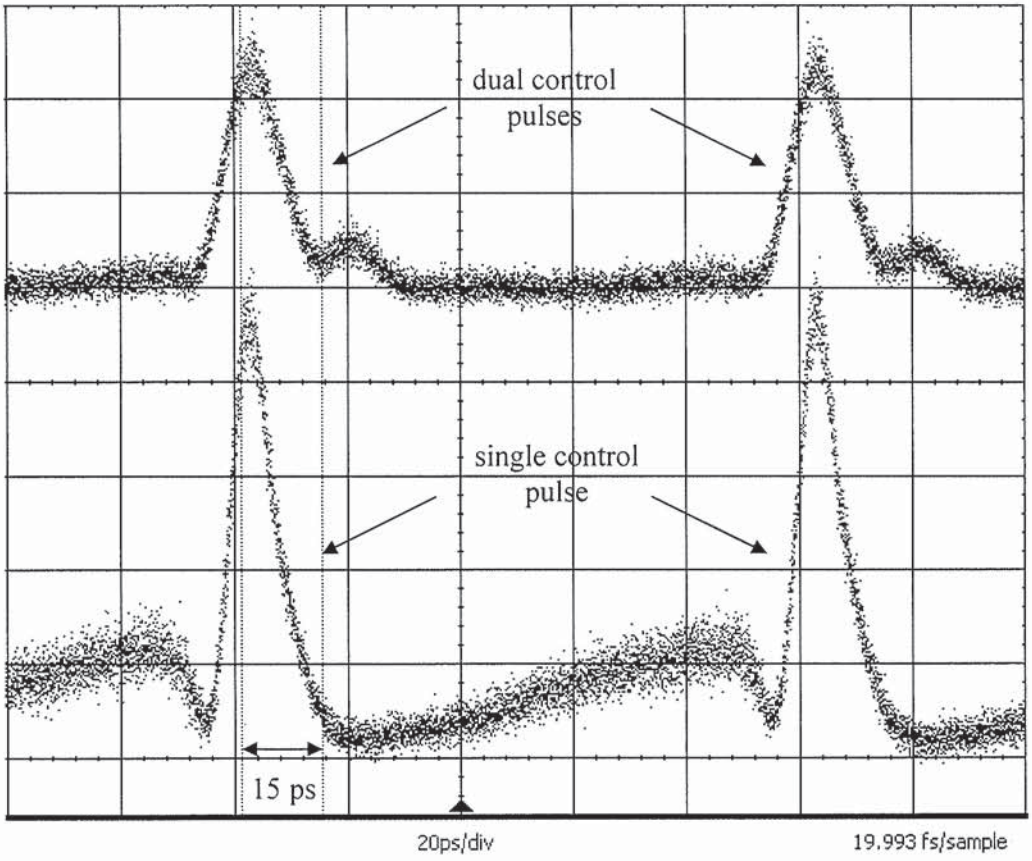

Fig. 5.9. The switching windows for single and dual control pulses.

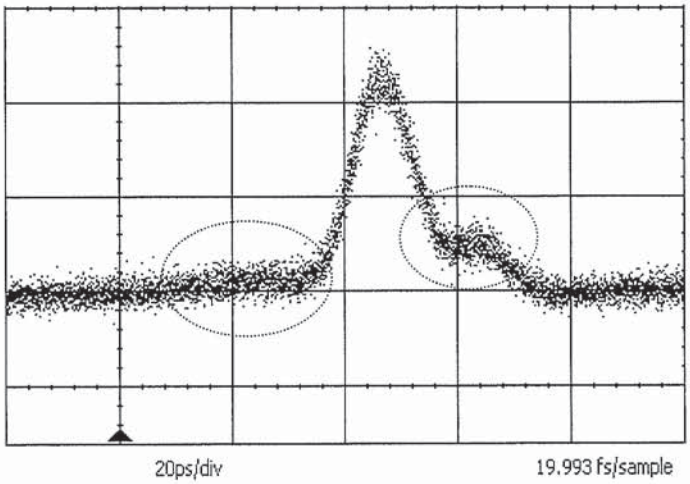

Fig. 5.10. The switching window is not completely flat.

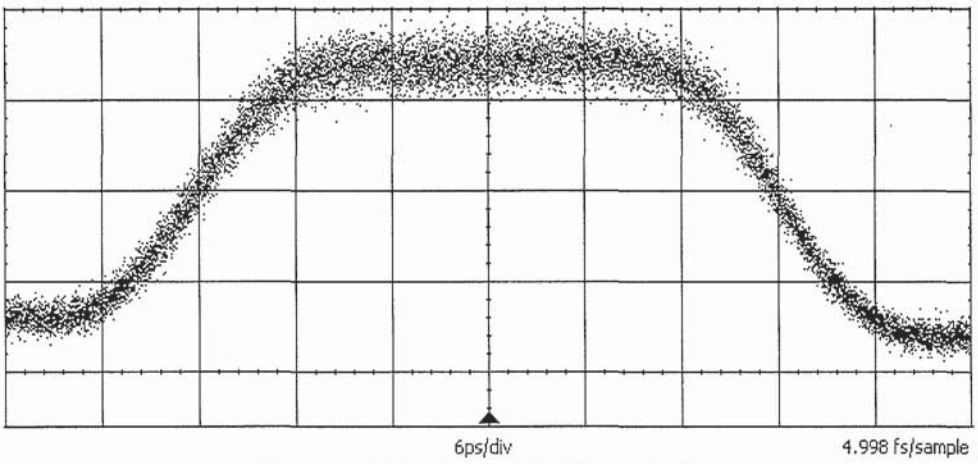

Fig. 5.11. The 35 ps switching window.

5.6 Conclusion

In this chapter, a symmetrical switching window has been presented. The switching window is not completely flat. The switching window in this experiment is slightly wider than the theory by 1.7 ps. The edges of the symmetrical switching window are controlled by the length of the SOA. The width of the switching window is dependent on the SOA offset. These results have been observed to be in a good agreement with the symmetric sampling window which was theoretically reported earlier [70].

Chapter 6

Circulating Shift Register: Transient Behaviour

6.1 Introduction

The idea of using shift registers to generate sequences of ones and zeros has been explored, developed and refined over more than five decades. Principally, communications have made use of the sequences generated. Nowadays, the shift register is being transformed from its electronic version to optical based designs due to the demand in high speed all-optical communication. The first all-optical shift register was proposed and demonstrated by Whitaker et al. [74]. The scheme employed a nonlinear optical loop mirror composed of a dispersion shifted fibre in a fibre loop and offered ultra fast switching capability. The advantages of using an SOA as the nonlinear element in all-optical switching techniques have been deployed in circulating shift register due to its integrability and low switching energy requirement. Since then, recirculating shift registers have been demonstrated using the SOA-NOLM switch with feedback [75], the ultrafast nonlinear interferometer, UNI [76] and by exploiting SOA self-phase modulation to achieve polarisation independent operation [77]. All-optical circulating shift registers will be a key component in future all-optical signal processing for the realisation of ultra-high speed OTDM switching networks [78].

In this chapter, the circulating shift register with an inverter using an SOA-NOLM [75] is presented. The main objective is to analyse the amplitude transient which is observed in this device. The variation of the power transient is plotted and compared with theoretical results.

6.2 All-optical circulating shift register

The operation of the circulating shift register can be described by a schematic diagram in Fig. 6.1, which consists of an SOA-NOLM with feedback arranged in such a way that the reflected signal returns to the SOA as a control pulse. Initially there are no control pulses in the feedback loop and the signal pulses are reflected by the SOA-NOLM through the 50:50 coupler. This is because the SOA remains unchanged and hence no phase difference is created between the two counter-propagating pulses in the fibre loop. If the reflected signals are amplified, in this case to a power level at least ten times higher than the input signals [80], polarisation rotated, and fed back into the loop as a control pulse, a circulating shift register function is obtained. The use of the reflection port for feedback causes the inversion of the logical value of the control pulse. Thus the temporal output will show blocks of pulses of '1' and '0'. The length of the shift register is determined by the feedback delay time which is the time between a signal pulse arriving at the loop centre and that pulse returning to the loop centre as a control pulse [74]. Mathematically, the period of each block is given by

$$T_B = L\left(n/c\right) \tag{6.1}$$

where L is the sum of half the length of the SOA-NOLM and the feedback path, n is the refractive index of the fibre and c the speed of light in vacuum. The total length, L can be measured using longitudinal mode frequency spacing equation [81],

$$\Delta f = \frac{c}{2nL} \quad . \tag{6.2}$$

This length is defined by the loop ABCDA in Fig. 6.1. If BD is disconnected, the loop forms a ring laser. By increasing the amplifier gain of the EDFA until lasing occurs and measuring the output on an electrical spectrum analyser, the value of Δf can be obtained.

Thus the length of the block of pulses can be determined accurately. The period of each block can also be written as

$$T_B = mT_{bit} \tag{6.3}$$

where m is the number of bits in the shift register and T_{bit} is the period of each bit. In order to ensure pulse synchronisation, m must be an integer number, which can be achieved by adjusting the total length, L.

Since the SOA is offset in the loop, the counter-propagating, ccw, pulses experience different dynamic gain states which in turn induces a different phase shift and thus switching can occur at the transmission port. A model of the loop response incorporating the dynamics of the SOA that explains the behaviour of the circulating shift register has been presented by K.J.Blow et. al. [82]. In this model, the rate equation of an SOA [33] for the carrier densities immediately after the j th pulse, n_j^+ and before the j th pulse, n_j^- are used. Thus, the transmitted energy for the j th signal pulse can be written as

$$E_j = \frac{1}{2}E_o\left\{1+\cos\left[\Theta\left(n_j^+ - n_j^-\right)\right]\right\} \tag{6.4}$$

where E_o is the input pulse energy and $\Theta\left(n_j^+ - n_j^-\right)$ is the phase difference experienced by the current signal pulse which arrives between the clockwise and anti-clockwise parts of the feedback pulse. This system also demonstrates a type of fibre loop memory, because the pulse transits the loop twice: once as the signal and once as the control. Hence, the system retains the information about the initial state [74].

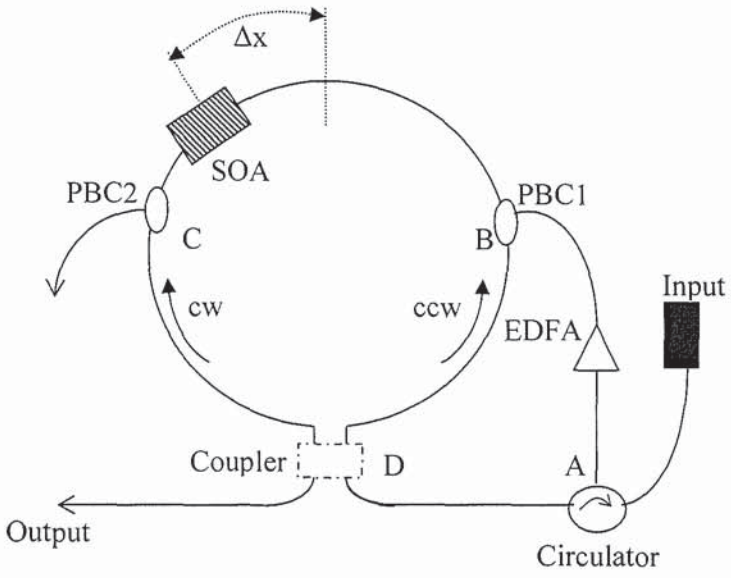

Fig. 6.1. Schematic diagram of the circulating shift register.

6.3 Experiment and results

Fig. 6.2 depicts the experimental setup used in this work. The optical source is a gain switched distributed feedback laser with a peak wavelength of 1557 nm and driven at a repetition rate of 2.49 GHz. The 25 ps pulse is generated and further reduced timing jitter by using the injection seeding technique [79]. The seeding power is -3.2 dBm provided by a tunable CW source at a wavelength of 1556.95 nm. These pulses are amplified and filtered before being injected into the fibre loop through a circulator. The reflected pulses are then appropriately amplified by an EDFA and are fed back to the fibre loop as control pulses. The feedback is coupled into the loop via a polarisation beam combiner, PBC. Two polarisation beam combiners are used to inject and to reject the control pulses respectively. There are six polarisation controllers labelled from PC1 to PC6 that maintain the polarisation state in the experiment. PC1 and PC2 are mainly used to adjust the

polarisation state of the reflected pulses so that they are orthogonal to the input pulses in the fibre loop. The other PCs are principally to increase the extinction ratio of the SOA-NOLM. The SOA is asymmetrically placed from the centre to create a 140 ps switching window. The transmitted pulses are observed on the 3.2 GHz LeCroy real-time oscilloscope.

6.3.1 Blocks behaviour

Blocks of pulses which are switched out from the fibre loop are shown in Fig. 6.3. The period of the square wave is twice the block length. It shows that all pulses are either completely switched or unswitched. This block pattern is stable for more than 24 hours until the polarisation drifted. The block length in terms of the feedback delay time is 383.86 ns which is measured directly on the real-time oscilloscope. Thus the number of pulses in one period is 960. The calculated block length based on an electrical spectrum analyser measurement of the mode frequency spacing, Δf ($\Delta f = 2.606$ MHz) is 78.31 m. The electrical spectrum is shown in Fig. 6.4. This long feedback length is mainly contained within the EDFA which is used to amplify the feedback section. Fig. 6.5 depicts an example of optical memory where three bits of pulses are removed from the block by slightly changing the polarisation state of the fibre loop. Although the pulses are removed at random, the procedure is simple and sufficient for the purpose of difference pattern. Specific pulse sequences could be stored by modulating the first block entering the loop. The removed pulses are clearly seen in the zeros region and are extremely stable (many hours).

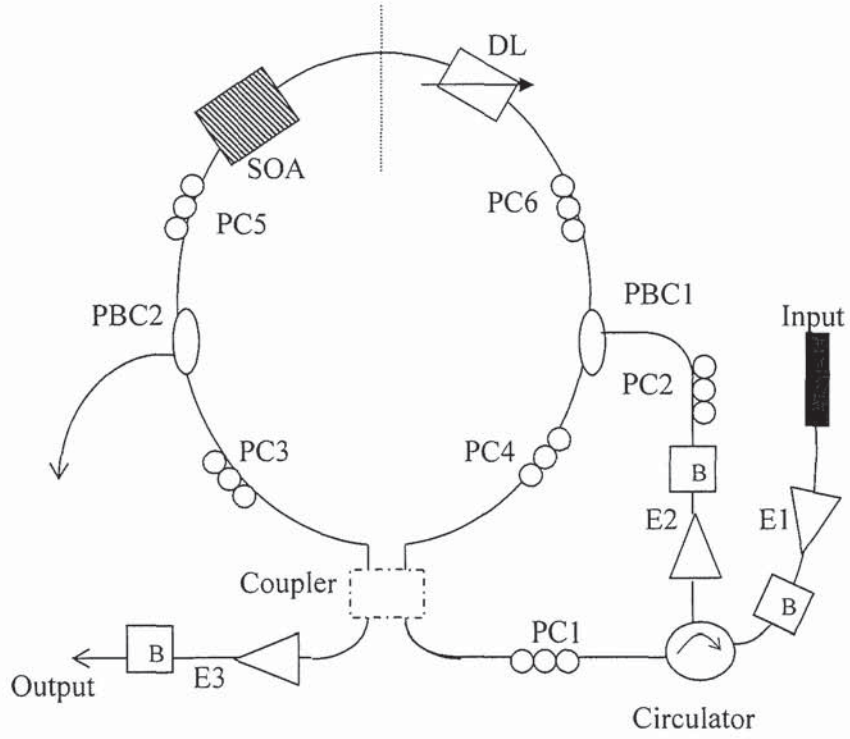

E1, E2, E3 and E4 – EDFA
PC1, PC2, PC3, PC4, PC5 and PC6 – Polarisation controller
PBC1 and PBC2 – Polarisation beam combiner
B – Band pass filter
DL – Delay line

Fig. 6.2. Experimental setup of the circulating shift register with an inverter.

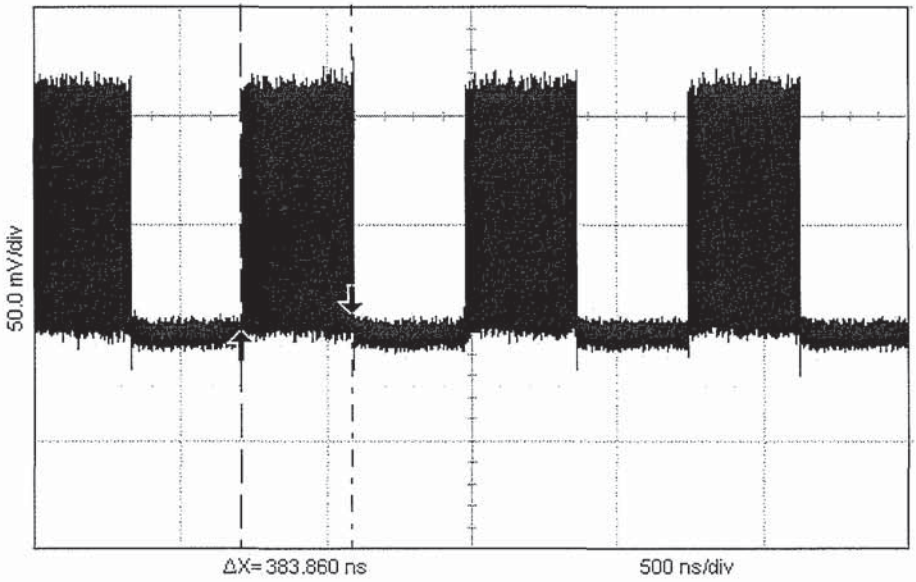

(a)

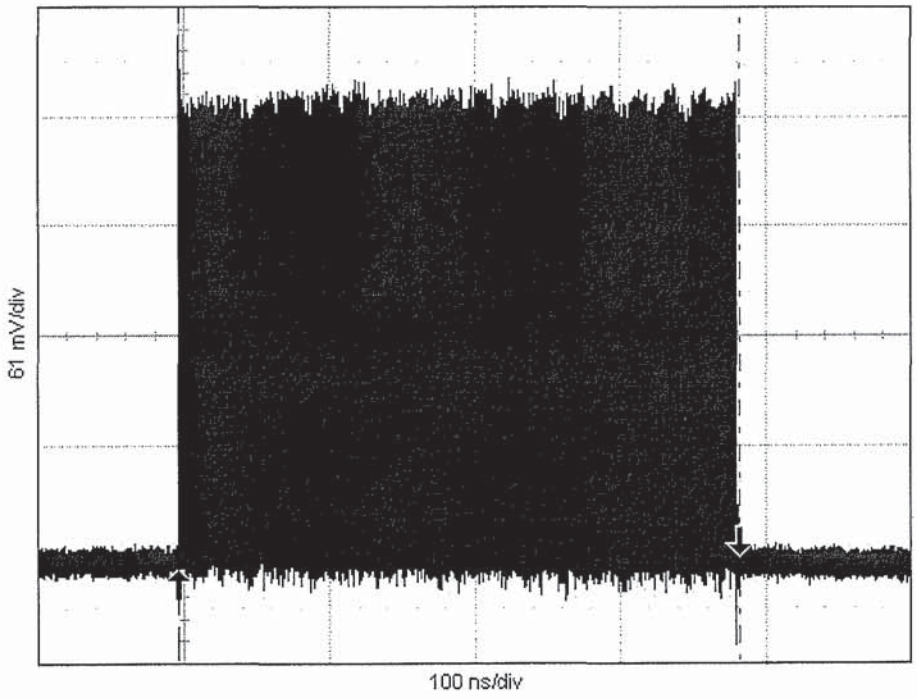

(b)

Fig. 6.3. Experimental output from circulating shift register. (a) many blocks and (b) single block.

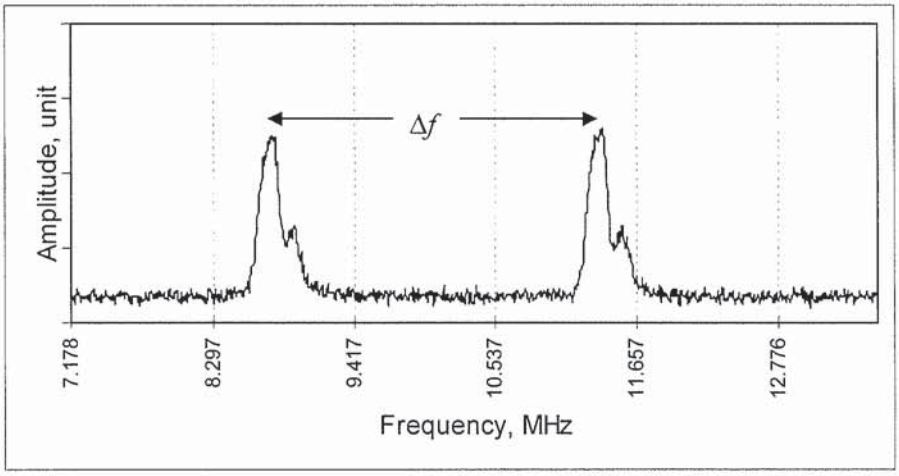

Fig. 6.4. Measurement of block mode spacing from the RF spectrum analyser used to calculate the feedback length.

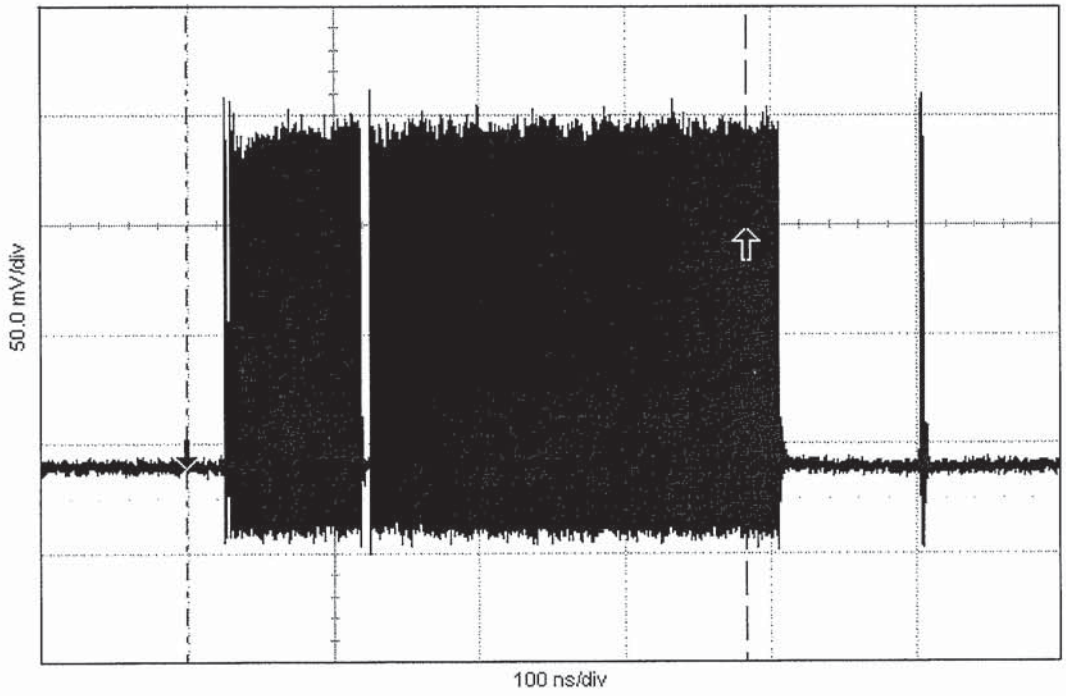

Fig. 6.5. Experimental output of the shift register where three bits are removed.

This shift register has been modelled in a very simple way [82]. The model assumes the pulses can be represented by delta functions in time and leads to a set of simple equations as given by Eq. (6.4). The same parameters are used as in [82]. The block behaviour has been observed experimentally and theoretically for different input powers as shown in Figs. 6.6 and 6.7. The figures show that both the contrast ratio between the stored ones and the stored zeros changes with the input power. The theoretical curves also show some small changes in the ringing observed at the transition between the block of ones and the block of zeros. In general, this behaviour is masked by the noise in the experimental signal. The block behaviour for different SOA drive currents is shown in Figs. 6.8 and 6.9. At high currents we see that the blocks are not cleanly stored. It is important to remember that these comparisons between the theory and experiment are not fully quantitative as the model contains a number of effective parameters which are not simply equal to the experimental parameters. For example, the theory ignores the dependence of the lifetime on the electron density and so the current in the model is not equal to the current in the experiment. However, the types of behaviour observed in both cases are similar. Other more exotic block behaviours are depicted in Fig. 6.10. However, it is difficult to get similar simulated results which are plotted in Fig. 6.11. This is because the output from the simulation is indicative of chaotic behaviour and in this regime we would expect very sensitive dependence on real parameters and initial conditions. Many of the parameters can be changed in the model that lead to similar outputs.

Finally in Fig. 6.12 we show the simulated results obtained when a few bits are removed from a block in order to see more complex memory-like behaviour. The results have shown a good qualitative agreement between the experiment and the simulation. Although the model is quite simple, it is useful enough to understand the behaviour of the shift

register. The model will be used in the next section to analyse the transient observation in the first few pulses of the shift register.

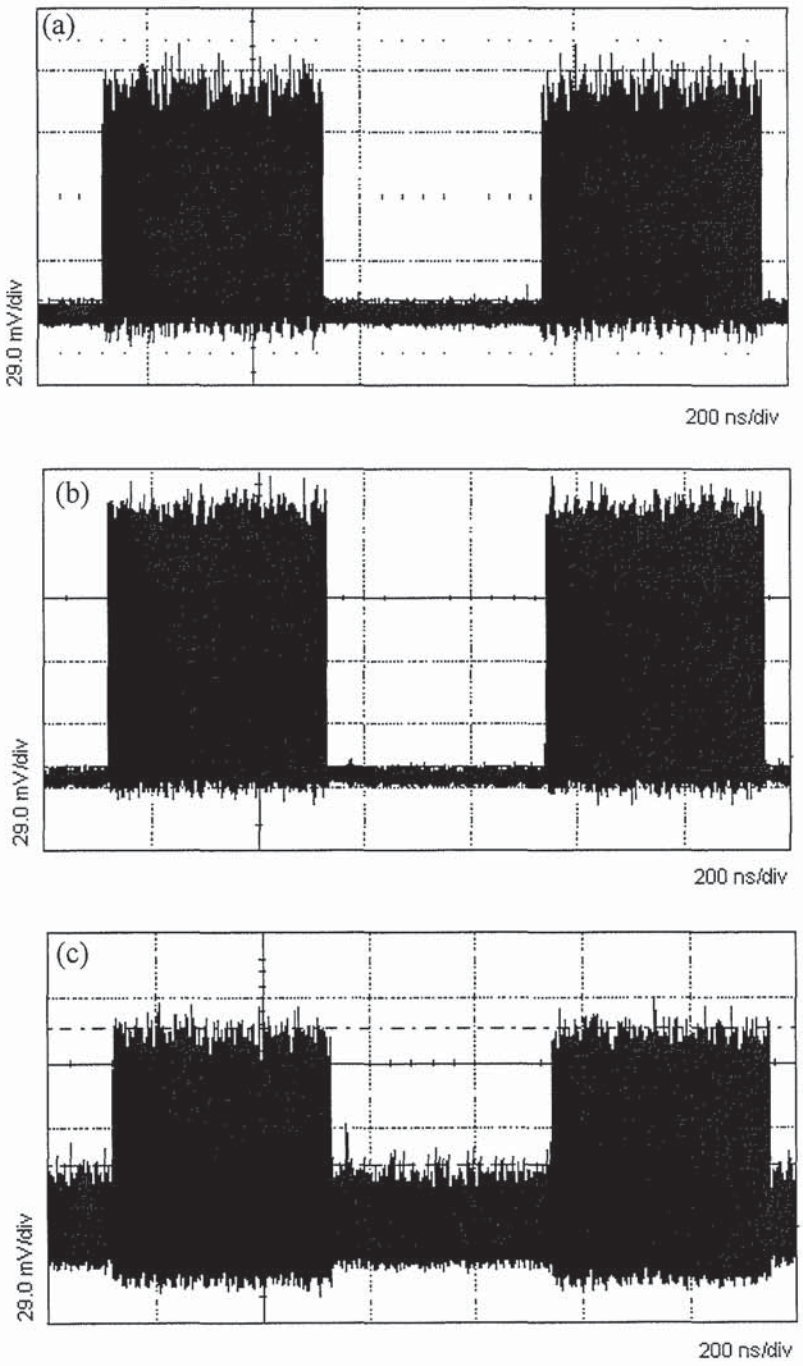

Fig. 6.6. Experimental output of the shift register at different input powers (a) 0.2 mW, (b) 0.3 mW, and (c) 0.4 mW.

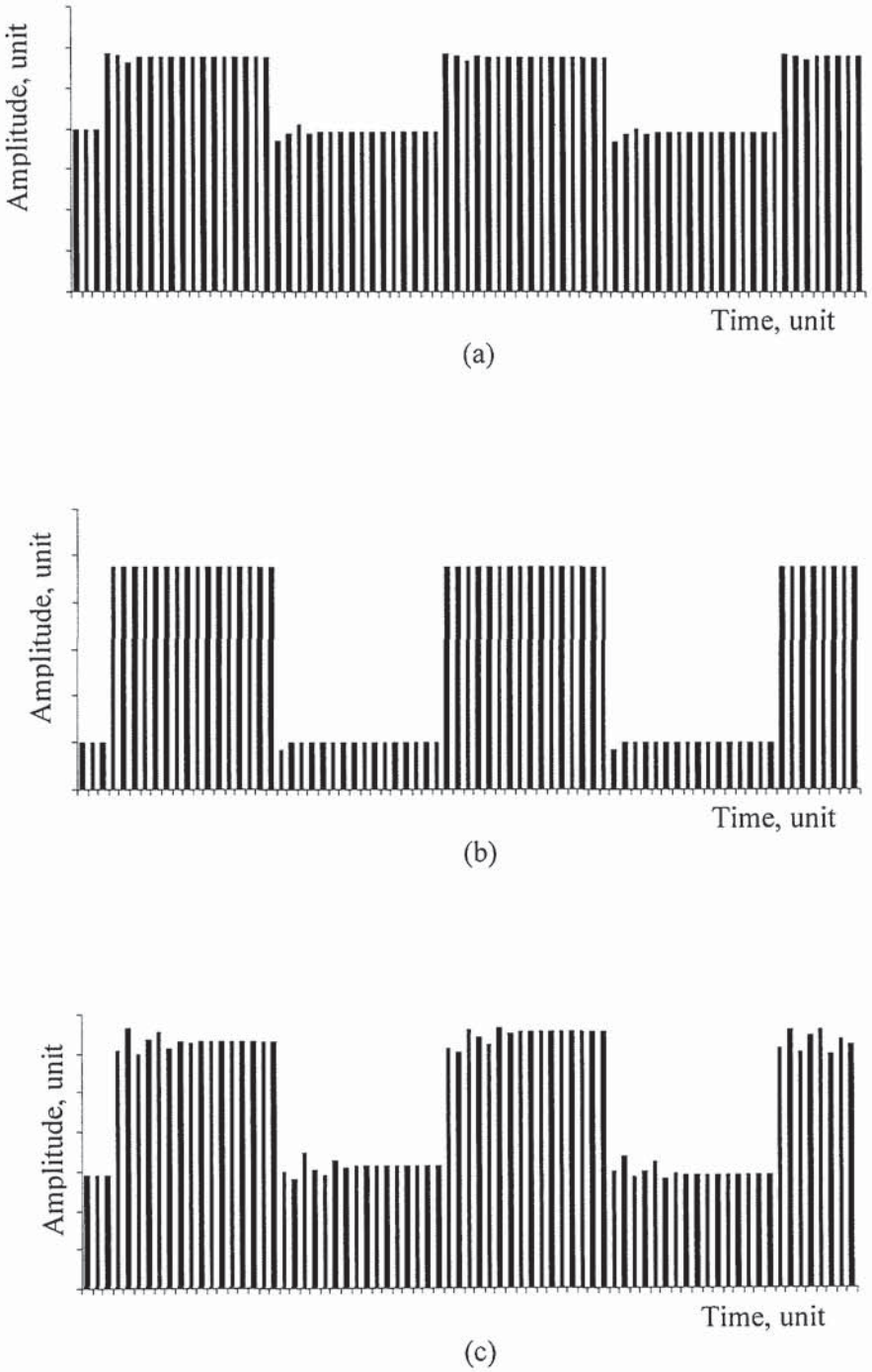

Fig. 6.7. Simulated output of the shift register at different input powers (a) 0.2 mW, (b) 0.3 mW, and (c) 0.4 mW.

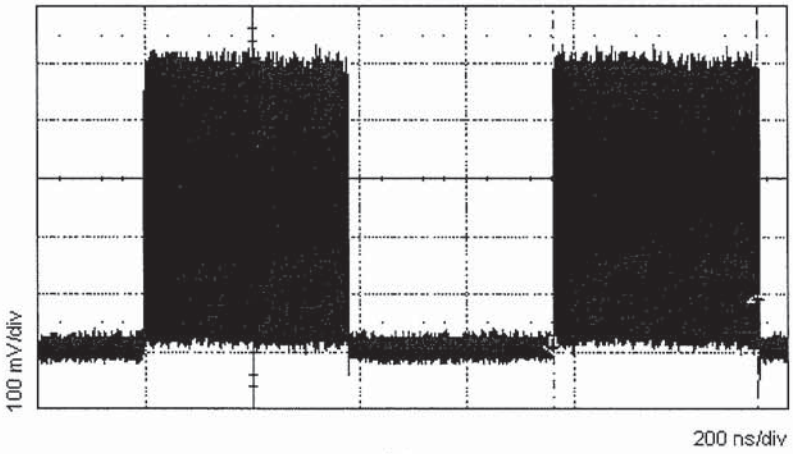

(a)

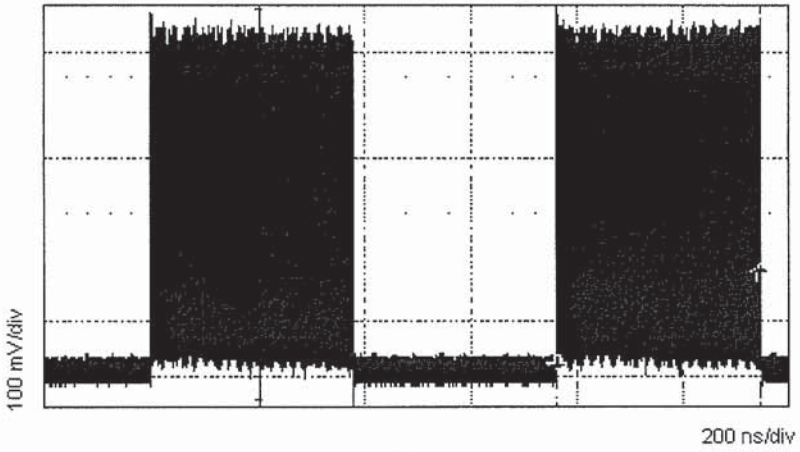

(b)

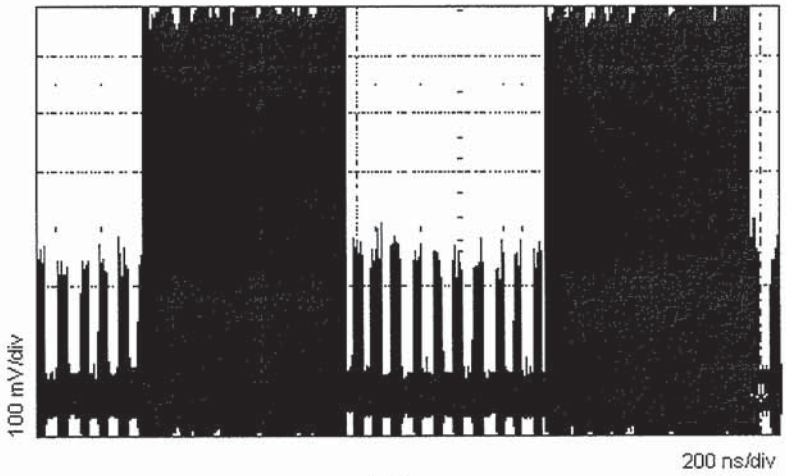

(c)

Fig. 6.8. Experimental output of the shift register at different currents (fixed input). (a) 170 mA, (b) 200 mA and (c) 230 mA.

(a)

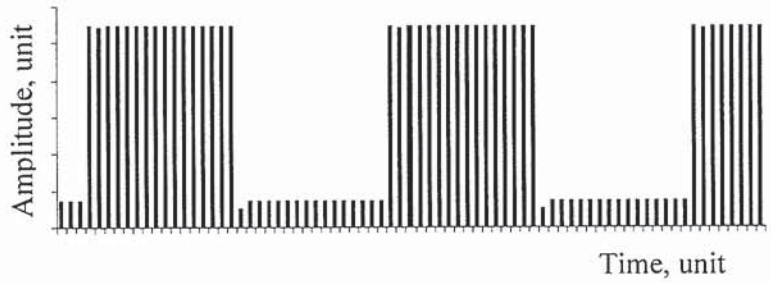

(b)

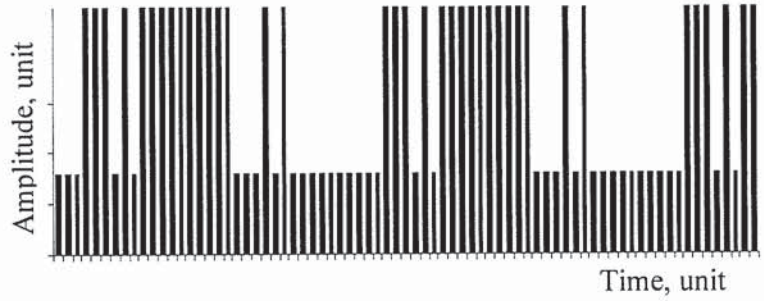

(c)

Fig. 6.9. Simulated output of the shift register at different currents (fixed input). (a) 170 mA, (b) 200 mA and (c) 230 mA.

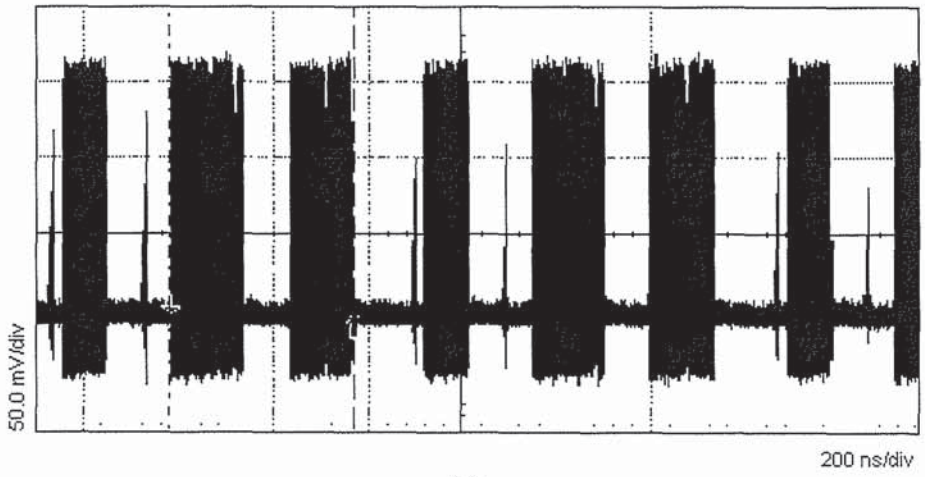

(a)

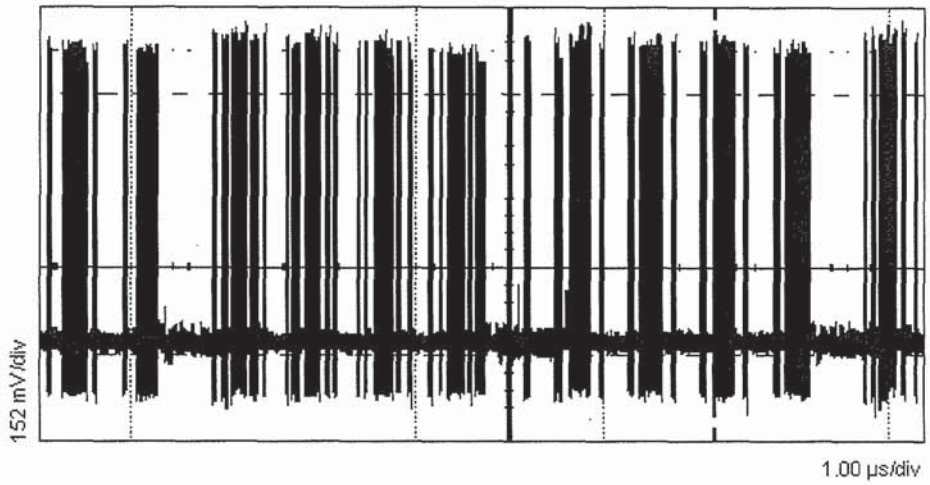

(b)

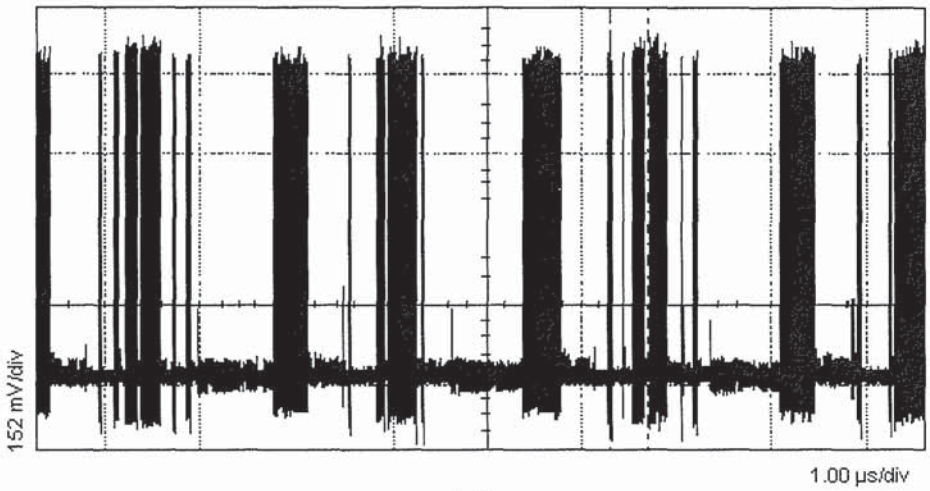

(c)

Fig. 6.10. Experimental output of other block behaviours. (a), (b) and (c).

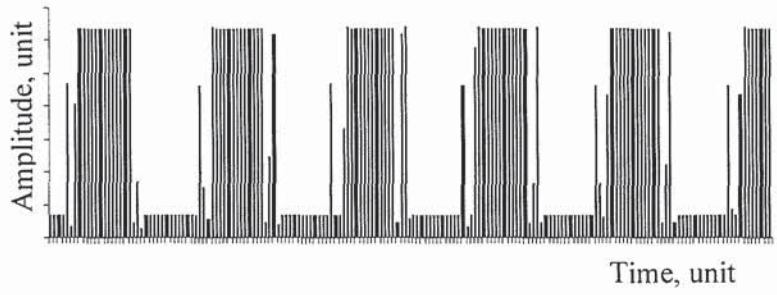

(a)

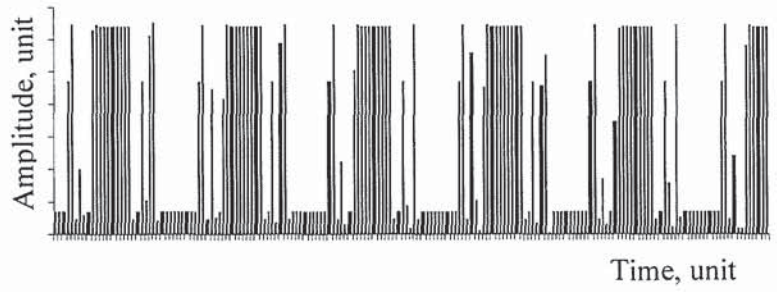

(b)

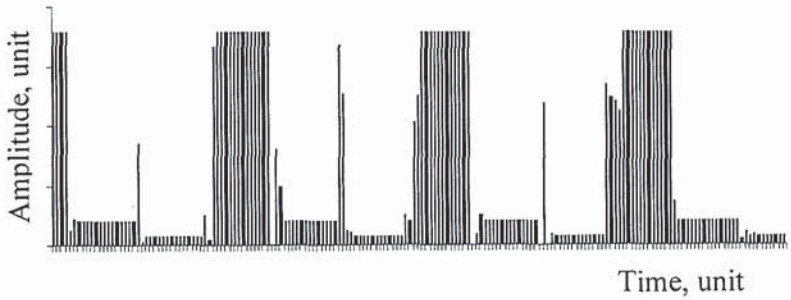

(c)

Fig. 6.11. Other simulated block behaviours. (a), (b) and (c).

(a)

(b)

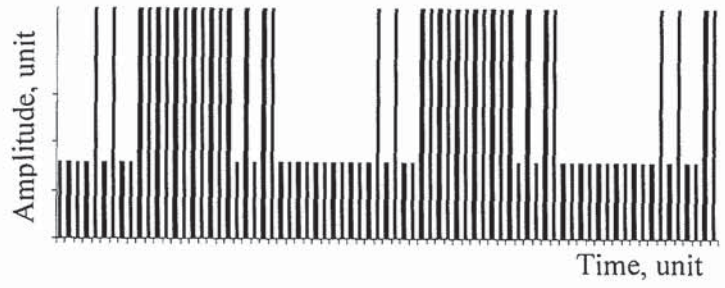

(c)

Fig. 6.12. Simulated output of register where a few bits are removed. (a), (b) and (c).

6.3.2 Transient analysis

In the previous section, the block behaviour has been observed macroscopically. If the block is analysed independently in detail one can see a transient power in the first few pulses before the steady-state or flat top is reached. Generally, the transient is a temporary wiggle, the response of a system on the way to settling down into an equilibrium or steady-state. The transient behaviour depends on the operating conditions of the switch, for example it changes with changes in the input pulse power or with changes in the injection current. Fig. 6.13 shows an example of the transient power that can be seen in the first few pulses of the circulating shift register.

An example of the predicted output is shown in Fig. 6.14. A stable block output is obtained but note that the block output has some amplitude modulation on the first few pulses. This is also seen in Fig. 6.13. Now, the transient behaviour in the experiment can be compared with the theory. To do this the transient power is defined by

$$P_{transient} = P_o - P_s \tag{6.5}$$

where P_o is the power of the first pulse and P_s is the average power of the pulses when steady-state is reached as indicated in Fig. 6.13. The transient powers that have been extracted from the experiments and the theoretical data are plotted in Fig. 6.15. Similar trends are observed in both graphs therefore they are in a good agreement. Fig. 6.15(a) shows a wider range of input power when compare to Fig. 6.15(d). At low injection current, the input power that needs to be applied into an SOA is reduced. This causes the circulating shift register to be more stable and a wider range of the input power can be utilised to observe the block behaviour. However, the block of pulses deteriorates as the injection current is increased. Hence, a shorter range of the input power is allowed to form the block behaviour as shown in Fig. 6.15(d). If the injection current is further increased,

the block of pulses will disappear irrespective of the value of the input power. The area under the curve is becoming smaller as the injection current approaches its maximum value. This area represents the stability of the shift register. The optimum range of the input power is between 0.2 to 0.4 mW. Fig. 6.15(e) shows the effect of increasing the injection current with the input power. With a higher inversion inside the SOA, less energy is required to saturate the amplifier. The dependency of the transient on the input power and the injection current is clearly seen in Figs. 6.15(e) and 6.15(f). There is a 0.2 mW difference between the theory and the experimental value of the input power that was required in this shift register as depicted in Fig. 6.15(f). This is because the model has used a constant recovery time, τ whereas in the actual experiment it is dependent on the injection current into the SOA. That explains why the curves plotted in Fig. 6.15 are not showing a perfect match with the theory. The transition point where the maximum transient power occurred is 200 mA for both theory and experiment. The peak of the transient power can be seen at a lower input power if the SOA is biased at a higher current. Although the most stable shift register state is accompanied with the transient, this does not mean that the transient could not be completely removed. With a proper adjustment of the input power and the polarisation controllers, the transient can be slowly reduced and removed from the blocks. However, this will reduce the extinction ratio between blocks of ones and zeros. Thus, it will affect the stability of the shift register.

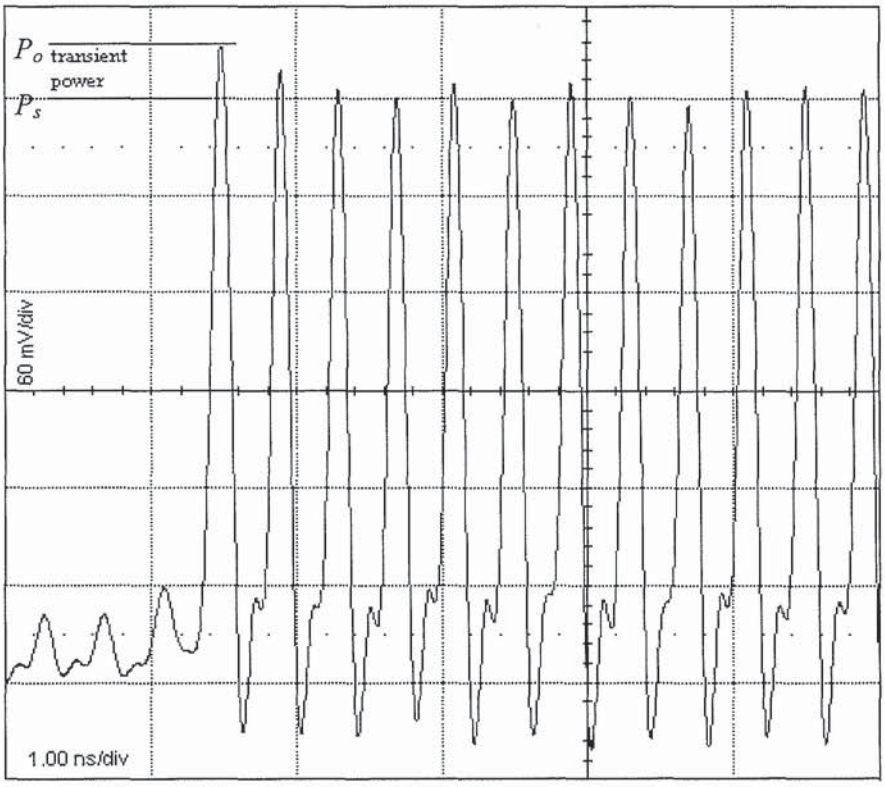

(a)

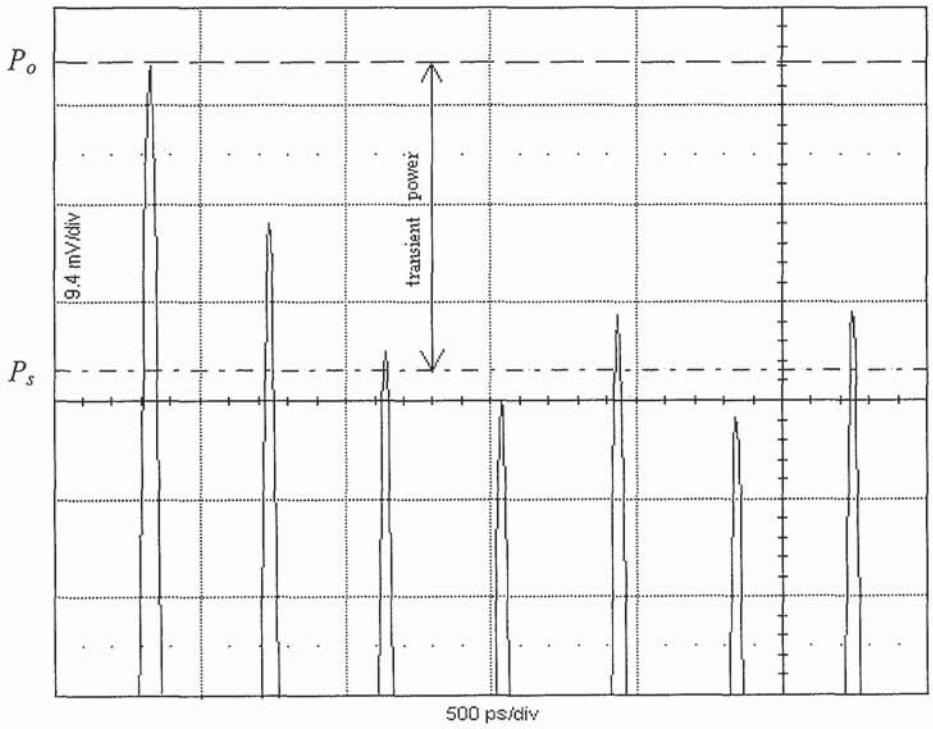

(b)

Fig. 6.13. Transient power in circulating shift register. (a) small scale, and (b) large scale.

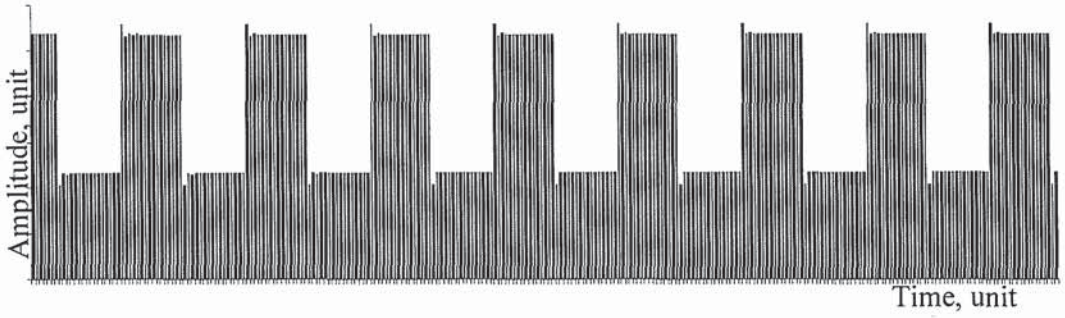

Fig. 6.14. Simulated temporal shift register.

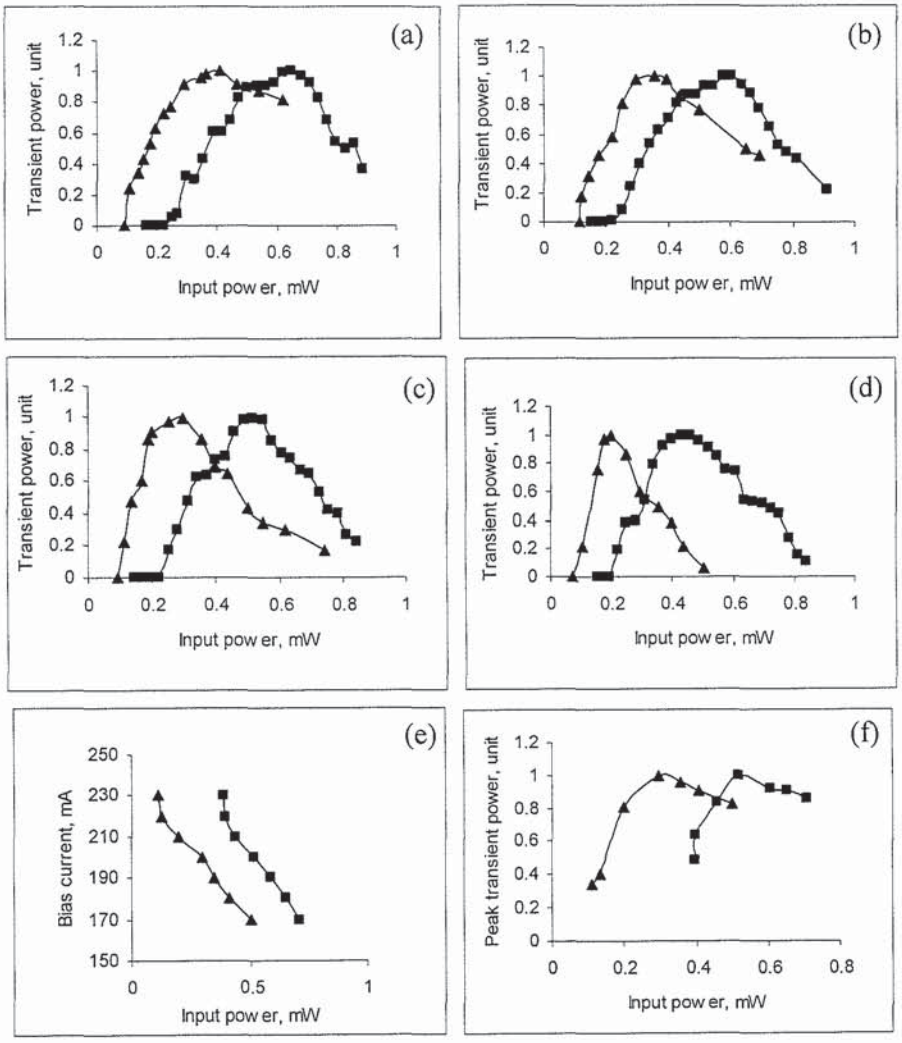

Fig. 6.15. Transient power versus input power; (a) 180 mA, (b) 190 mA, (c) 200 mA, and (d) 210 mA. (e) SOA bias current versus input power. (f) Peak transient power versus input power.

6.4 Conclusion

In this chapter, an all-optical circulating shift register has been demonstrated. The circulating shift register can be a basic building block for other applications such as optical memory and clock division [83]. The blocks behaviour from the theoretical prediction has shown similar trend with the observation from the experiment. The blocks of pulses are very stable for more than 24 hours. The stability can be extended if the experiment is conducted in an environment where the polarisation is stabilised. The transient power has shown a good agreement between the experiment and the simulation. The transient power is dependent on the input power and the SOA's bias current.

Chapter 7

Conclusions and Future Work

7.1 Introduction

This work investigates all-optical interferometric switches based on semiconductor optical amplifiers and their application to all-optical signal processing. The objectives which are mentioned in chapter one have been successfully achieved and shown in their respective chapter. The research is carried out mainly by using experimental techniques. The new results presented in this thesis are reported for the first time together with explanations. In some cases the results consist of modifications and improvements over previously published work. However, there is still room for further advancement in all the studies undertaken.

In this section the most important conclusions from this thesis that can be found, especially in those chapter four to chapter six are given. It will be followed by some recommendations for future work.

7.2 Conclusions

Chapter one has reviewed some background on the development of optical fibre communication systems. The advantages of using all-optical processing in comparison with the electronic configuration have been described. The objectives of this doctoral research are clearly identified. Theoretical concepts and properties of the optical fibre communication are presented in chapter two. This is to help understand the basic theory

that is involved in communicating with optical fibres. Nonlinear effects such as SPM, XPM and FWM are explained in detail. In chapter three, the most important component in this work i.e. the semiconductor optical amplifier is characterised. The gain was measured to be 20 dB at an injected current of 200 mA which was chosen to be used in all the experimental work reported here apart from the transient studies in chapter six. The saturation output power was found to be 3.85 dBm.

CSRZ conversion and transmission has been demonstrated in chapter four. All-optical data format conversion from RZ and NRZ has been performed for a single channel system and a four channel WDM system. The converted format, CSRZ, is observed within the full optical bandwidth of the device which is 28.8 nm. However, the data must be separated by at least 1 nm in wavelength from the control pulse. There is no restriction of the control pulse wavelength except that the control pulse must be inside the SOA's bandwidth and should be suppressed to the lowest power, after the nonlinear conversion, in order to increase the BER of the converted channels. The CSRZ format was shown to be more tolerant to nonlinear effects in the transmission fibre. An optical signal with large nonlinearity tolerance allows for longer transmission distances and should greatly improve the stability of optical transmission performance. A 0.9 dB improvement on the receiver sensitivity is observed for CSRZ converted from NRZ, and 0.5 dB if converted from RZ. This is due to an enhancement in the total energy contained in the pulse sequence with a suppression of the carrier of the CSRZ. The SOA-NOLM has proven that it could be an attractive device for converting data formats in all-optical networks.

Chapter five presents an all-optical switch with a symmetric switching window by employing two identical control pulses into the SOA-NOLM. The width of the switching window is dependent on the SOA offset while the edges are controlled by the length of the

SOA. It is clear that the SOA is the core factor that determines the results in various SOA-NOLM applications. In chapter six, the current that biases the SOA was shown to control the level of transient power observed in the first few pulses of the circulating shift register. The transient also can be reduced by adjusting the input power of the control pulses. This chapter also studied the operation of an all-optical circulating shift register with an inverter.

7.3 Future Work

As the research addressed in this thesis is relevant to the future of all-optical processing, there is much work that may be continued. The successful implementation of the CSRZ conversion suggests that further development for realising other format conversions, such as duobinary, would be fruitful. This could contribute to a general all-optical format generator or converter that could be used in any network. The effect of changing the wavelength of the control pulse within the optical bandwidth and the performance as the number of channels is increased beyond four is worth studying in order to optimise the converter. It would also be interesting to study the use of the symmetrical switching window at higher channel bandwidths. Thus exploring the limitations due to the optical bandwidth of the SOA. The transient behaviour observed in the shift register can be theoretically modelled and analysed in more detail. This phenomenon can also be studied in other all-optical devices where significant time delays are involved in the system.

References

1. G. P. Agrawal, *Fiber-Optic Communication Systems*, 2nd eds., 1997, Wiley.
2. J.Gowar, *Optical Communication System,* 2nd eds., 1993. Prentice Hall.
3. G.Keiser, *Optical Fiber Communication,* 3rd eds., 2000, McGraw Hill.
4. R.Menzel, *Photonics:Linear and Nonlinear Interactions of Laser Light and Matter,* 2001, Springer.
5. Pallab Bhattacharya, *Semiconductor optoelectronic devices,* 2nd eds., 1997, Prentice Hall.
6. F.G.Smith and T.A.King, *Introduction to Optics and Photonics,* 2000, Wiley.
7. C.R.Pollock and M.Lipson, *Integrated Photonics,* 2003, Kluwer.
8. J. Bellamy, *Digital Telephony*, 1991, Wiley.
9. K.Iizuka, *Elements of Photonics,* 2002, Wiley.
10. G. P. Agrawal, *Nonlinear Fiber Optics*, 3rd eds., 2001, Academic Press.
11. Y.Guo, C.K.Kao, E.H.Li and K.S.Chiang, *Nonlinear Photonics*, 2002, Springer.
12. D. Marcuse, A. R. Chraplyvy, and R. W. Tkach, *Dependence of cross-phase modulation on channel number in fibre WDM systems*, J.Lightwave Technol., 1994, **12**(5): pp.885-887.
13. G.Bellotti, A.Bertaina, and S.Bigo, *Dependence of self-phase modulation impairments on residual dispersion in 10 Gb/s based terrestrial transmissions using standard fibre*, IEEE Photon. Technol. Lett., 1999, **11**(7): pp.824-826.
14. K.Inoue, *Four-wave mixing in an optical fibre in the zero-dispersion wavelength range*, Journal of Lightwave Technology, 1992, **10**(11): pp.1553-1561.
15. J.E.Sharping, M.Fiorentino, A.Coker, P.Kumar and R.S.Windeler, *Four-wave mixing in microstructure fibre,* Optics Letters, 2001, **26**(14):pp.1251-1254.

16. H.Taga, *Long distance transmission experiment using the WDM technology*, J.Lightwave Technol., 1996. **14**(6): pp.1287-1298.

17. R.W.Tkach, A.R.Chraplyvy, F.Forghieri, A.H.Gnauck, and R.M.Derosier, *Four-photon mixing and high speed WDM systems*, J.Lightwave Technol., 1995, **13**(5): pp.841-849.

18. R.W.Boyd, *Nonlinear optics*, 2nd eds., 2003, Academic Press.

19. D.Cotter and A.M.Hill, *Stimulated Raman crosstalk in optical transmission: Effects of group velocity dispersion*, Electron. Lett., 1984, **20**(4): pp.185-187.

20. P.P.Banerjee, *Nonlinear optics,* 2004, Marcel Dekker.

21. Y.Aoki,K.Tajima, and I.Mito, *Input power limits of single-mode optical fibres due to stimulated Brillouin scattering in optical communication systems*, J.Lightwave Technol., 1988, **6**(5): pp. 710-719.

22. Q. Jiang and M. Kavehrad, *A frequency calibration method for multilocation optical FDM networks,* IEEE Photonics Technology Letters, 1993, **5**(10): pp.1253-1256.

23. I. Akasaki, S. Sota, H. Sakai, T.Tanaka, M. Koike, and H. Amano, *Shortestwavelength semiconductor laser diode*, Electron. Lett., 1996, vol.**32**: pp. 1105-1106.

24. S.Nakamura, Y.Ueno and K.Tajima, *168 Gb/s all-optical wavelength conversion with a symmetric-Mach-Zender-type switch*, IEEE Photonics Technology Letters, 2001, vol.**13**: pp.1091-1093.

25. N.J. Doran and D. Wood, *Nonlinear optical loop mirror,* Opt. Lett., 1998, vol. **13**:pp. 56-58.

26. J.Sokolov, P.Prucnal, I.Glesk, and M.Kane, *A terahertz optical asymmetric demultiplexer (TOAD)*, IEEE Photonics Technol. Lett., 1993, vol.**5**:pp787-790.

27. I.Glesk, J.Sokolov, and P.Prucnal, *Demonstration of all-optical demultiplexing of TDM data at 250Gb/s*, Electron Lett., 1994, vol.**30**:pp.339-341.

28. D.Davies, A.Ellis, T.Widdowson and g.Sherlock, *10 Gb/s data switched semiconductor laser amplifier nonlinear loop mirror*, Electron Lett., 1995, vol.**31**:pp.111-112.

29. A.Ellis, d.Davies, A.Kelly, and W.Pender, *Data driven operation of semiconductor amplifier loop mirror at 40 Gb/s*, Electron Lett., 1995, vol.**31**:pp.1245-1246.

30. A.Ellis, D.Patrick, D.Flannery, R.Manning, D.Davies, and D.Spirit, *Ultra-high speed OTDM networks using semiconductor amplifier-based processing nodes*, J.Lightwave Technol, 1995, vol.**13**:pp.761-770.

31. K.Suzuki, K.Iwatsuki, S.nishi, and m Saruwatari, *Error-free demultiplexing of 160 Gb/s pulse signal using optical loop mirror including semiconductor laser amplifier*, Electron. Lett., 1994, vol.**30**:pp.1501-1503.

32. M.J.Connelly, *Semiconductor Optical Amplifiers*, 2002, Kluwer.

33. M.Eiselt, W.Piper, and G.Weber, *SLALOM: semiconductor laser amplifier in a loop mirror*, J.Lightwave Technol., 1995, vol.**13**:pp.2099-2112.

34. N.Grote, and H.Venghaus, *Fibre Optic Communication Devices*, 2001, Springer.

35. H.G.Shiraz, *Semiconductor Laser Diodes and Amplifiers*, 2004, Imperial College Press.

36. G.P.Agrawal, *Semiconductor Lasers*, 2001, Kluwer.

37. B.E.Saleh, and M.C.Teich, *Fundamentals of Photonics*, 1991, John Wiley.

38. H.J.S.Dorren, G.D.Khoe, and D.Lenstra, *All-optical switching of an ultrashort pulse using a semiconductor optical amplifier in a Sagnac-interferometric arrangement*, Opt.Comm., 2002, vol.**205**:pp.247-252.

39. J.Leuthold, C.H.Joyner, B.Mikkelsen, G.Raybon, J.L.Pleumeekers, B.I.Miller, K.Dreyer, and C.A.Burrus, *100Gb/s all-optical wavelength conversion with integrated SOA delayed-interference configuration*, Electron Lett., 2000, vol **36**:pp.1139-1130.

40. G.P.Agrawal, *Population pulsation and nondegenerate four-wave mixing in semiconductor laser amplifiers*, J.Opt.Soc.Am.B, 1998, vol.**5**:pp.147-159.

41. J.Moores, K.Bergman, H.Haus, and E. Ippen, *Demonstration of optical switching by means of solitary wave collisions in a fibre ring reflector*, Optics Letters, 1991, vol. **16**:pp.138-140.

42. M.Islam, *Ultrafast Fibre Switching Devices and Systems*, 1992, Cambridge University Press.

43. N.J.Smith, and N.J.Doran, *Picosecond soliton transmission using concatenated nonlinear optical loop-mirror intensity filters*, J.Opt.Soc.Am.B, 1995, vol.**12**:pp.1117-1125.

44. R.J.Manning, A.D.Ellis, A.J.Poustie, and K.J.Blow, *Semiconductor laser amplifiers for ultrafast all-optical signal processing*, J.Opt.Soc.Am.B, 1997, vol.**14**:pp.3204-3216.

45. T.K.Liang, H.K.Tsang, C.S.Wong, and C.Shu, *All-optical time-division demultiplexing with polarization-diversity nonlinear loop interferometer*, Optics Express, 2003, vol.**11**:pp.2047-2052.

46. S.Diez, R.Ludwig, and H.G.Weber, *Gain-Transparent SOA-Switch for High-Bitrate OTDM Add/Drop Multiplexing*, IEEE Photonics Technology Letters, 1999, vol.**11**:pp.60-62.

47. R.J.Manning, I.D.Philips. A.E.Kelly, A.J.Poustie and K.J.Blow, *All-optical clock division at 40 GHz using semiconductor optical amplifier based nonlinear interferometer*, Electronics letters, 1999, vol.**35**:pp.121-124.

48. R. S. Tucker and W. D. Zhong, *Photonic packet switching:An overview*, IEICE Trans. Electron., 1999, vol.**E82-C**:pp.202-212.

49. K.L. Hall, and K.A. Rauschenbach, *All-Optical bit pattern generation and matching*, Electron.Lett., 1996, vol.**32**:pp.1214-1215.

50. A.E. Kelly, I.D. Phillips, R.J. Manning, A.D. Ellis, D. Nesset, D.G. Moodie, and R.Kashyap, *80 Gbit/s All-Optical Regenerative Wavelength Conversion Using Semiconductor Optical Amplifier based Interferometer*, Electron. Lett., 1999, vol.**35**:pp. 1477-1478.

51. A.D. Ellis, A.E. Kelly, D. Nesset, D. Pitcher, D.G. Moodie, and R. Kashyap, *Error Free 100 Gb/s Wavelength Conversion Using Grating Modulation in a 2 mm Long Semiconductor Optical Amplifier*, Electron. Lett., 1998, vol.**34**:pp1958-1959.

52. J. Zhou, N. Park, J.W. Dawson, K.J. Vahala, M.A. Newkirk, and B.I. Miller, *Terahertz Four-Wave Mixing Spectroscopy for Study of Ultrafast Dynamics in a Semiconductor Optical Amplifier*, Appl. Phys. Lett., vol.**63**:pp.1179-1181.

53. K. Uchiyama, S. Kawanishi, and M. Saruwatari, *100-Gb/s Multiple-Channel Output All-Optical OTDM Demultiplexing Using Multichannel Four-Wave Mixing in a Semiconductor Optical Amplifier*, IEEE Photonic Technol. Lett., 2002, vol.**10**:pp.890-892.

54. K.L.Deng, I.Glesk, K.I.Kang, and P.R.Prucnal, *Unbalanced TOAD for optical data and clock separation in self-clocked transparent OTDM networks*, IEEE Photonics Technology Letters, 1997, vol.**9**:pp.830-832.

55. W.M.Wong's SLALOM model based on reference no. 33.

56. Y.Miyamoto, A. Hirano, K. Yonenaga, A. Sano, H. Toba, K. Murata, and O. Mitomi, *320 Gbit/s (8x40 Gbit/s) WDM transmission over 367 km with 120 km repeater spacing using carrier-suppressed return-to-zero forma,* Electronics Letters, 1999, vol.**35**:pp.2041–2042.

57. G. Bosco, A. Carena, V. Curri, R. Gaudino, and P. Poggiolini, *On the use of NRZ, RZ and CSRZ modulation formats for ultra-dense WDM at 40 Gb/s*, European Conference on Optical Communication (ECOC), 2002, vol.**3**:pp.3.7.

58. Y.Zhu, W. S. Lee, P. Lobb, C. Schahill, D. Witley, S. Savory, C. Fludger, B. Shaw, and A. Hadjifotiou, *Polarization-channel-inetrleaved carrier-suppressed RZ ETDM/DWDM transmission at 40 Gbit/s with 0.8 bit/s/Hz spectral efficiency,* European Conference on Optical Communication (ECOC), 2001, vol.**1**:pp.54–55.

59. A. Agrawal, S. Banerjee, D. F. Grosz, A. P. K¨ung, D. N. Maywar, A. Gurevich, and T. H. Wood, *Ultrahigh- capacity long-haul 40-Gb/s WDM transmission with 0.8-bit/s/Hz spctral efficiency by means of strong optical filtering*, IEEE Photonics Technology Letters, 2003, vol.**15**:pp.470–472.

60. D.S.Lee, M.S.Lee, Y.J.Wen, and A.Nirmalathas, *Electrically Band-Limited CSRZ Signal With Simple Generation and Large Dispersion Tolerance for 40-Gb/s WDM Transmission Systems,* IEEE Photonics Technology Letters, 2003, vol.**15**:pp.987-989.

61. G. Wenke and M. Klimmek, *Consideration on the alpha-Factor of Nonideal, external optical Mach-Zehnder Modulators,* Journal of Optical Communications, 1996, vol.**17**:pp.42–48.

62. Wendi Li, Minghua Chen, and Yi Dong, *All-Optical Format Conversion From NRZ to CSRZ and Between RZ and CSRZ Using SOA-Based Fiber Loop Mirror,* IEEE Photonics Technology Letters, 2003, vol.**16**:pp.203-205.

63. C.G.Liu, Y.J.Kim, C.S.Park, H.J.Lee, and C.S.Park, *Experimental demonstration of 10-Gb/s data format conversions between NRZ and RZ using SOA-loop-mirror,* Journal of Lightwave Technol., 2005, vol **23**:pp.834-841.

64. W.M.Wong, *CSRZ generation using SOA-NOLM: A VPI Model*, 2004, Aston University.

65. R..J.Manning, D.A.O.Davies, D.Cotter, and J.K.Lucek, *Enhanced recovery rates in semiconductor laser amplifiers using optical pumping*, Electron Lett., 1994, vol.**19**:pp.889-891.

66. O.Wada, *Femtosecond semiconductor-based optoelectronic devices for optical communications systems,* Optical and Quantum Electronics, 2000, vol.**32**:pp.453-471.

67. J.P.Sokoloff, I.Glesk, and P.R.Prucnal, *Performance of 50 Gb/s OTDM system using a TOAD*, IEEE Photonics Technology Letters, 1994, vol.**6**:pp.98-100.

68. B.C.Wang, V.Baby, W.Tong, L.Xu, M.Friedman, R.J.Runser, I.Glesk, and P.R.Prucnal, *A novel fast optical switch based on two cascaded TOADs*, Optics Express, 2002, vol.**10**:pp.15-23.

69. H.Shi, *Performance analysis on semiconductor laser amplifier loop mirrors*, Journal of Lightwave Technol., 2002, vol **20**:pp.682-688.

70. H.L.Minh, Z.Ghassemlooy, W.P.Ng, and R.Ngah, *Terahertz Optical Asymmetric Demultiplexer with a symmetrical switching window*, London Communication Symposium, 2004, pp.89-92.

71. P.Toliver, R.J.Runser, I.Glesk, and P.Prucnal, *Comparison of three nonlinear interferometric optical switch geometry*, Opt.Comm., 2000, vol.**175**:pp.365-373.

72. G.Toptchiyski, S.randel, K.Petermann, S.Diez, E.Hilliger, C.Schmidt, C.Schubert, R.Ludwig, and H.G.Weber, Journal of Lightwave Technol., 2000, vol **18**:pp.2188-2195.

73. K.I.Kang, T.G.Chang, I.Glesk, and P.R.Prucnal, *Comparison of Sagnac and Mach-Zender ultrafast all-optical inteferometric switches based on a semiconductor resonant optical nonlinearity*, Applied Optics, 1996, vol.**35**:pp.417-426.

74. N.A.Whitaker, M.C.Gabriel, H.Avramopolous, and A.Huang, *All-optical, all-fiber circulating shift register with an inverter*, Optics Letters, 1991, vol.**16**:pp.1999-2001.

75. A.J.Poustie, R.J.Manning and K.J.Blow, *All-optical circulating shift register using a semiconductor optical amplifier in a fibre loop mirror*, Electronics Letters, 1996, vol.**32**:pp.1215-1216.

76. K.L.Hall, J.P.Donelly, S.H.Groves, C.I.Fennely, R.J.Bailey and A.Napolene, *40 Gbit/s all-optical circulating shift register with an inverter*, Optics Letters, 1997, vol.**22**:pp.1479-1481.

77. H.J.Lee and H.G.Kim, *Polarisation-independent all-optical circulating shift register based on self-phase modulation of semiconductor optical amplifier*, Electronics Letters, 1999, vol.**35**:pp.70-72.

78. V.W.S.Chan, K.L.Hall, E.Modiano, and K.A.Rauschenbach, *Architectures and technologies for high-speed optical data networks*, Journal of Lightwave Technol., 1998, vol.**16**:pp.2146-2168.

79. D.S.Seo, D.Y.Kim, and H.F.Liu, *Timing jitter reduction of gain switched DFB laser by external injection seeding*, Electronics Letters, 1996, vol.**32**:pp.44-45.

80. R.J.Runser, D.Zhou, C.Coldwell, B.C.Wang, P.Toliver, K.L.Deng, I.Glesk, and P.Prucnal, *Interferometric ultrafast SOA-based optical switches: from devices to applications*, Opt.Quantum Electron., 1997, vol.**33**:pp.841-874.

81. K.Iga, *Fundamentals of laser optics*, 1994, Plenum Press NY.

82. K.J.Blow, R.J.Manning, and A.J.Poustie, *Nonlinear optical loop mirrors with feedback and a slow nonlinearity*, Optics Comm., 1997, vol.**134**:pp.43-48.

83. R.J.Manning, A.J.Poustie, K.J.Blow, *All-optical clock division using a semicondcuctor optical amplifier loop mirror with feedback*, Electronics Letters, 1996, vol.**32**:pp.978-981.

Publications

1. M.M.Nahas, M.H.A.Wahid, R.A.Ibbotson, and K.J.Blow, *10 Gb/s transmission over long distance after all-optical NRZ and RZ to CSRZ format conversion using SLALOM*, Nonlinear Guided Waves Conference 2005, Proc.ppWB7, Dresden, Germany, September 2005.
2. M.H.A.Wahid, M.M.Nahas, R.A.Ibbotson, and K.J.Blow, *WDM transmission after All-optical NRZ to CSRZ and RZ to CSRZ format conversion using an SOA-NOLM*, submitted to Optics Communications.